Department of Nuclear Physics and Biophysics
Faculty of Mathematics, Physics and Informatics
Comenius University in Bratislava

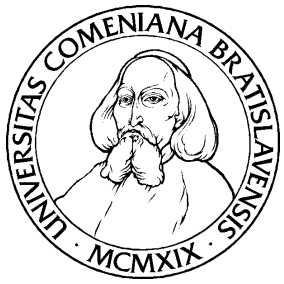

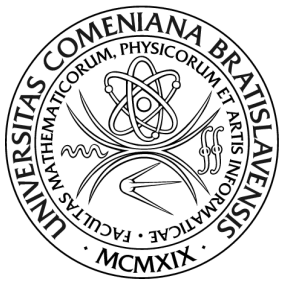

Study of spontaneous fission and K isomerism in rutherfordium isotopes

by

Pavol Mošať

Disseration thesis

Bratislava, 2019

Univerzita Komenského v Bratislave
Fakulta matematiky, fyziky a informatiky

83452776

ZADANIE ZÁVEREČNEJ PRÁCE

Meno a priezvisko študenta: Mgr. Pavol Mošať
Študijný program: jadrová a subjadrová fyzika (Jednoodborové štúdium, doktorandské III. st., denná forma)
Študijný odbor: jadrová a subjadrová fyzika
Typ záverečnej práce: dizertačná
Jazyk záverečnej práce: slovenský
Sekundárny jazyk: anglický

Názov: Štúdium spontánneho štiepenia a K izomery v izotopoch rutherfordia
Study of spontaneous fission and K isomerism in rutherfordium isotopes

Anotácia: Získanie informácií o najťažších známych prvkoch je veľkou výzvou pre teoretickú, ako aj experimentálnu jadrovú fyziku. Teoretické modely často nedokážu uspokojivo opísať štruktúru atómových jadier s extrémnym počtom nukleónov. Aj to je motiváciou pre realizáciu a budovanie nových experimentov zameraných na oblasť najťažších známych atómových jadier.
Silným nástrojom na získanie nových informácií o superťažkých prvkoch je rozpadová spektroskopia jadier z oblasti prvkov s protónovým číslom vyšším ako 100. Vývoj novej detekčnej techniky umožnil detailné alfa a gama spektroskopické merania pre tieto izotopy a tým aj získanie nových informácií o ich štruktúre. Dôležitou o je taktiež informácia o účinných prierezoch reakcií a možnostiach produkcie týchto ťažkých jadier.

Cieľ: PhD projekt je zameraný na spracovanie, analýzu a fyzikálnu interpretáciu experimentálnych dát z meraní zameraných na produkciu najťžších známych prvkov. Merania budú realizované na separátore SHIP v GSI Darmstadt (Nemecko) príp. experimente SHELS v JINR Dubna (Rusko). Oba experimenty patria medzi popredné svetové pracoviská v tejto oblasti jadrovej fyziky. Aktuálne sú k dispozícii experimentálne dáta pre izotopy ruetherfordia, dubnia a seaborgia (Z=104 – 106).
Študent preberie zodpovednosť za experimentálne dáta z meraní zameraných na produkciu izotopov ruherfordia. Fyzikálnym cieľom práce bude štúdium vlastností ich spontánneho štiepenia a možnosti existencie izomérnych stavov očakávaných v týchto izotopoch s využitím metód rozpadovej spektroskopie. Po technickej stránke je očakáva spracovanie dát, ich analýza, fyzikálna interpretácia a opublikovanie výsledkov z merania.

Literatúra: Literatúra:
P.E. Hodgeson, E. Gadioli and E. Gadioli Erba, Introductory Nuclear Physics, Oxford University Press, 1997.
K. Heyde, Basic Ideas and Concepts in Nuclear Physics, Institute of Physics Publishing, 3rd edition 2004.
R. Casten, Nuclear Structure from a Simple Perspective, Oxford University Press, 1990.
Cyriel Wagemans, The Nuclear Fission Process, CRC Press, 1991
K.S. Krane, Introductory Nuclear Physics, John Wiley & Sons, 1988.
Cyriel Wagemans, The Nuclear Fission Process, CRC Press, INC (2000)

Univerzita Komenského v Bratislave
Fakulta matematiky, fyziky a informatiky

Články publikované v karentovaných časopisoch.

Poznámka: Doktorand preberie zodpovednosť za niektorú z tém v rámci riešených projektov. Počas štúdia by mal absolvovať sériu pobytov na zahraničných pracoviskách, preto je žiadúca flexibilita, znalosť angličtiny a schopnosť samostatne pracovať. Téma je zabezpečená grantovými prostriedkami a dlhodobou úspešnou medzinárodnou spoluprácou.

Kľúčové slová: jadrová štruktúra, rozpadová spektroskopia, gama spektroskopia, oneskorené štiepenie po beta premene, jadrové reakcie

Školiteľ: doc. Mgr. Stanislav Antalic, PhD.
Katedra: FMFI.KJFB - Katedra jadrovej fyziky a biofyziky
Vedúci katedry: prof. RNDr. Stanislav Tokár, DrSc.

Dátum zadania: 20.02.2015

Dátum schválenia: 23.02.2015 prof. RNDr. Jozef Masarik, DrSc.
garant študijného programu

.....
študent

.....
školiteľ

Student:

Mgr. Pavol Mošať
Department of Nuclear Physics and Biophysics
Faculty of Mathematics, Physics and Informatics
Comenius University in Bratislava
Mlynská dolina
842 48 Bratislava
Slovak Republic

Field of study: Nuclear and sub-nuclear physics
Study program: 4.1.5. Nuclear and sub-nuclear physics

Supervisor:

Dr. Stanislav Antalic
Department of Nuclear Physics and Biophysics
Faculty of Mathematics, Physics and Informatics
Comenius University in Bratislava
Mlynská dolina
842 48 Bratislava
Slovak Republic

Abstract

The dissertation thesis is focused on the topic of spontaneous fission properties of isotopes from the region around rutherfordium ($Z = 104$). Spontaneous fission is a decay mode important especially for trans-fermium isotopes where it can become the limiting factor for survival of such heavy nuclei. Measurements aimed at the production of rutherfordium and dubnium ($Z = 105$) isotopes with high statistics were carried out in GSI Darmstadt using velocity filter SHIP. In this work the SF decay properties (mainly focused on fission-fragment total kinetic energies) of isotopes ^{255}Rf, ^{256}Rf and ^{258}Rf produced in reactions $^{50}\mathrm{Ti} + {}^{207}\mathrm{Pb}$, $^{50}\mathrm{Ti} + {}^{208}\mathrm{Pb}$ and $^{50}\mathrm{Ti} + {}^{209}\mathrm{Bi}$ are presented. The method of time and position correlation search was used to identify spontaneous fission events. For the evaluation of the fission-fragment total kinetic energies (TKE), it was necessary to determine the correction to the energy deficit mainly due to the pulse-height defect, which is typical for the used silicon detectors. This effect was studied on spontaneous fission of ^{252}No, and the corretion was applied to evaluate the $\overline{TKE}$ of investigated rutherfordium isotopes. Tentative signature of bimodal fission was observed in TKE distributions of ^{255}Rf and ^{256}Rf. High statistics of produced ^{255}Rf opened an opportunity for the investigation of isomerism in this isotope. Two new high-K isomeric states in ^{255}Rf were identified by ER-CE-(CE)-α/SF correlation search with half-lives of $38 \pm 4\,\mu$s and $15 \pm 5\,\mu$s at excitation energies 1150–1450 keV and 900–1200 keV, respectively, and a tentative decay scheme was proposed.

Keywords:

fusion-evaporation reactions, spontaneous fission, total kinetic energy, pulse-height defect, nuclear isomerism

Abstrakt

Dizertačná práca je zameraná na tému vlastností spontánneho štiepenia izotopov rutherfordia ($Z = 104$). Spontánne štiepenie je proces jadrovej premeny, významný najmä pre izotopy z oblasti transfermií, kde sa stáva ohraničujúcim faktorom pre prežitie tak ťažkých jadier. Merania s produkciou izotopov rutherforia a dubnia ($Z = 105$) s výzmanou štatistikou dát boli uskutočnené v GSI Darmstadt s použitím rýchlostného filtra SHIP. V tejto práci sú predstavené výsledky meraní vlastností spontánneho štiepenia izotopov ^{255}Rf, ^{256}Rf and ^{258}Rf, ktoré boli syntetizované vo fúzno-výparných reakciách $^{50}\mathrm{Ti} + {}^{207}\mathrm{Pb}$, $^{50}\mathrm{Ti} + {}^{208}\mathrm{Pb}$ and $^{50}\mathrm{Ti} + {}^{209}\mathrm{Bi}$. Na identifikáciu spontánneho štiepenia bola použitá metóda hľadania časových a pozičných korelácií signálovz detektorov. Pre správne vyhodnotenie celkových kinetických energií (TKE) štiepnych fragmentov je nevyhnutné určeniť korekciu na energetický deficit spôsobený tzv. pulse-height defect-om, ktorý je typický pre použité kremíkové detektory. Tento efekt bol študovaný na spontánnom štiepení ^{252}No, na základe ktorého sme vyhodnotili $\overline{TKE}$ pre izotopy rutherfordia. V distribúciách TKE pre izotopy ^{255}Rf a ^{256}Rf bolo pozorovaných niekoľko indikácií bimodálneho štiepenia. Vďaka vysokej štatistike zozbieraných dát pre izotop ^{255}Rf sa naskytla možnosť pre štúdium izomérie. Na základe nájdených ER-CE-(CE)-α/SF korelácií boli v ^{255}Rf identifikované dva nové K-izoméry s polčasmi $38 \pm 4\,\mu$s a $15 \pm 5\,\mu$s a excitačnými energiami 1150–1450 keV and 900–1200 keV a tiež bola navrhnutá predbežná rozpadová schéma.

Keywords:

fúzno-výparné reakcie, spontánne štiepenie, celková kinetická energia, pulse-height defect, jadrová izoméria

Acknowledgements

I would like to express my gratitude to my supervisor Dr. Stanislav Antalic for his continuous support of my PhD study and related research, for his patience, help, and immense knowledge.

My sincere thanks also goes to Dr. Fritz P. Heßberger for the fruitful email discussions of results from the topic of spontaneous fission and isomerism in the transfermium region.

I thank Dr. Boris Andel, who provided me technical support for the data analysis at the beginning of my PhD study .

Finally, I would like to thank my family, my parents and my brother, and also my friends, for supporting me during the (sometimes tough and busy :)) period of the PhD study.

Contents

Preface

I started my PhD study at the Comenius University in Bratislava in September 2015 under the supervision of Dr. Stanislav Antalic. After a discussion I chose the spontaneous fission properties of rutherfordium isotopes as the topic of my work. This study was based on the analysis of the data collected at SHIP experiment (GSI Darmstadt) in 2014, in which I did not personally participated. However, at the very beginning of my study I went to GSI for three weeks, during which an experiment was performed at SHIP, where I got more familiar with the setup. During my PhD study I later also participated in many other experiments on several setups.

Experiments at SHELS at JINR (Dubna, Russia) were focused on the spectroscopy of rutherfordium and dubnium isotopes and also measurements of prompt neutron multiplicities from spontaneous fission of rutherfordium isotopes. At ISOLDE at CERN (Geneve, Switzerland/France) and AGFA in ANL (Chicago, USA), we performed several spectroscopic measurements for isotopes from the lead region. Experiment MARA at the University of Jyväskylä (Jyväskylä, Finland) was dedicated to the study of proton emitters. Besides I did the analysis of rutherfordium data and presented partial results at many international conferences and workshops dedicated to nuclear physics by an oral presentation or as a poster.

My study of rutherfordium isotopes was firstly focused on the topic of the total kinetic energies of fragments from the spontaneous fission of ^{255}Rf, ^{256}Rf and ^{258}Rf. From this analysis I prepared a publication in Acta Physica Polonica B focused on the energy correction of pulse-height defect for fission-fragment measurements with silicon detectors. Such a correction is crucial for the evaluation of total kinetic energies of fission fragments at SHIP and similar experiments. It allowed me to determine the total kinetic energies for rutherfordium isotopes. Later I also started to focus on the second topic, the search for K isomers in ^{255}Rf, which were observed for the first time in this isotope. This study was based on the internal-conversion electron spec-

troscopy. Finally, I summarized the results from both topics in the article, which I submitted to Physical Review C. This dissertation thesis is based on the same results, however the topics of total kinetic energies and K isomerism are discussed more in details here than in the articles.

The thesis is divided in six Chapters and an appendix. In Chapter 1 and introduction to the problematics is summarized. The work then continues with Chapter 2 where the physical background, related to discussed physics is explained. The experimental setup at SHIP, including the velocity filter, detectors, electronics and data analysis are described in Chapter 3. The Chapter 4 contains details about the irradiations with production of studied rutherfordium isotopes, as well as other isotopes used for the detector calibrations, and also information on how the isotopes were identified or separated from each other. Discussion of obtained results, comparison with previous results or theoretical calculations is in Chapter 5. The last Chapter is dedicated to conclusion and perspectives. The appendix contains information about the very interesting additional result I obtained during the analysis - the evaluation of α-decay branching ratio of ^{256}Rf from the two newly observed α-decay events and partial half-life for spontaneous fission of ^{251}No from one new event which doubled the overall statistics obtained up to now for this isotope.

Chapter 1

Introduction

The spontaneous-fission process is believed to finally terminate nuclear stability at increasing proton numbers Z or extreme ratios Z/N in heaviest nuclei. In the region of the heaviest elements, the macroscopic part of fission barrier vanishes at $Z \gtrsim 104$ and the nuclear stability against spontaneous fission (SF) is provided only by microscopic effects of few MeV resulting from the nuclear shell structure [1]. Investigation of structure and decay properties of the heaviest nuclei is essential in order to determine the production possibilities of superheavy isotopes, to understand the limits of nuclear stability and to improve models predicting next spherical proton and neutron shells beyond ^{208}Pb ($Z = 82, N = 126$). The study of spontaneous-fission properties such as fission-fragment mass distributions, total kinetic energies, prompt neutron emission and partial half-lives of the isotopes from the transfermium region presents a challenge for nuclear physics nowadays [2].

In this region only some basic experimental information on half-lives or branching ratios is available. The knowledge about fission modes, kinetic energy release and mass distribution of fission fragments is scarce. Especially interesting are total kinetic energy (TKE) measurements, that are connected to the fission mode (asymmetric from elongated shape, symmetric from elongated or compact shape). The experimental values of mean TKE ($\overline{TKE}$) and also TKE distributions are very valuable inputs for further theoretical descriptions of SF and calculations of SF properties.

Measurements of TKE distributions revealed the possibility of bimodal fission, with two fission modes, for several isotopes in trans-uranium region. Theoretical calculations discuss the possibility of bimodal fission for even $^{254\text{-}260}$Rf isotopes, which should be noticeable in their TKE distributions [3]. Experimental studies of mass and TKE distributions confirmed the concept

of bimodal fission in lighter nuclei up to nobelium (e.g. ^{258}Fm, ^{259,260}Md or ^{258,260}No) [4, 5]. Until now, only few results with limited statistics of SF events with measured total kinetic energy were obtained for rutherfordium ($Z = 104$) isotopes [4, 5, 6].

In this work we present data on SF of ^{255}Rf, ^{256}Rf, and ^{258}Rf obtained at SHIP, where fragment energies from the SF of nuclei implanted in a silicon detector were measured. For the evaluation of mean TKE release during the fission process it was necessary to correct the detector response for the energy deficit, mainly due to the pulse height defect.

Another interesting feature studied in this region is the presence of isomeric states. Detailed spectroscopic studies of nuclei near the deformed shells $Z = 100$ and $N = 152$ where the presence of K isomers was found, serve us as a strong tool for investigations into the structure of the heaviest elements.

The existence of K-isomeric states was previously confirmed in several even-even isotopes (e.g. ^{252}No [7], ^{254}No [8, 9, 10], ^{254}Rf [11], ^{256}Rf [12, 13]), and odd-even or even-odd isotopes (e.g. ^{253}No [14, 15], ^{255}Lr [16, 17], ^{257}Rf [18]).

In ^{255}Rf, a single-particle $5/2^+[622]$ isomer with $T_{1/2} = 50 \pm 15\,\mu s$ populated by α decay of ^{259}Sg was previously identified with an excitation energy of $\approx 135\,keV$ [6]. However, the presence of K isomer in this isotope was not confirmed up to now. One of the motivations of our work was therefore to search for K isomers in ^{255}Rf.

Goals of thesis

The main goal of this work was to investigate the SF properties of isotopes ^{255}Rf, ^{256}Rf, and ^{258}Rf produced at fusion-evaporation reactions ^{50}Ti + ^{207}Pb, ^{50}Ti + ^{208}Pb and ^{50}Ti + ^{209}Bi. Such experiments can be performed in only few laboratories in the world. Our team at the Department of Nuclear Physics and Biophysics of Comenius University in Bratislava collaborate closely with experiment SHIP at GSI Darmstadt and SHELS at JINR Dubna. Part of the measurements was carried out in 2014 at GSI using the accelerator UNILAC and the velocity filter SHIP. The aim of these experiments is to obtain new data on the nuclear structure and on the production mechanism. Up to now there is a lack of satisfying data on SF properties of Rf isotopes. We focused our interests on the evaluation of $\overline{TKE}$ and energy distribution in respect to expected bi-modal fission. The other goal was to investigate the isotope of ^{255}Rf for the presence of K isomers, which were

confirmed in its neighbouring isotopes. For this purposes the same data were used.

Chapter 2

Physical background

2.1 Spontaneous fission

In 1938, two chemists, Otto Hahn and Fritz Strassman [19], showed that in irradiation of uranium nuclei with neutrons, elements such as barium or lanthanum were produced. In that time it was expected that this procedure could lead into production of heavier elements than uranium by neutron capture and consequent beta decay. They deduced that the uranium nuclei must have been somehow split, but as chemists they were restrained of making any physical conclusions. In 1939, Lise Meintner and Otto Robert Frinch [20] proposed a theoretical model in which a usually stable uranium nucleus after catching a neutron becomes very unstable and is subsequently divided into two lighter nuclei. This phenomenon and the two products were called *"fission"* of nucleus and *"fission fragments"*. A neutron capture is needed to induce the whole process, hence the name *"induced fission"*. In 1940, Georgy Nikolayevich Flerov and Konstantin Antonovich Petrzhak [21] were observing radioactive α decay of ^{238}U and discovered a possibility for the nucleus to undergo fission without previously catching a neutron. This process was observed on the background of α decays with about 7 orders smaller probability. Since this phenomenon appeared spontaneously, it was called *"spontaneous fission"*.

2.1.1 Fragments separation

The possibility for the nucleus to fission can be understood from the energy balance of the states before and after fission process. In the region

of such a heavy nuclei as ^{238}U the binding energy per nucleon is about 7.6 MeV. Considering the hypothetical fission of this nucleus into two lighter nuclei of the same mass 119 (a.k.a. symmetrical fission), the binding energy per nucleon for both created fragments increases to about 8.5 MeV. The binding energy difference between the prefission and postfission states is $-7.6 - (-8.5) = 0.9\,\mathrm{MeV}\,/\,\mathrm{nucleon}$. The total binding energy difference for the symmetrical fission of nucleus with mass $A = 238$ is about $0.9 \times 238 = 214\,\mathrm{MeV}$. This corresponds to an excess energy which can be released in different ways; such as the emission of neutrons, β particles, γ rays and so on. However, 80 % of this energy is transferred into the kinetic energies of fission fragments by the Coulomb repulsion. Although the spontaneous fission process (SF) may seem to be obviously energetically favorable, it is not able to compete with the α decay of ^{238}U. In fact, SF is quite rare decay mode in the region of $A < 250$. The explication of this hindrance lies in the mechanism of mass splitting. The process of fission can be described by a simplified model of separation of two spherical fragments of radii R_1 and R_2 ($R1 = R2$), masses $A_1 = A_2 = 119$ and $Z_1 = Z_2 = 46$, touching by their surfaces, so the separation distance R is

$$R = R_1 + R_2 = 2 \times 1.25 {A_1}^{1/3} = 12.2\,\mathrm{fm} \tag{2.1}$$

and the corresponding Coulomb potential

$$V = \frac{1}{4\pi\epsilon_0}\frac{Z_1 Z_2 e^2}{R} = 250\,\mathrm{MeV} \tag{2.2}$$

The liquid drop model can be used here. Consider a spherical liquid drop to start quadrupole oscillation around the initially spherical state. Nucleus as a liquid drop is being deformed from spherical shape into the shape of a "prolate" ellipsoid characterized by axes a and b, where $a < b$. Consequently the system is passing through a spherical shape again and due to the inertial motion it is being re-deformed into an oblate ellipsoidal shape, this time with axes $b < a$, then back to the spherical shape and so on. It is the surface tension force (analogy to the nuclear force) that is forcing a liquid drop to return into a spherical shape and preventing it from splitting when being stretched while inertia force is making the drop being re-deformed again. There are also repulsing forces between protons in a nucleus. When oscillations are strong enough the nucleus can be stretched so much, that the repulsing forces start to dominate over the surface tension forces and they are not anymore able to stop the ongoing deformation. The nucleus is

being fatally stretched until it is separated into two pieces. This qualitative approach can be described by semi-empirical Weiszäcker formula for nuclear binding energy, especially by the first three terms resulting from liquid drop model.

$$E_{bind} = a_{vol}A - a_{sur}A^{2/3} - a_{Coul}\frac{Z^2}{A^{1/3}} - a_{sym}\frac{(A-2Z)^2}{A} - \delta \tag{2.3}$$

The equation 2.3 was originally designed for a spherical nucleus of radius R. The nucleus can be extended into the shape of an ellipsoid of the same volume, what results in changes of surface and Coulomb (2^{nd} and 3^{rd}) terms from Eq. 2.3. The volume of the ellipsoid can be expressed as $\frac{4}{3}\pi ab^2$. The major and minor axis of the ellipse are given as

$$a = R(1+\varepsilon) \tag{2.4}$$

$$b = R(1+\varepsilon)^{-1/2} \tag{2.5}$$

where ε stands for the eccentricity of the ellipse and is related to the usually used quadrupole deformation parameter β as

$$\varepsilon = \beta\sqrt{5/4\pi} \tag{2.6}$$

By a simple substitution it could be verified that using Eqs. 2.4 and 2.5, the volume of the ellipse $\frac{4}{3}\pi ab^2$ becomes $\frac{4}{3}\pi R^3$. It means that the initial volume of the spherical nucleus is not changing by the ellipsoidal deformation. However the surface of a sphere will be changed as $\frac{4}{3}\pi aR^2((1+\frac{2}{5}\varepsilon^2+...))$ and the third Coulomb term of equation 2.3 will be changed by a factor $(1-\frac{1}{5}\varepsilon^2+...)$. The binding energy difference between the nucleus of spherical shape and deformed into an ellipsoid will be

$$\Delta E = E_{bind}(\varepsilon) - E_{bind}(\varepsilon = 0) \tag{2.7}$$

$$\begin{aligned}\Delta E = &- a_{sur}A^{2/3}(1+\frac{2}{5}\varepsilon^2+...) - a_{Coul}\frac{Z^2}{A^{1/3}}(1-\frac{1}{5}\varepsilon^2+...) \\ &+ a_{sur}A^{2/3} + a_{Coul}\frac{Z^2}{A^{1/3}}\end{aligned} \tag{2.8}$$

which can be approximately rewritten as

$$\Delta E \cong (-\frac{2}{5}a_{sur}A^{2/3} + \frac{1}{5}a_{Coul}\frac{Z^2}{A^{1/3}})\varepsilon^2 \tag{2.9}$$

When the second term of the Eg. 2.9 becomes larger than the first one, a nucleus becomes unstable against the deformation. The attractive forces are not able to stop the extension and the nucleus splits. Therefore the condition for SF can be expressed as

$$\frac{1}{5}a_{Coul}\frac{Z^2}{A^{1/3}} > \frac{2}{5}a_{sur}A^{2/3} \tag{2.10}$$

and after some changes the condition 2.10 becomes

$$\frac{Z^2}{A} > \frac{2a_{sur}}{a_{Coul}} \tag{2.11}$$

where the term $2a_{sur}/a_{Coul}$ is also known as "critical" value, it slightly varies for different nuclei and can be expressed as

$$\Big(\frac{Z^2}{A}\Big)_{crit} = \frac{2a_{sur}}{a_{Coul}} = 50.883\Big[1 - 1.7826\Big(\frac{N-Z^2}{A}\Big)\Big] \tag{2.12}$$

A parameter x called fissility parameter is defined as a ratio of Z^2/A and its critical value as

$$x = \Big(\frac{Z^2}{A}\Big)/\Big(\frac{Z^2}{A}\Big)_{crit} \tag{2.13}$$

The parameter x can be used as an indicator of SF possibility. Since the whole deduction is based on the liquid drop model without adding any microscopic corrections, the indication is rough.

2.1.2 Partial half-lives

A dependence of SF partial half-lives on parameter Z^2/A can be clearly seen from the systematic of experimental data in Fig. 2.1. In this plot only values for even-even isotopes were used since they are not so strongly affected by effect of unpaired nucleons as even-odd or odd-odd isotopes [23]. The partial-half-life curves of isotopic groups for each element from Cm to No show peaks. This enhanced stability against SF is caused by the presence of closed deformed shell at $N = 152$. Better view on this effect can be seen in Fig. 2.2 where SF partial half-lives are plotted against neutron number

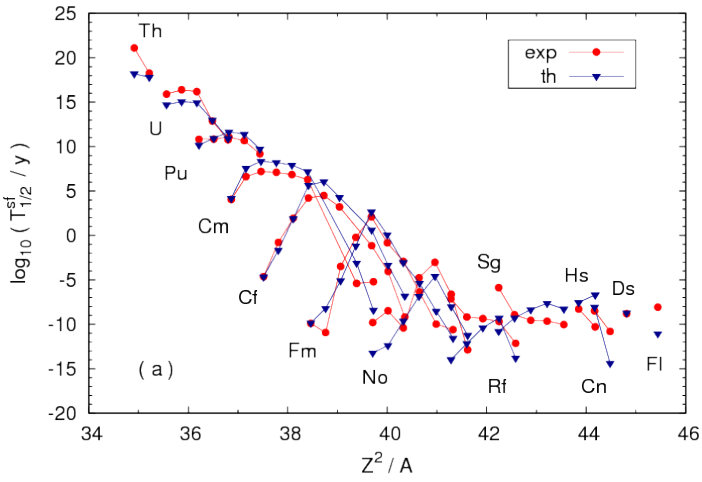

Figure 2.1: Spontaneous fission partial half-lives of even-even isotopes as a function of Z^2/A [22].

N. The stabilizing effect of shell with $N = 152$ seems to be influencing only isotopes up to No ($Z = 102$). For isotopes of heavier elements the effect disappeared, but a new trend of increasing SF partial half-lives is observed. This increase can be an indication of another possible closed shells (deformed at $N = 162$ or spherical at $N = 184$).

2.1.3 Fission barrier and microscopic effects

In previous section was mentioned that the process of nuclear fission strongly depends on the shape and height of fission barrier. Based on the liquid drop model assumptions a very simple estimations for fission barrier height were made ($\sim 250\,MeV$) and the fissility parameter was defined. Although the liquid drop model calculations can provide us useful hints for SF behavior, a relatively small corrections to fission barriers of only couple MeV, resulting from microscopic effects, may have strong influence and significantly change the SF characteristics. Especially in the region of super-heavy elements it is expected that fission barrier heights resulting from liquid drop model will decrease to only few MeV at $A = 250$ [25]. With increasing mass number the barriers would become extremely low and nuclei would become extremely unstable against SF as can be seen on the solid line in Fig. 2.3.

In order to investigate SF further it is necessary to include microscopic

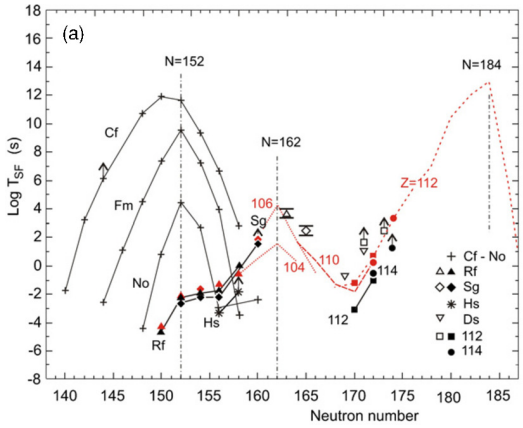

Figure 2.2: Spontaneous fission partial half-lives (experimental) of even-even isotopes as a function of on neutron number N. Solid symbols and crosses are even-even isotopes, open symbols are even-odd. Black color represents experimental data, red color calculated data. A strong effect of closed deformed shell $N = 152$ is evident for isotopes from up to No. From Rf the stabilizing effect seems to disappear[24].

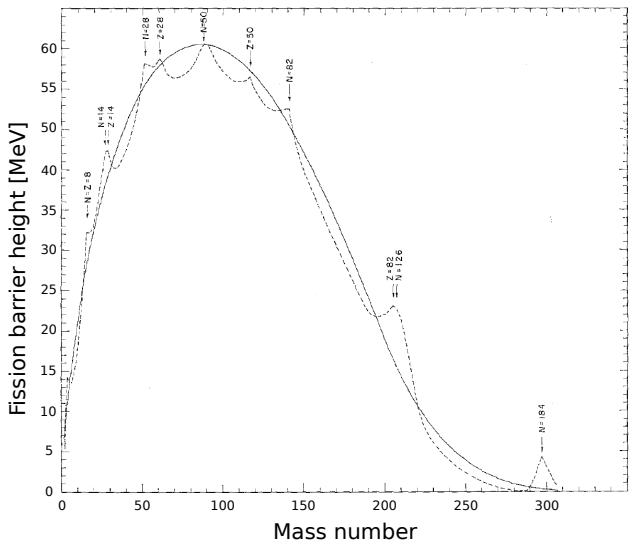

Figure 2.3: Fission barrier height (fission activation energy) variation with mass number calculated for the most stable isotopes. The full line represents calculations based only on liquid drop model, dashed line includes microscopic effects [25].

effects, which can change the fission barriers. These effects are composed of two main components, shell correction δS and pairing correction δP. The shell-corrected liquid-drop-barrier heights are indicated by a dashed line in Fig. 2.3 and it can be seen that in the region of extremely heavy nuclei around $A = 300$ where the liquid-drop barriers practically completely vanish, the microscopic effect start to play crucial role for SF.

The total energy of nucleus can written as a sum of liquid-drop-model component E_{LDM} and microscopic shell and pairing components as

$$E = E_{LDM} + \sum_{p,n} (\delta S + \delta P) \tag{2.14}$$

The examples of fission barriers resulting from the liquid drop model are shown on the top of Fig. 2.4. The shell component of microscopic correction (indicated in the middle) is also a function of deformation. By adding this component, double humped fission barriers are obtained (bottom).

Several theoretical models can be used to calculate the fission-barrier heights. Some evaluations can be made using Thomas-Fermi model processed in [26], where no microscopic corrections are included. They can be subsequently added from FRDM (finite range droplet model) [27]. Another possibility is to use the FRLDM (finite range liquid drop model) from [28] which is complex enough and includes directly macroscopic and microscopic effects.

2.1.4 Mass distribution

Fragment-mass distributions are nice example for an important role of shell effects in SF process. According to the liquid drop model, the largest energy release in fission would be achieved for nuclear split into two equally large fragments making the symmetrical mode the most favorable. However until 1970, thirty years after the discovery of fission, all acquired data for both spontaneous and induced fission showed preferably asymmetric mass distribution of fragments. While for the fission of ^{236}U was measured that the most preferable masses of lighter and heavier fragments were $A_L = 95$ and $A_H = 140$, for twenty-nucleon heavier ^{256}Fm it was $A_H = 114$ and $A_H = 141$. The same studies of more isotopes are summarized in Fig. 2.5. The masses of heavier fragments are approximately constant while the variation of lighter-fragment masses is evident [24].

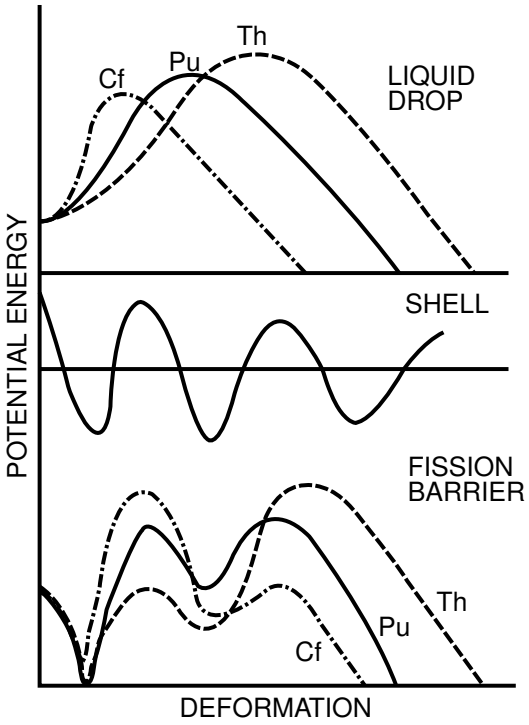

Figure 2.4: Liquid-drop-model fission barrier (top) corrected by the shell component of microscopic effects (middle). The final double humped fission barrier at the bottom [29].

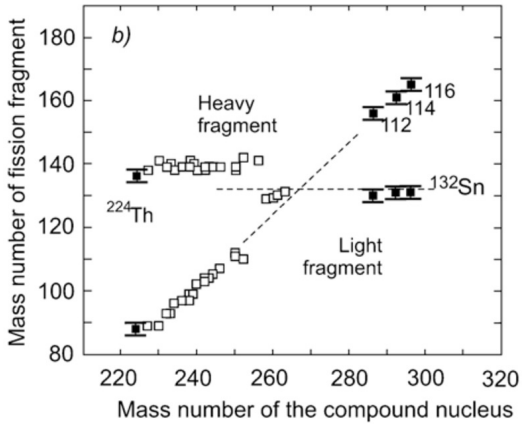

Figure 2.5: Most probable masses of fission fragments [24].

The mass-distribution asymmetry is caused by shell effects, especially the effect of closed spherical shell for doubly magic nucleus ^{132}Sn with $Z = 50$ and $N = 82$. One of the fragments is preferably formed with the similar configuration as ^{132}Sn during the fission process. However, in Fig. 2.5 the most probable mass of heavier fragment for fissioning nuclei up to $A \sim 260$ is around $A = 139$ and not $A = 132$ as would be expected from the previous argument. The explanation is based on the fact that during the process of stretching the fragments are formed with the same ratio of neutrons and protons as the ratio N/Z of fissioning nucleus. So the final most probable mass $A = 139$ for the heavier fragment is the result of compromise between being as close to the doubly magic configuration as possible and maintaining the ratio N/Z of fissioning nucleus.

The fission-barrier height does not depend only on nuclear deformation as was shown in Fig. 2.4 but is also a function of mass asymmetry of fragments formation during the stretching process. A very nice example of how complex the variety of effects influencing the mass distribution is, was observed in SF of ^{180}Hg [30]. A symmetrical fission of this isotopes would lead to the two fragments of ^{90}Zr which has magic configuration with $N = 50$. Before the experiment, symmetrical fission mode of this isotope was the most anticipated among physicists, however the experiment showed that the most probable ratio of fragment masses after the fission were 72/108. To explain this results a complex calculations of potential energy dependence on deformation and mass distribution were performed. The results for PES (potential energy surface) calculations are shown in Fig. 2.6 [30]. Although the energetic minimum is located in the position of symmetrical fission, this mass distribution mode is hindered due to the large barrier present in the elongation process. A way "around" the barrier leads to the asymmetrical mass distribution.

In the region of very heavy nuclei, mass distributions of several isotopes were determined up to rutherfordium. The systematics of these distributions is shown on Fig. 2.7. A rather sharp transition from asymmetric to symmetric fission for the isotopes can be observed in fermium and nobelium. The hints of the same behaviour are also for rutherfordium, although in this case the distributions are based on limited statistics.

2.1.5 Total kinetic energy release

The electrostatic interaction between two fission fragments of positive charges given by proton numbers Z_1 and Z_2 can be described as

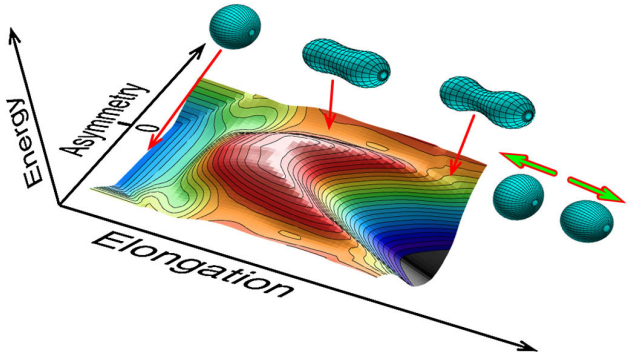

Figure 2.6: Potential energy surface for ^{180}Hg dependence on nuclear deformation and asymmetry of mass distribution of forming fragments [30].

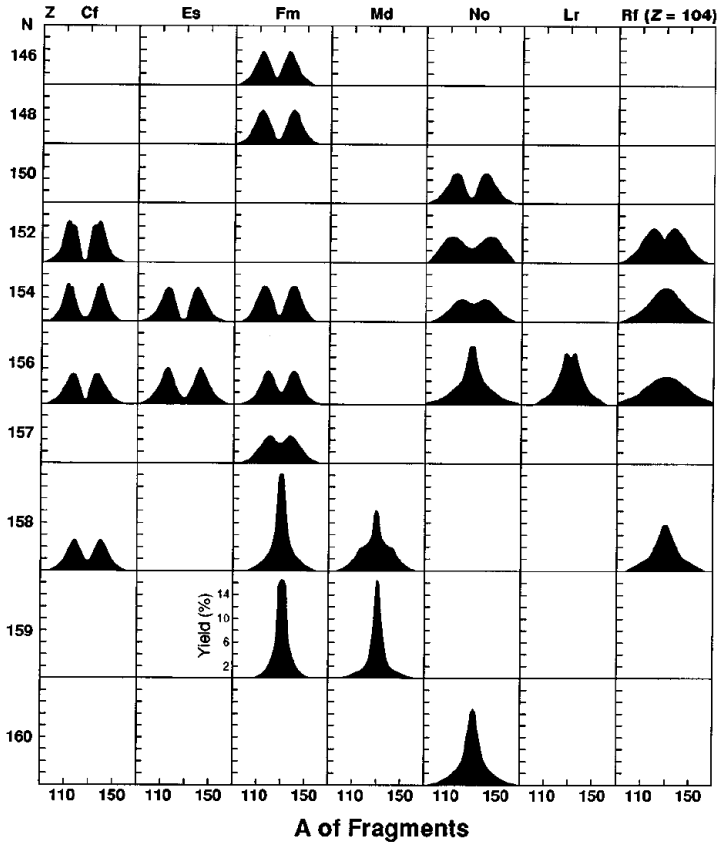

Figure 2.7: Experimental systematics of fission-fragment mass distributions for isotopes with $Z = 98$–104 [23, 31].

$$TKE = Z_1 Z_2 e^2 F(r) \tag{2.15}$$

where term $F(r)$ depends on the fragments shape and charge distribution during scission.

From a simple description of the SF process discussed in previous section it can be assumed that the origin of total kinetic energy (TKE) of fragments lies in a mutual Coulomb repulsion of two nuclei. A very simple expression can be used to describe TKE release when considering two symmetric, uniformly charged spheres of radius R touching by their surfaces. In this case $F(r) = 1/(2R)$, $A_1 = A_2 = A/2$ and $Z_1 = Z_2 = Z/2$ where the physical quantities without indexes refer to the fissioning nucleus and indexes 1 and 2 refer to the first and second fission fragment. The mutual repulsion can be written as

$$TKE = \frac{\left(\frac{Ze}{2}\right)^2}{2R} = \frac{e^2}{2^{8/3} r_0}\left(\frac{Z^2}{A^{1/3}}\right) \tag{2.16}$$

where the nuclear radius was expressed as $R = r_0(A/2)^{1/3}$ with r_0 nuclear radius parameter [32]. The dependence of the $\overline{TKE}$ experimental data on the $\frac{Z^2}{A^{1/3}}$, a.k.a. Viola-Seaborg systematics, is shown in Fig. 2.8. The $\overline{TKE}$ of asymmetrically fissioning isotopes is linearly increasing with $\frac{Z^2}{A^{1/3}}$. The group of symmetrically fissioning isotopes shows increased values of $\overline{TKE}$ and does not fit to the linear trend.

From fitting of the experimental data to Eq. 2.16 the value of 1.8 fm for nuclear radius parameter can be extracted instead of typical $r_0 = 1.2-1.3$ fm. The most convincing explanation is based on the strong prolate deformation of fission fragments after the scission [32].

For a rough estimation of the TKE release in fission a very simple equation that works pretty well over a wide range of nuclei can be used [33]:

$$TKE = \frac{Z_1 Z_2 e^2}{1.8(A_1^{1/3} + A_2^{1/3})}\text{MeV} \tag{2.17}$$

2.1.6 Bimodal fission

Measurements of TKE distributions revealed the possibility of bimodal fission for several isotopes in trans-fermium region. The phenomenon of bimodal fission can be explained as a coexistence of two fission modes for the SF

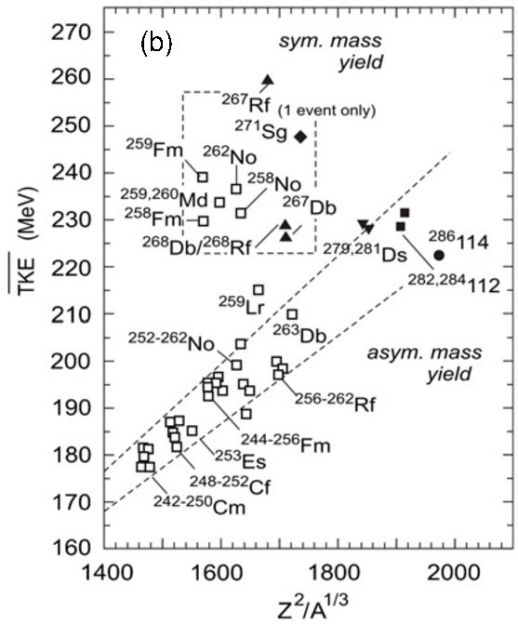

Figure 2.8: $\overline{TKE}$ from spontaneous fission variation with $\frac{Z^2}{A^{1/3}}$ [24].

of an isotope. These two modes are characterized by significantly different $\overline{TKE}$. The calculations of potential-energy surfaces revealed two different paths to fission, the first following the liquid-drop model and the second influenced by shell effects. The liquid-drop model like path leads to a fission from elongated shapes of fission fragments at the scission point. This fission mode is typically characterized by lower $\overline{TKE}$ values. The shell-effect path leads to a fission from compact shapes and the $\overline{TKE}$ are higher by ≈35 MeV. The competition of these two modes and thus a visible change in measured $\overline{TKE}$ is discussed in recent theoretical calculations where the possibility of bimodal fission for even Fm and Rf isotopes is reported [3].

In this study, the total deformation energy was calculated at the scission point using the Strutinsky procedure (macroscopic-microscopic approach). The shapes of fragments just before the separation was described by Cassinian ovals with three additional shape parameters, corresponding to mass asymmetry, quadrupole deformation and elongation. A part of the results, including fission-fragment mass distributions and TKE for even rutherfordium isotopes ^{254}Rf–^{268}Rf is shown in Fig. 2.9. One fission mode corresponds to fission from elongated shape and another from compact shape (blue and red, respectively, in Fig. 2.9).

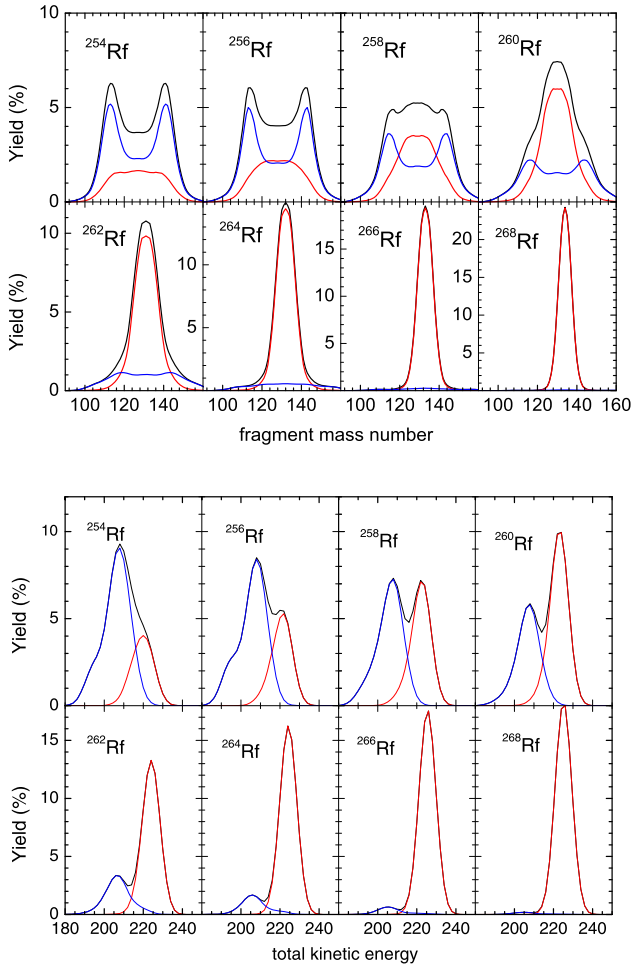

Figure 2.9: Fission-fragment mass distributions (top) and total kinetic energies (bottom) for even rutherfordium isotopes ^{254}Rf–^{268}Rf calculated in [3]. Two competing fission modes are present, from the elongated shape (blue), from the compact shape (red).

At mass number $A = 254$ the lower-energy (elongated), mass asymmetric mode (elongated) is slightly dominant over higher-energy (compact), rather mass asymmetric mode. With increasing mass the higher-energy mode becomes more dominant and also changes the mass distribution from asymmetric to narrow symmetric at the same time. At mass number $A = 258$ the both modes have the same probabilities.

Experimental studies of mass and TKE distributions confirmed the concept of bimodal fission in lighter nuclei up to nobelium (e.g. ^{258}Fm, ^{259,260}Md or ^{258,260}No) [4, 5]. However until now, only few results with limited statistics of SF events with measured total kinetic energy were obtained for rutherfordium ($Z = 104$) isotopes [4, 5, 6].

2.1.7 Neutron emission

Most part of the energy released in SF process is transformed into the TKE of fragments, the rest of this energy goes to the excitation of fragments. Due to the conservation of ratio N/Z of fissioning nucleus, the created fragments are in the neutron rich region. The de-excitation of fragments (fully-accelerated) is mainly performed by the emission of prompt neutrons, that take away the most of the excitation energy. Prompt γ rays are released too and the rest of the energy is emitted in the form of β particles, neutrinos, delayed neutrons, etc. [33].

The average number v_T of prompt neutrons emitted from fission fragments is a unique characteristic of every fissioning isotope. The multiplicity is increasing with the excitation energy of fragments, which is rising with the mass of fissioning nucleus. In Fig. 2.10 the dependence of neutron multiplicities on the mass A can be clearly seen. It is expected, that for very heavy isotopes v_T will be about 7 [33].

2.2 Internal conversion

Internal coversion (IC) is a de-excitation process of a nucleus in excited state, competing with internal transition via γ rays. Excited nucleus interacts with electron from atomic orbital via electromagnetic interaction. The excitation energy of nucleus is transferred to electron, which is emitted from the atom with kinetic energy E_{CE} as

$$E_{CE} = \Delta E - B_e \tag{2.18}$$

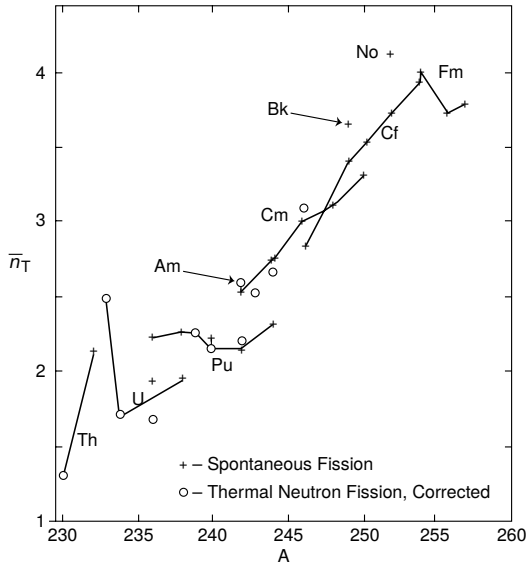

Figure 2.10: Average number of prompt neutrons emitted in spontaneous and induced fission dependence on the mass of fissioning nucleus [23].

where ΔE is the transition energy (excitation energy of a nucleus) and B_e is a binding energy of an electron in the atomic orbital. The electron energy E_{CE} depends on the orbital from which the electrons interacted (K, L, M, ...). Therefore, we observe lines corresponding to each orbital in the spectrum of electron energies. An example of the energy spectrum of conversion electrons from the β decay of ^{198}Hg is on Fig. 2.11. This isotope undergoes β^- decay $^{198}\mathrm{Hg} \rightarrow {}^{198}\mathrm{Tl}$ with $Q = 0.96\,\mathrm{MeV}$ and populates a 2^+ state in ^{198}Tl at excitation energy of $0.412\,\mathrm{MeV}$ [33]. Deexcitation via internal conversion leads to the ground state. Emitted electrons have energies equals to the energy difference of the 2^+ and ground states, lowered by the binding energy of K, L, M orbitals, which can be observable in electron energy spectrum as lines. After the internal conversion, there is a vacancy in electron shell, leading to a de-excitation via X-rays or Auger electrons. The energies of Auger electrons are also observable in Fig. 2.11. The competition between γ transition and internal conversion is characterized by conversion coefficient which is determined as

$$\alpha = \frac{\lambda_{IC}}{\lambda_\gamma} = \frac{number\,of\,transitions\,via\,IC}{number\,of\,transitions\,via\,\gamma\,decay} \tag{2.19}$$

Conversion coefficients can be roughly estimated via formulas

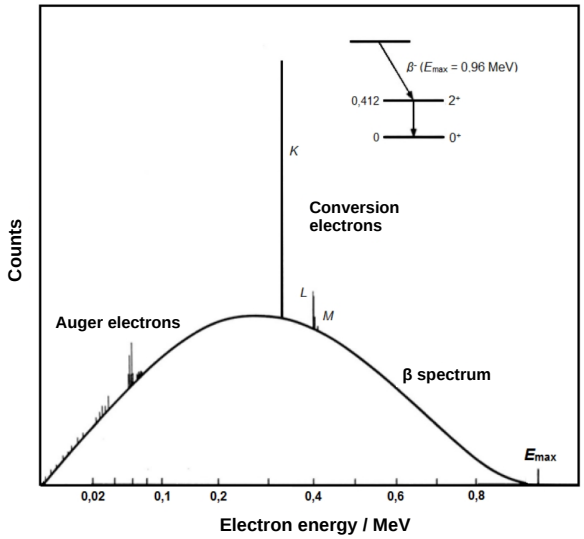

Figure 2.11: Energy spectrum of electrons from the β^- decay ^{198}Hg $\rightarrow$ ^{198}Tl with $Q = 0.96\,\mathrm{MeV}$, which populates a 2^+ state in ^{198}Tl at excitation energy of $0.412\,\mathrm{MeV}$. The deexcitation to ground state via internal conversion is observable as K, L and M lines in the spectrum. Auger electrons from the deexcitation of atomic shell are also visible.

$$\alpha(EL) = \frac{Z^3}{n^3}\frac{L}{L+1}\left(\frac{e^2}{4\pi\varepsilon_0\hbar c}\right)^4\left(\frac{2m_ec^2}{E}\right)^{L+5/2} \tag{2.20}$$

$$\alpha(ML) = \frac{Z^3}{n^3}\left(\frac{e^2}{4\pi\varepsilon_0\hbar c}\right)^4\left(\frac{2m_ec^2}{E}\right)^{L+3/2} \tag{2.21}$$

where EL is an electric transition with multipolarity L, ML is a magnetic transition with multipolarity L, Z is proton number of nucleus, n is the main quantum number of an electron in electron shell, $4\pi\varepsilon_0\hbar c$ is a fine structure constant. It is obvious that due to the dependence on Z^3 the internal conversion is especially important for very heavy nuclei.

2.3 Nuclear isomerism

Nuclear isomers are long-lived metastable states of atomic nuclei. The name of nuclear isomerism was derived from chemical isomers due to some analogy. Chemical isomers have the same molecular formulas, they consist of the same

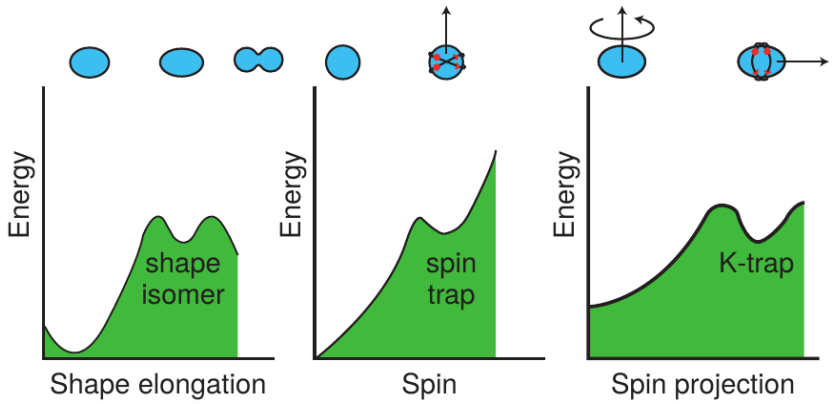

Figure 2.12: Three types of isomers [34].

particles, but arranged in different physical configurations. Nuclear isomers conisist of the same nucleons, but with different orbital configuration. While typical energies for chemical isomers are in eV, in the case of nuclear isomers the excitation energies may reach up to several MeV.

The de-excitation half-lives of such states may vary. There is not a strict definition of a minimum half-life for excited state to be called "isomeric". The definition of "long-lived" may be understood as long enough for the atomic structure to be formed. From the experimental point of view it can be considered as experimentally measurable time. Typically the lower limit is consider to be 10^{-9}s, while the half-life of isomers may reach up to 10^{15} years as in the of ^{180}Ta. This half-life is comparable to the formation of the Earth, making $^{180}\mathrm{Ta}^{m}$ to be the only naturally occurring isomer.

The existence of the isomers itself is allowed when there is a secondary minimum in the potential energy dependence on some nuclear variables, such as shape elongation, spin or the projection of spin into the symmetry axis (see Fig. 2.12). When a nuclei find itself in the secondary minimum, a small change in one of nuclear variables may lead only to state with higher excitation energy. A transition which would lead to energetically more favourable state demands a large change in either shape elongation or spin or spin projection.

2.3.1 Shape isomers

Shape isomers (left on Fig. 2.12), also called fissioning isomers appear, when during elongation a nucleus is stuck in the secondary minimum of double-humped fission barrier. There are two possibilities for a nucleus in this state; either it deexcites after some time towards the less elongated ground state via γ transitions or if the secondary barrier is low enough, nucleus can continue to elongate and undergo fission via tunneling effect through the barrier. An example of this kind of isomer can be find in ^{242}Am, where the low-lying nuclear isomeric state has half-life of 141 years while the fissioning isomeric state with excitation energy of 2.2 MeV has half-life of only 14 ms due to the thinner secondary barrier.

2.3.2 Spin isomers

Spin isomers occurs when the nucleus is stuck in an excited state with spin much different than state with lower excitation energies. A deexcitation into lower states would require a large change in spin and therefore an emission of a γ ray with high multipolarity to match the spin change. Such a transition is strongly hindered, giving rise to a long-lived spin isomer. An example of such in isomer is $^{180}\mathrm{Ta}^{m}$ with spin difference between isomeric and ground state $\Delta I = 8$ deexciting via strongly hindered γ transition with multipolarity $\lambda = 8$, resulting in an extremely large half-life of 10^{15} years.

2.3.3 K isomers

In deformed, axially symmetric nuclei, the quantum number K is defined as the projection of total nuclear spin Ω, onto the symmetry axis. By breaking nucleon pairs, multi-quasiparticle (qp) configurations with high-K value are possible (typically 2-qp or 4-qp configuration for even-even and 3-qp for odd-even or even-odd isotopes). The selection rules for electromagnetic transitions require the multipolarity of the decay radiation at least as large as the change in the K value [35]. These rules give rise to K isomers, the metastable, relatively long-lived states with high K. Detailed spectroscopic studies of nuclei near the deformed shells $Z = 100$ and $N = 152$ where the presence of K isomers was found, serve us as a strong tool for investigations into the superheavy elements properties. High-K isomers are of special interest with respect to the properties of superheavy isotopes as their hindrance

against spontaneous fission or alpha decay may lead to existence of states exceeding the lifetime of the ground state. An example can be found in ^{270}Ds, where the reported half-lives for the ground state and high-K isomeric states are $T_{1/2}(g.s.) = 100^{+140}_{-40}\mu$s and $T_{1/2}(i.s.) = 6.0^{+8.2}_{-2.2}$ms [36].

In the transfermium region, the existence of K-isomeric states was previously confirmed in several even-even isotopes (e.g. ^{252}No [7], ^{254}No [8, 9, 10], ^{254}Rf [11], ^{256}Rf [12, 13]), and odd-even or even-odd isotopes (e.g. ^{253}No [14, 15], ^{255}Lr [16, 17], ^{257}Rf [18]).

2.4 Compound nucleus reactions

The idea of compound nucleus reactions (a.k.a. reactions of complete fusion or fusion-evaporation reactions) is based on an assumption that a projectile a accelerated to the energy T_α (in laboratory system) hits the stationary target nucleus X in a way that the impact parameter is small compared to the size of nucleus. The hitting projectile overcomes the Coulomb barrier, enters the target nucleus and interacts there with individual nucleons by scattering. Scattered nucleons also interact with other nucleons. After a series of interactions all of the projectile kinetic energy is redistributed among all nucleons. By this mechanism the projectile becomes stuck in the target nucleus, forming a heavier system called "compound nucleus" (CN). The probability of the formation process depends on the energy of incident projectile and available quantum levels in the target nucleus. After the energy redistribution, the CN is in a state of high excitation and high angular momentum. The de-excitation is done firstly by the emission of protons, neutrons and alpha particles and later by γ quanta. The rest of the CN after the evaporation and final de-excitation is called "evaporation residue" (ER) and can be considered as the final product of the reaction. The CN formation takes $\sim 10^{-22}$ s. The whole process can be schematically represented as

$$a + X \longrightarrow CN^* \longrightarrow Y + b \tag{2.22}$$

where the b can be understood as all evaporated particles (protons, neutrons, α) from the CN. The a (projectile) and X (target) represent input channel of the reaction, while the Y and b are output channel. In CN^* the asterisk stands for the excited state. The excitation energy can be approximately defined as

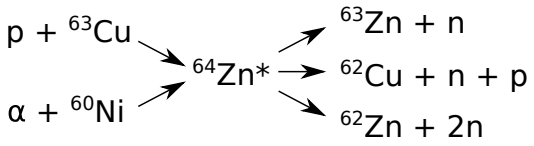

Figure 2.13: Two different input channels leading to the same compound nucleus. Three possible output channels are independent on the way the compound nucleus was formed [37].

$$E^* = Q + (\frac{m_X}{m_X + m_a})T_a \tag{2.23}$$

where the Q value of the reaction is

$$Q = (m_a + m_X - m_{CN^*})c^2 \tag{2.24}$$

and m_a, m_X and m_{CN^*} are the masses of projectile, target and compound nucleus. Typically $E^* = (30 - 60)\,\mathrm{MeV}$. The average binding energy per nucleon for heavy nuclei is about $(7-8)\,\mathrm{MeV}$. Although the incident projectile bring significant amount of energy to the CN, it is redistributed among $200-250$ nucleons. The average gain of energy per nucleon is not enough for any nucleon to escape the nucleus. Due to the random collisions between nucleons it is possible that enough amount of energy will be concentrated into one nucleon which can be evaporated. The process of nucleon emission takes $\sim 10^{-19}\,\mathrm{s}$. Later ($\sim 10^{-17} - 10^{-10}\,\mathrm{s}$) the evaporation residue is de-exciting by the emission of γ quanta until it reaches the ground state. The probability of reaction to take place is characterized by a cross-section σ. It can be determined experimentally from the number of projectiles N_{proj} incident on the target with surface density of target nuclei n and the number of produced evaporation residues N_{ER} as

$$N_{ER} = \sigma N_{proj} n \tag{2.25}$$

The compound nucleus reaction can be considered as a two step process - the CN formation and particle evaporation. The main idea is the assumption that the creation probability of final products is independent on the way the CN was formed. In other words, the two steps are completely independent.

The concept of compound nucleus reactions was experimentally confirmed in Berkeley in 1950 [37] on a CN ^{64}Zn which was formed by two different input channels - in reactions $\mathrm{p} + {}^{63}\mathrm{Cu}$ and $\alpha + {}^{60}\mathrm{Ni}$. Three different reaction

outputs were observed: $^{63}\mathrm{Zn} + \mathrm{n}$, $^{62}\mathrm{Cu} + \mathrm{n} + \mathrm{p}$ and $^{62}\mathrm{Zn} + 2\mathrm{n}$. The reaction is schematically represented in Fig. 2.13. It was expected that weather the CN ^{64}Zn is created in one reaction or another (but with the same excitation energy), the cross-sections for the final products creation will be the same. That would allow to write the cross-section $\sigma(a, b)$ of the reaction with the input a, X and output Y, b as a product of the probabilities of two reaction steps

$$\sigma(a, b) = \sigma_{CN^*}(a, X, T_a)P(b, E^*) \tag{2.26}$$

where $\sigma_{CN^*}(a, X, T_a)$ represent the absorption of projectile a with kinetic energy T_a by a target nucleus X resulting the formation of compound nucleus CN^* and $P(b, E^*)$ stands for the probability of CN with excitation energy E^* to evaporate b particles and to create the final product Y.

To produce the same evaporation residue with the same CN of the same excitation energy but by a different inputs $a' + X'$, the cross-section is analogically

$$\sigma(a, b) = \sigma_{CN^*}(a', X', T'_a)P(b, E^*) \tag{2.27}$$

From the Eq. 2.24 it can be understood that in order to obtain the same excitation energy E^* when changing from a, X to a', X' the change from T_a to T'_a is necessary due to the differences in binding energies of both cases.

When considering a creation of an output Y', b' instead of Y, b from the CN formed by $a+X$ and $a'+X'$, the corresponding cross-sections are obtained

$$\sigma(a, b') = \sigma_{CN^*}(a, X, T_a)P(b', E^*) \tag{2.28}$$

$$\sigma(a', b') = \sigma_{CN^*}(a', X', T'_a)P(b', E^*) \tag{2.29}$$

From the Eqs. 2.26, 2.27, 2.28 and 2.29 one can conclude the ratio for cross-sections

$$\frac{\sigma(a, b)}{\sigma(a, b')} = \frac{P(b, E^*)}{P(b', E^*)} = \frac{\sigma(a', b)}{\sigma(a', b')} \tag{2.30}$$

The results of discussed experiment from [37] showed that the dependence between laboratory energy of incident protons and cross-sections of reactions (p, n), (p, pn), $(p, 2n)$ with target nuclei ^{63}Cu have the same character as the dependence between laboratory energy of incident αs (shifted by 7 MeV

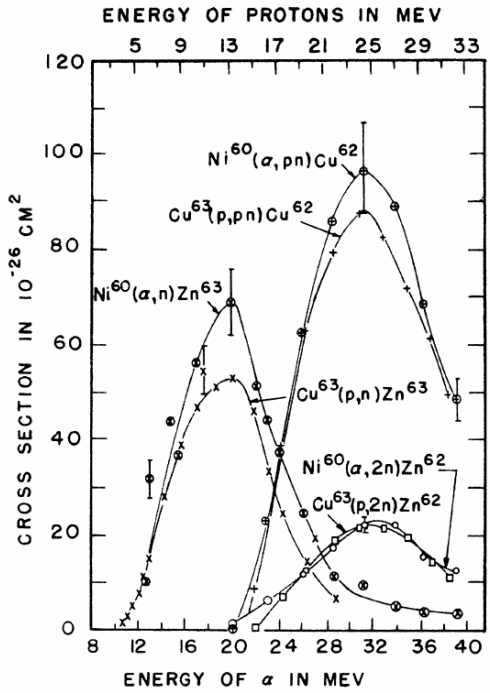

Figure 2.14: Cross-sections of reactions (p,n), (p,pn), $(p,2n)$ with target nuclei ^{63}Cu and reactions (α,n), (α,pn) and $(\alpha,2n)$ with target nuclei ^{60}Zn, depending on the laboratory energy of incident protons and α particles [37].

to represent the same excitation energies of compound nucleus) and cross-sections of reactions (α,n), (α,pn) and $(\alpha,2n)$ with target nuclei ^{60}Zn, which is shown in Fig. 2.14. Within the error bars the cross-section ratios $\sigma(p,n) : \sigma(p,pn) : \sigma(p,2n)$ agree to the ratios $\sigma(\alpha,n) : \sigma(\alpha,pn) : \sigma(\alpha,2n)$ which confirms the validity of Eq. 2.30.

This type of nuclear reactions is nowadays the only possible method of producing much heavier nuclei than those participating in the reaction itself and thus represents a unique possibility of production of the heaviest nuclei. Moreover, due to their properties, these reactions are an excellent tool for the study of nuclei in the state of high energy and high angular momentum.

The particles evaporated during the CN de-excitation have energies with a Maxwellian distribution. If the emitted particles are neutrons, the energy spectrum is shown in Fig. 2.14 and the distribution can be expressed as

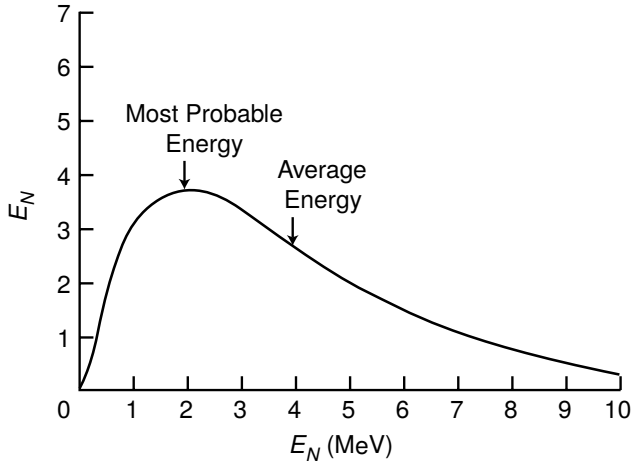

Figure 2.15: Energy spectrum of neutrons evaporated from the compound nucleus [33].

$$N(\varepsilon)d\varepsilon = \frac{\varepsilon}{T^2} exp\Big(\frac{-\varepsilon}{T}\Big)d\varepsilon \tag{2.31}$$

where ε refers the energy of projectile nucleus and T is nuclear temperature given by

$$E^* = aT^2 - T \tag{2.32}$$

with a being the *level density parameter* of the excited nucleus, $A/12 - A/8$ (from Fermi gas model).

The most probable energy of emitted neutron is T while the average energy is $2T$. Thus the CN "evaporates" neutrons just like molecules are being evaporated from the surface of a hot water. Charged particles (protons, α particles) can be emitted from the CN as well with a difference that the minimal possible kinetic energy is not zero as in case of neutrons. Instead, the threshold energy for the emission of charged particle ε_S (which approximately corresponds to a Coulomb barrier) determines the minimal energy of evaporated charged particles. The energy spectrum in this case is

$$N(\varepsilon)d\varepsilon = \frac{\varepsilon - \varepsilon_S}{T^2} exp\Big(\frac{-\varepsilon - \varepsilon_S}{T}\Big)d\varepsilon \tag{2.33}$$

[33].

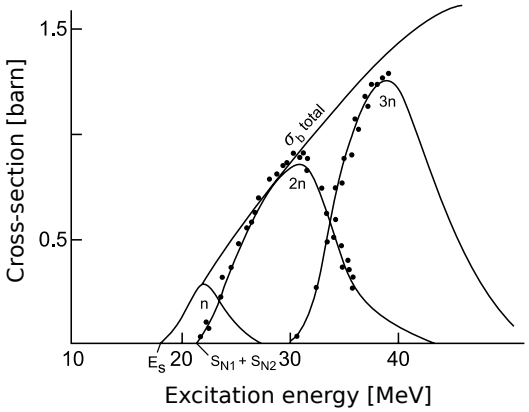

Figure 2.16: Excitation function - cross-section variation with the excitation energy of the compound nucleus [33].

2.4.1 Excitation energy vs. cross-sections

The dependence of compound nucleus reaction cross-section on the excitation energy of CN (and thus the laboratory energy of projectile) is evident and characteristic. For a demonstrative example, the excitation function of fusion-evaporation reaction of $\alpha + {}^{209}$Bi is shown in Fig. 2.16. Depending on the excitation energy of CN ^{213}At the multiplicities of x neutrons are evaporated with different cross-sections (resulting in final products $^{213\text{-x}}$At).

The cross-section of reaction $^{209}\text{Bi}(\alpha, xn)^{213\text{-x}}$At discussed above is zero until a certain excitation energy E_S. This excitation energy corresponds to a minimal energy of projectiles, which allow the nuclei to overcome the fusion barrier and therefore the formation of CN. From this point, the CN formation cross-section increases because the overcoming of fusion barrier becomes more probable. Fusion barrier is also the reason for typically hindered 1n evaporation channel as can be see in Fig. 2.16. Other evaporation channels can be also affected and slightly hindered. On the other side, with the increase of excitation energy, the probability of CN fission is rising, so from a certain point at higher energies the CN formation cross-section starts to decrease. In the other words, the CN formation cross-section dependence on excitation energy can be characterized as a competition between two processes - overcoming the fusion barrier and immediate fission - where probabilities of both are rising with increased excitation energy.

As was shown in previous section in Fig. 2.15, the average energy of evaporated neutrons is $2T$. The neutron separation energy is S_N. By the

evaporation of the first neutron $N1$, the average decrease of CN excitation energy is $S_{N1} + 2T$. To evaporate the second neutron $N2$ the average energy "consumption" is $S_{N1} + 2T$ and so on (we consider T to be constant). From experimental experiences it can be approximately said that one evaporated particle takes away the amount of about 10 MeV from CN excitation energy. The creation of final product through $1n$ evaporation channel become possible only when the excitation energy of CN is above the first neutron separation energy S_{N1} (and of course above E_S corresponding to fusion barrier). The two-neutron evaporation channel will be available at excitation energies above $S_{N1} + S_{N2}$, three-neutron channel at $S_{N1} + S_{N2} + S_{N3}$ and so on. The peaks of particular xn evaporation channels are expected at $S_N1 + 2T$, $S_N1 + S_N2 + 4T$, $S_{N1} + S_{N2} + S_{N3} + 6T$ and so on [33]. From experimental data the distances between the positions of this peaks are usually about 10 MeV, which confirms the fact that each neutron takes away about 10 MeV of excitation energy from CN. The positions of peaks use to be shifted to higher excitation energies. It can be seen in Fig. 2.16 where the 2n-peak position is at 30 MeV and the position of 3n peak is at 40 MeV even though to evaporate 2 and 3 neutrons the energy of about 2×10 MeV and 3×10 MeV is needed. In order to explain this shift it is necessary to include the angular momentum of highly excited CN into consideration. In Fig. 2.17 the *yrast* line is showed. It is a technical term referring to the state of nucleus with minimal possible excitation energy for given angular momentum. A CN, which is typically excited to $30 - 70$ MeV, has angular momentum of $60 - 80\,\hbar$. At first the de-excitation goes by the emission of nucleons or α particles. As was mentioned before, every evaporated particle takes away about 10 MeV but the decrease of angular momentum is only very slight. After evaporating some particles the CN approaches the yrast line and appears in the state where another particle emission would result in a state below the yrast line and thus is not possible. By the emission of "statistical" γ transitions the CN is cooling off until it reaches the yrast line. Consequently only the de-excitation along this line is possible and so called "yrast cascade" is emitted. The mentioned shift of cross-section peaks is thus mainly cased by the impossibility for CN to cross the yrast line and necessity to cool down by γ quanta [38].

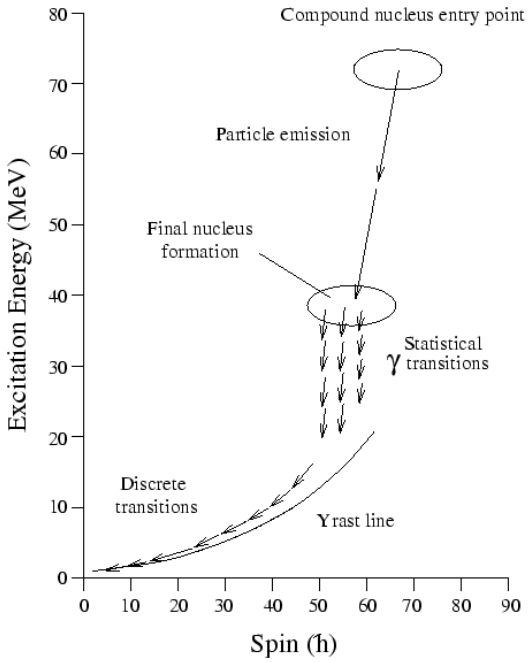

Figure 2.17: Yrast line is representing a state of the nucleus with minimal possible excitation energy for given angular momentum.

Chapter 3

Experiment description

3.1 Velocity filter SHIP

SHIP (Separator for Heavy Ion reaction Products) uses specific kinematic properties of fusion-evaporation reaction products to separate them from projectiles that did not react in the target and from other undesired produced nuclei. The separator (configuration showed in Fig. 3.1) is placed in the direction of beam from UNILAC (UNIversal Linear ACcelerator).

The 120 m long accelerator is able to produce stable heavy ion beams from carbon to uranium of intensities up to 10^{13} particles / s with energies up to 20 MeV / u. It is working in pulsed mode of 50 Hz. One 20 ms macropulse consists of 5 ms long beam burst and 15 ms period without beam called "pause". Typical macropulse is shown in Fig. 3.2.

After being accelerated the projectiles are directed to the target material mounted on a rotating wheel construction. The photo of target is shown in Fig. 3.3. It is organized into 8 separated segments. The rotational movement of the target wheel is 18.75 Hz and is synchronized with the pulsing regime of accelerator in a way that between the 2 consequent beam bursts the wheel is moved by 18.75 Hz / 50 Hz = 0.375 turns which corresponds to a turn by 3 segments, so the sequence of segments irradiation is 1,4,7,2,5,8,3,6,1... The reason for this arrangement is to enlarge the irradiating area because of the low melting points of typically used target materials and so in order to use higher-intensity primary beams a good mechanism to redistribute the intensity is needed. Other reason for enlarging the target area is to minimize the irradiation damage. The dimensions of each target segment are 110 mm × 23 mm and the diameter of the target wheel is 310 mm.

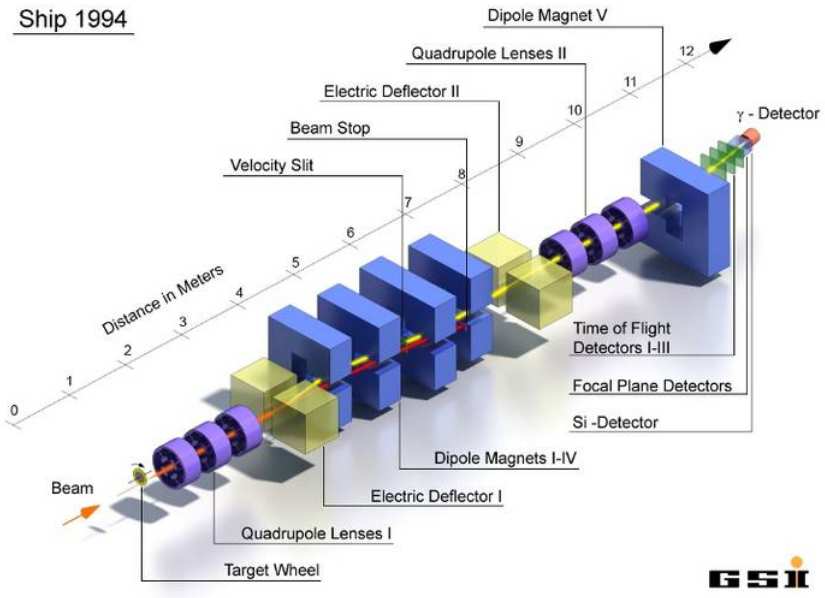

Figure 3.1: Velocity filter SHIP [39].

Due to the diffraction the reaction products leave the target under a wide range of angles from the direction of primary beam and thus the main line of the separator. A triplet of quadrupole magnets is used to focus these deflected evaporation residues. Each of the quadrupole magnets is turned by 120° to obtain a uniform focusation.

The reaction products are escaping the target with the velocities lower than the velocities of projectiles of primary beam that are simply passing through the target without interacting. It is given by the conservation law of momentum. After the interaction, compound nuclei have the same momentum as incident projectiles since the target nuclei are not moving in the direction of beam and thus their contribution to the momentum of compound nuclei is zero. The velocity of a compound nucleus produced by the fusion of target and projectile nuclei is given by

$$v_{CN} = \frac{m_p}{m_p + m_t} v_p \tag{3.1}$$

where v_{CN} stands for the velocity of compound nucleus in laboratory system, m_p and m_t are masses of projectile and target nuclei, respectively.

The fact of different velocities is the main principle used in the separator.

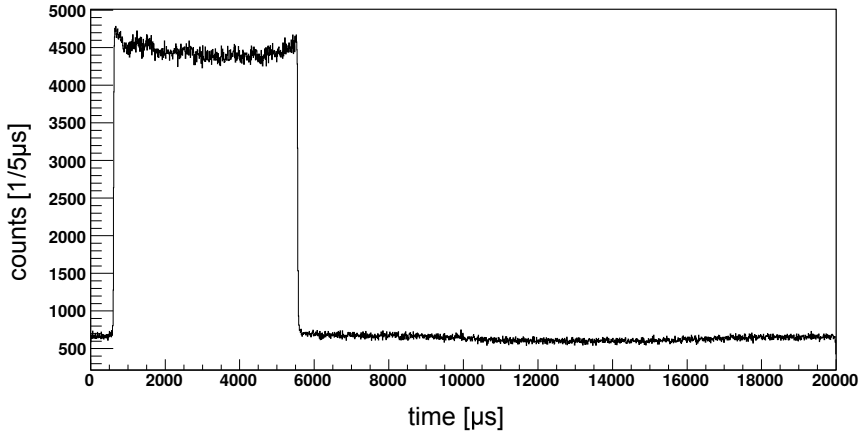

Figure 3.2: Macropulse from UNILAC composed of 5 ms beam burst and 15 ms pause.

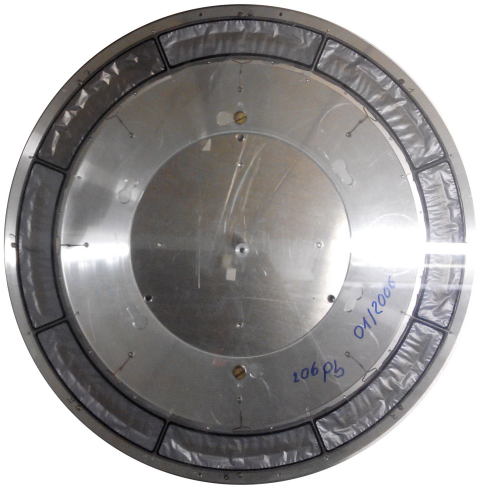

Figure 3.3: Target wheel.

The velocity filter itself consists of electrical deflecting plates and magnetic dipoles. The electrical and magnetic fields $\vec{E}$ and $\vec{B}$ are perpendicular to each other interacting with the charged particles by the Lorentz force

$$F = qE + qvB \tag{3.2}$$

where q and v are charge and velocity of the particle. When this force on the particle is zero, the particle pass through the separator. By the correct choosing of size of the variables E and B one can select a precise velocity that will be accepted by the filter ($\pm 5\,\%$). Particles with other velocities are deflected and stopped during the process of separation.

In opposite to the usual Wien filters, SHIP works with separated fields organized as electrostatic deflector I + 2 magnetic dipoles I and II followed by a mirror reversed configuration, 2 magnetic dipoles III and IV + electrostatic deflector II. Another triplet of magnetic quadrupoles is placed after the separator in order to focus the particles that did pass through the separator. The beam of separated particles is then deflected with a magnetic dipole V by 7.5° for the background suppression reasons. It helps to push out the evaporation residues from the high-energy background coming out from the separator and from the neutrons that could damage the gamma detectors [40].

3.1.1 Experimental cross-sections

The number of evaporation residues of one kind, produced in the target of experiment SHIP depends on the number of projectiles that hit the target N_{proj}, fusion-evaporation reaction cross-section σ and the density of target nuclei in the target n such as

$$N_{ER} = \sigma N_{proj} n \tag{3.3}$$

Except σ, which cannot be determined directly, it is possible to evaluate all the other members in eq. 3.3. The number of ER produced in the reaction can be estimated via the number of radioactive decay detected in the detection setup. If the half-life of radioactive decay i (eg. α decay or SF) is way shorter in comparison with the time of measurement, one can consider the number of detected radioactive decays N_i, corrected by branching ratio b_i and detection efficiency of radioative decay i, to be equal to the number of ER that were implanted into the STOP detector. If this number is then

corrected by the transmission of SHIP separator for given reaction, one can obtain the number of ER produced in the target.

$$N_{ER} = \frac{N_i}{\varepsilon_{sep}\, b_i\, \varepsilon_{det,i}} \tag{3.4}$$

The number of projectiles hitting the target can be estimated from the beam properties. The beam current I_{peak} multiplied by the time of measurement $t_{measurement}$ is equal to the total charge of projectile particles that hit the target. Dividing this number by charge of single projectile gives the total number of projectiles. Due to the pulsing mode of UNILAC accelator, this number must be corrected to the ratio of t_{pulse} and $t_{macropulse}$.

$$N_{proj} = \frac{I_{peak}}{q} \frac{t_{pulse}}{t_{macropulse}}\, t_{measurement} \tag{3.5}$$

The density of target nuclei in the target can be estimated as

$$n = f\frac{N_{trg}}{S} = f\frac{\frac{m}{M_m}N_A}{S} = f\frac{N_A}{M_m}d \tag{3.6}$$

where f is the isotopic purity of target material, N_{trg} is the number of target nuclei in the target, S is the target surface, m is the target mass, M_m is the mass of one mol of target nuclei, N_A is Avogadro number and d is the target thickness in kg/m^2. From the equations 3.4, 3.5, 3.6 one can finally determine the reaction cross-section as

$$\sigma = \frac{N_{ER}}{N_{proj}}\frac{1}{n} = \frac{\frac{N_i}{\varepsilon_{sep}\, b_i\, \varepsilon_{det,i}}}{\frac{I_{peak}}{q}\frac{t_{pulse}}{t_{macropulse}}\, t_{measurement}} \frac{M_m}{f d N_A} \tag{3.7}$$

3.2 Detectors

Selection of suitable detectors depends on the type of detecting particles, their energies, type of expected radioactive decay, half-life, intensity, etc. Neutron deficient isotopes in the transfermium region produced at SHIP are mostly undergoing α decay, SF and EC/β^+ decay with a wide range of half-lives (from microseconds to minutes). Spontaneous fission is always accompanied by the emission of γ rays and so is the de-excitation of possibly present isomeric states (even though the de-excitation by internal conversion

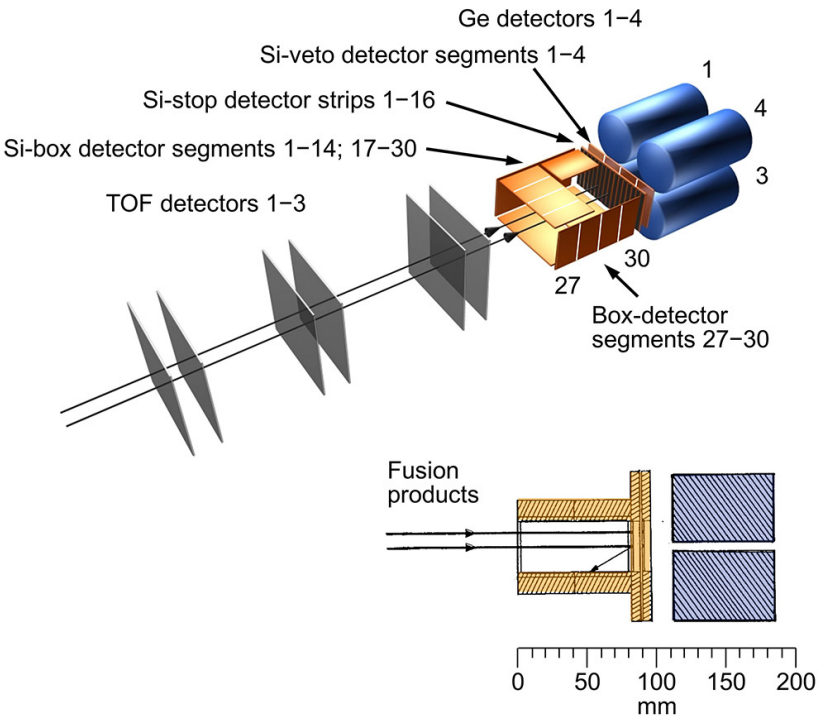

Figure 3.4: Detection system at velocity filter SHIP [41].

is in many cases more probable and accompanied by X-rays and Auger electrons). The detection system at SHIP in Fig. 3.4 was built to fulfill these demands as much as possible.

TOF

The evaporation residues firstly pass through a triplet of TOF detectors [42]. Each of three TOF systems consists of a carbon foil of $55\,\mathrm{cm}^2$ surface and $30\,\mu\mathrm{g/cm}^2$ thickness and a parallel mesh. Electric potential difference of $400\,\mathrm{kV}$ is applied between the foil and the mesh creating electric field $\vec{E}$. A homogeneous magnetic field $\vec{B}$ is also applied. Evaporation residues passing through the carbon foil eject electrons which are accelerated by $\vec{E}$. The presence of $\vec{B}$ is twisting the electron direction into the circular motion. The electrons are directed into the micro-channel plates where they are collected creating a signal. One of the main purposes of this detectors is to distinguish between implanted particles (with TOF signals) and particles from the decay

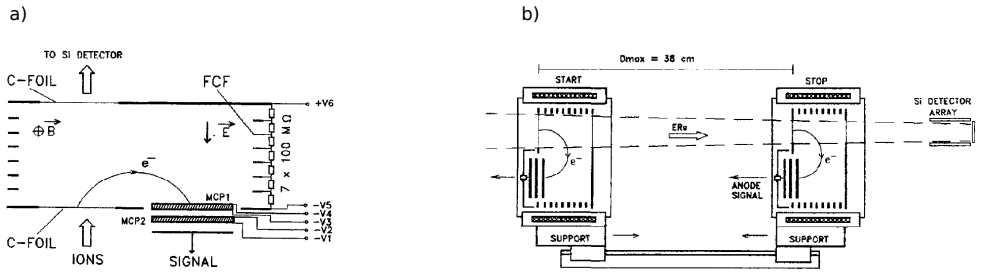

Figure 3.5: a) working scheme of a unit of time-of-flight system, b) schematic view of arrangement of time-of-flight system at velocity filter SHIP [42].

(without TOF signals) and thus suppress the background in spectra. The types of particles (e.q. evaporation residues, transfer products, projectiles,...) flying through the TOF system can be distinguish using their different kinematic properties - different time-of-flights and energies.

STOP

Evaporation residues that passed through the separator and TOF system are implanted into the position-sensitive silicon strip detector with 16 strips also called as the "STOP" detector. Each of the strips represents an individual y-position sensitive detector 5 mm wide and 35 mm long. The active area of the whole STOP detector is 80 mm x 35 mm. Considering the y position resolution of each strip (about 150 μm FWHM for an α source) the system behaves as a set of 3700 small detectors with dimensions 5 mm x 0.15 mm. For an external α source of ^{241}Am the energy resolution is about 14 keV. In real situations when α particles are emitted by an implanted evaporation residue in the STOP detector, the FWHM is worsen a little bit to $(20 - 25)$ keV.

BOX

The system of six silicon strip detectors organized in "box" geometry is placed just in front of the STOP detector in order to detect particles escaping from the STOP detector in backwards direction. This configuration provides geometrical efficiency of 80 % from 2π half-space in front of the STOP detector.

CLOVER

The detection of γ rays and X-rays is achieved by the CLOVER detector composed of four Ge crystals, which is installed very close behind the STOP detector.

3.2.1 Some remarks on detection of α and SF activities using SHIP detection setup

The decaying evaporation residues implanted into the STOP detector (the implantation depths are typically few micrometers) remain in this place until their decay. During the decay (e.g. α) the Q-value of the α decay is distributed among the α particle and recoiling mother nucleus with respect to the momentum and energy conservation laws. The situation is clearly different to the measurements with external sources:

- the measured signal amplitude is the pile-up of α-particle amplitude and recoiling daughter nucleus amplitude,
- the particles are not passing through the dead layer at the surface of the detector as in the case of external source

The implantation depth of ERs into the focal plane detector is typically a few µm while the range of fission fragments in silicon is 10–20 µm. When registering SF of evaporation residues implanted in the STOP detector, three different situations can occur. Considering a 180° angle between the fission fragments, there is $\approx$ 60% probability (strongly depending on the ER implantation depth in the STOP detector) that both fragments are stopped in the STOP detector [Fig. 3.6a)]. The remaining part are events ($\approx$ 40% of all) when one fragment escapes from the STOP detector in backward direction. In this case there is $\approx$ 80% probability for the escaped fragment to be detected by the BOX detector [denoted here as STOP-BOX coincidences; see Fig. 3.6b)]. The remaining $\approx$ 20% of the escaping fragments are not fully detected [Fig. 3.6c)]. Since fission events with one escaped fragment not registered by the BOX cannot be separated from the events with both fragments being stopped in the STOP detector, we refer to both cases as "STOP-BOX anticoincidences". In the cases with one fragment completely escaped from the detection system, the fission energy cannot be fully reconstructed. The presence of these events in the spectrum results in a low-energy tail (for more details see [43]).

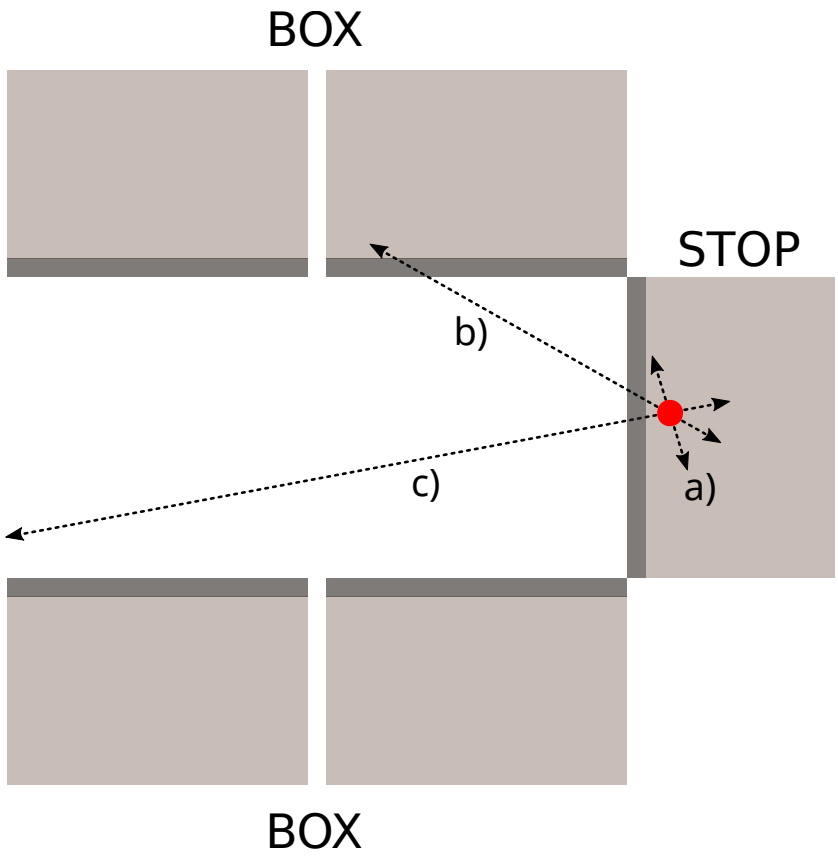

Figure 3.6: Schematic view (not to scale) of STOP and BOX detectors registering fragments from SF of an implanted nucleus (side view with respect to the direction of implantation). Red circle represents an evaporation residue implanted into the STOP detector, arrows represent the directions of 2 fission fragments. Active area of Si detectors is in bright grey color, dead layers are in dark grey. From the geometrical point of view, three possible cases can occur:
a) STOP-BOX anticoincidence (both fragments stay in STOP),
b) STOP-BOX coincidence (one fragment escapes to BOX),
c) STOP-BOX anticoincidence (one completely escaped fragment).
We note, scenarios a) and b) allow us to reconstruct the TKE completely, while c) does not.

3.2.2 Calibrations

The detection system of SHIP consists of many detectors as was discussed in previous sections. In the case of strip detectors, each strip represents one detector and so does each crystal in CLOVER. The strips of STOP and BOX detectors are connected to two electronic branches with different amplifications. In order to make this complex system of detectors to work properly which means to show the correct energies (in the case of silicon detectors also positions), it is necessary to prepare a very precise calibrations. Besides the usual calibration as a relation between the response of the detector and the real energy of the particle this also includes some calibrations to correct some electronic effects and effects worsening the position coordinates in the detector. All types of calibrations and other corrections used for the analysis of data from SHIP are discussed below.

Ballistic calibration

One of the properties of Si detectors used at SHIP is that the signal amplitude depends on the position in the strip from were the signal originates (the position of particle detection). Two same-type particles of identical energies incident to different positions in the same strip would generate signals with different amplitudes. This effect, called "ballistic deficit", is caused by different charge-collection times and it is worsening the energy resolution of each strip of STOP detector. The correction to this effect is obtained by choosing an α line with well-known energy and experimentally searching for a 2^{nd}-order-polynomial dependence between an energy differences from the real energy ΔE of each detected event and the vertical position in the strip y from where the signal originated

$$\Delta E = k_1 + k_2 y + k_3 y^2 \tag{3.8}$$

where k_1, k_2, k_3 are calibration coefficients. The example of the ballistic calibration of 2^{nd} strip from the STOP detector is shown in Fig. 3.7. α particles generated signals at different y positions of the strip. Without the ballistic effect all events would be distributed Gaussially along $\Delta E = 0\,\mathrm{keV}$ similarly as are events in α peaks distributed around the real α energy. By using the coefficients k_1, k_2, k_3 we are correcting measured α energy of every event.

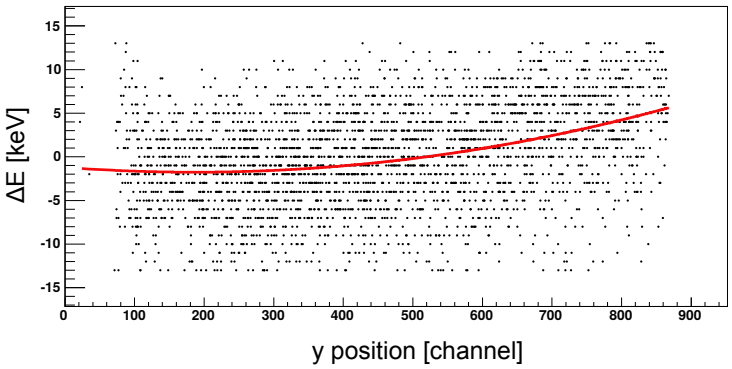

Figure 3.7: Ballistic calibration. Dependence between an energy differences of each detected event ΔE from the real energy and the vertical position in the strip y from where the signal originated fitted by a 2^{nd}-order-polynomial (red curve).

Low-energy and high-energy calibration of the STOP detector

The signals from STOP detector are processed by two electronic branches with different amplification. The low-energy electronic branch covers energies from some keV up to 16 MeV and is primarily designed for signals from α particles while high-energy electronic branch with 10 times lower amplification covers energies from 4 MeV to hundreds MeV and is designed for signals from evaporation residue implantation or spontaneous fission.

The main task of energy calibrations is to determine the relation between the amplitude of signal and corresponding energy of the particle that generated the signal. In the case of α decay of evaporation residue implanted into the STOP detector the signal is generated by the kinetic energy of α particle and a part of daughter nucleus kinetic energy. The measured energy is not corresponding to α energy E_α and neither to Q_α value. The calibration by external source would not be precise enough, but can serve as a preliminary calibration. An α source of known energies is used for this purposes. The precise calibration can be done with the use of some known activities from implanted evaporation residues or products of transfers reactions. Special targets for this purposes are usually used.

Both low and high-energy calibrations have to be done for every of the 16 strips of STOP detector separately. The energy resolution (FWHM) of well-calibrated STOP detector (all strips summed) is about 20 keV.

Low-energy and high-energy calibration of the BOX detector

The calibration is performed similarly to STOP detector. Altogether 28 detection segments need to be calibrated. For the calibration purposes α particles escaped from the STOP detector are used. The signal is generated by the rest of kinetic energy of α that left part of the energy escaping the STOP detector. The coincidental signals from STOP and BOX detectors are summed together. The relation between the amplitude of the summed signals and real energy of α particle is then determined. During the escape, α particle passes through dead layers of both STOP and BOX detectors, what is worsening the energy resolution to about 60 keV.

Position calibration between low and high electronic branch

The y position of the signal origin taken from low and high-energy branches should be the same. However a shift of positions between the two branches can be sometimes found. In order to obtain the same positions in both branches a correction to this effect needs to be applied. It is necessary when searching for the position correlations of signals (e.g. high energy signal from evaporation residue implantation and signal from its α decay). This is the right method to find the correction because both signals are expected to originate in the same position of one strip. By using implanted short-lived α decaying isotopes one can look at the position difference between signals shown by high (evaporation residue position) and low-energy (α decay position) branch for each strip.

Gamma detector calibration

The calibration of the 4 crystals of CLOVER detector is obtained using two isotopes with known energies of emitted γ rays. For this purposes sources of ^{152}Eu and ^{133}Ba are used. Together 14 γ lines are covering wide range of energies. Because of the nonlinearity of the used CLOVER detector, the calibration is done by fitting the 14 points with a polynomial of 4^{th} order. In case of significant non-linear response of the crystal we applied the separate calibration for lower (up to 600 keV) and higher (over 600 keV) energies.

3.2.3 Electronics

In the detection system of SHIP, signals with wide range of amplitudes, depending on detected particles, are registered. STOP detector itself serves as a focal plane detector, where the evaporation residues (separated from background) are implanted. Their implantation energies are typically $(10 - 50)$ MeV. Beside ER, also projectiles which passed though SHIP are implanted in STOP detector with energies $(200 - 250)$ MeV. Both STOP and BOX detectors were designed in order to detect the particles of different kind and energies originating in the radioactive decays of implanted evaporation residues. These particles are typically:

- electrons from internal conversion with energies $(0 - 1000)$ keV,
- α particles with energies of several $(4000 - 9000)$ keV,
- escaping α particles with energies of several $(1000 - 2000)$ keV,
- fission fragments with total energies of $(150 - 250)$ MeV.

The scheme of the electronics at SHIP detection setup is shown in Fig. 3.8. Due to the wide range of energies registered within the same detectors, two different electronic branches are used. Low-energy branch is suited for particle energy range of $(0 - 16000)$ keV. It is used mainly for α particles, electrons from internal conversion and also evaporation residues in cases when they have low energies. The signals from this branch are amplified by factor of about 10. High-energy branch, with no amplification, is used for fission fragments, projectiles and evaporation residues. It covers energy range from few MeV up to 300 MeV.

Low-energy branch is also used for the signals from the CLOVER detector up to 2000 keV, while the high-energy branch covers signals from gamma rays up to 8000 keV.

Signal position in the strip of the pssd STOP detector is determined via signal division to the top and bottom of the detector. A schematic view of an event registration in a strip is shown on Fig. 3.9. The event iss registered at distance of y_{TOP} from the top of detector and y_{BOT} from the bottom. The strip length is 35 mm so

$$y_{TOP} + y_{BOTTOM} = 35\,mm \tag{3.9}$$

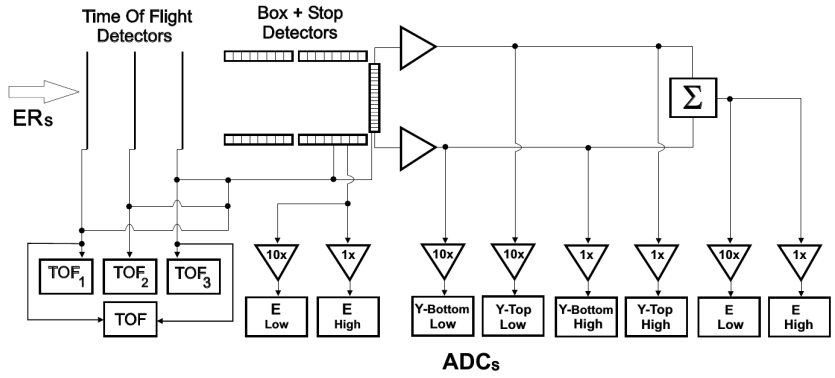

Figure 3.8: Scheme of the electronics at SHIP detection setup. Courtesy of B. Streicher [44].

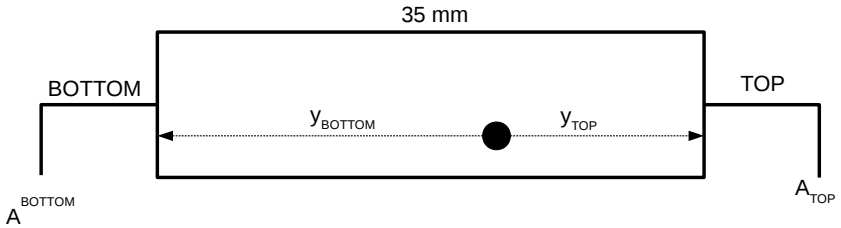

Figure 3.9: Scheme of a strip from PSSD detector. The origine of signal is indicated by black circle. Depending on the position on strip, the signal is divided towards the top and bottom of strip with amplitudes A_{TOP} and A_{BOTTOM}.

The signal is divided and a part of it is registered in the top of strip with the amplitude of A_{TOP} and second part is registered in the bottom with amplitude A_{BOTTOM}. The total amplitude A_{TOT} is determined as

$$A_{TOT} = A_{TOP} + A_{BOTTOM} \tag{3.10}$$

The distances from the top or bottom of the strips are proportional to the amplitude of corresponding signals $y_{TOP} \sim A_{TOP}$ and $y_{BOTTOM} \sim A_{BOTTOM}$ and the positions on the strip can be determined as

$$Position_{TOP} = A_{TOP}/A_{TOT},\ Position_{BOTTOM} = A_{BOTTOM}/A_{TOT} \tag{3.11}$$

3.2.4 Analysis

During the experiments at SHIP, the online analysis of the data is done with GO4 (GSI Object Oriented On-line Off-line). The off-line analysis of registered data within this work was done also with GO4. This framework was developed in GSI Darmstadt (Germany) for the purposes of measurements in low-energy nuclear physics. The analysis part itself, GO4SHIP, is a set of scripts written especially for the SHIP experiment and was implemented to GO4 for the offline analysis. This framework is widely used at SHIP experiments from a basic analysis to a complex correlation searching in the data.

3.2.5 Time and position correlations

The produced nuclei are implanted into the focal plane detector at SHIP experiment. The identification of an isotope is usually done within our experiment by the use of time and position correlation method [45]. The method is based on a search of subsequent decays originating from the place of ER implantation. The signals from the ER implantations are measured in the high-energy branch of electronic system. The implantation energies are typically few MeV and the position on a strip of implantation are usually well defined. At the same position subsequent decay/s of ER (and then decays of daughter nuclei) is/are expected according to the ER (and daughter nuclei) half-life and branching ratios. A chains of signals consisting of ER implantation and/or multiple subsequent decays are possible. The position resolution in best cases is about 0.15 mm, however, depending on the detected particles in the correlation chain, we choose different position windows. They are summarized in Table 3.1.

An example of a decay chain is shown on Fig. 3.10. In this illustrative case an ER was implanted into the focal plane detector at time t_0 and created a signal with energy E_0. The position of origin of this event is given by the strip, in which the ER of ${}^{A}Z$ was implanted and position y on this strip, which is determined from the energy signal division in the strip as was described in Sec. 3.2.3. According to the ER half-life and branching ratio, the ER undergoes decay (in this case α decay) after a time t_1, which is observed as a signal with energy E_1 in the same strip and position on the strip where the ER was implanted. The daughter nucleus after the decay, ${}^{A-4}Z-2$, may undergo another decay after time t_2, now according to the half-life and branching ratio of the daughter nucleus.

Correlation type	Typical position window
$\alpha - \alpha$	0.45 mm
ER $- \alpha$	1 mm
$\alpha -$ fission	1 mm
ER $-$ fission	1 mm
corr. with escaped α	1 mm
corr. including electron	no position window

Table 3.1: Position windows used in the correlation search. Fifth line corresponds to any correlation containing an α particle, which escaped from STOP to BOX detector. Sixth line correspond to correlations containing electrons, in this case the position window is not demanded, the only condition is that the correlation had to be found within the same strip.

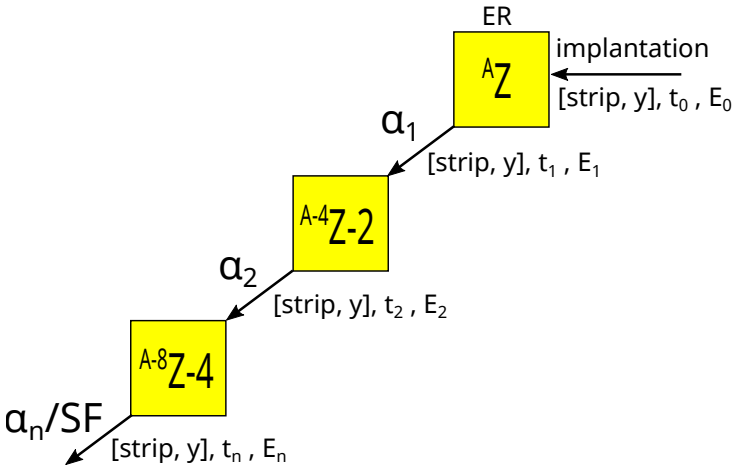

Figure 3.10: Example of a decay chain.

Such a decay chains are found in the data as a correlation between multiple signals. This method of isotopes identification, based on the assignments of radioactive decays to given isotopes is strongly selective tool. However, there are some limitation for this technique:

- In case of long-lived isotopes, rather large time windows must be set within the correlation search. For too long time windows, random correlations starts to appear.
- Depending on the detection geometry, there is always a possibility that a particle from decay escapes the focal plane detector and is detected in BOX detector or escapes the detection setup completely. In the case of fission fragments, the registered total kinetic energy is lower. For α particles, this may results in missing parts in the decay chains, which may make an assignment more difficult

In order to avoid the random correlations, various conditions are applied for decay signals:

- anti-coincidence with time-of-flight system,
- only events registered during the beam pause,
- STOP-BOX coincidences (especially in cases of fission detection),

for ERs, polygonal window in the are usually set as correlation searching conditions. Such a 2D plot of ^{216}Ac as ER produced in the reaction ^{50}Ti + ^{170}Er $\rightarrow$ ^{220}Th* is shown in Fig. 3.11. Projectiles are very well separated from the reaction product. Another issue is that besides fusion-evaporation reaction, also transfer reactions are taking place at the target. The transfer-reaction products are typically target-like (very similar mass to the target nuclei). Depending on the reaction, the transfer-reaction products form a well separated group from the fusion-evaporation-reaction products. However, in the cases, when two group are not separated, the implantation signals from transfer-reaction products may contribute to the random correlations.

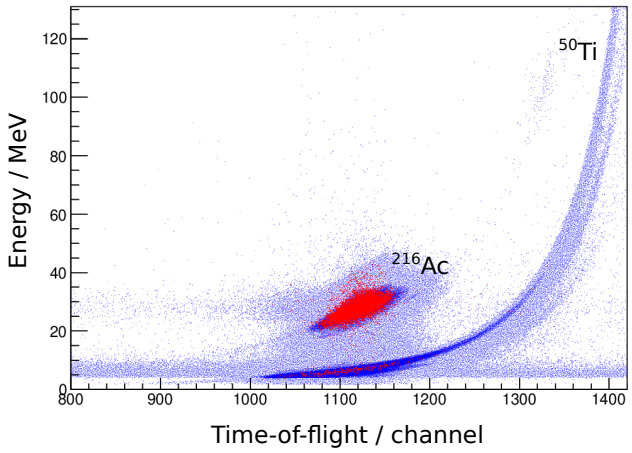

Figure 3.11: A plot of time-of-flight vs. energy of ^{216}Ac as ER produced in the reaction ^{50}Ti + ^{170}Er $\rightarrow$ ^{220}Th*. Blue: all signals registered in high-energy branch of electronics, red: signals found as ERs in the ER-α(^{216}Ac) correlation search.

Chapter 4

Experiment R292 at SHIP

4.1 Calibration reactions

4.1.1 Reaction ^{50}Ti + ^{170}Er → ^{220}Th*

The reaction of ^{50}Ti + ^{170}Er was performed for calibration purposes. The target was 350 µg/cm^2 thick and the energy of projectiles was set to 241.5 MeV. This initial energy corresponds to the beam energy of 237.9 MeV in the middle of the target and excitation energy of compound nucleus of 57.9 MeV. The advantage of this reaction is that it produces several α-decaying isotopes with separated peaks, that are useful for the energy calibration of detectors (see sections below), including ^{216}Ac with 440 ± 16 µs which can be used for fast-decay correction (discussed in Sec. 4.1.2).

Low-energy and high-energy calibrations by α lines

The energy spectrum of α decays from isotopes produced in the reaction ^{50}Ti + ^{170}Er is shown in Fig. 4.1. Many of the peaks are doublets from neighbouring isotopes with similar α-decay energies. However these energies are separated by only several keV, we decided to use for the energy calibration only single peaks, preferably from higher energy part of spectrum as it corresponds to energies expected for α decay of rutherfordium isotopes. We used namely ^{214}Ac ($E_\alpha = 7216$ keV), ^{215}Th ($E_\alpha = 7523$ keV), ^{215}Ac ($E_\alpha = 7601$ keV) and ^{216}Th ($E_\alpha = 7920$ keV).

After the balistic calibration (discussed in Sec. 3.2.2) and low-energy calibration, α-decay peaks have typically FWHM $\approx$ 20 keV. As an example we randomly chose three strips and compared peaks at the same energy

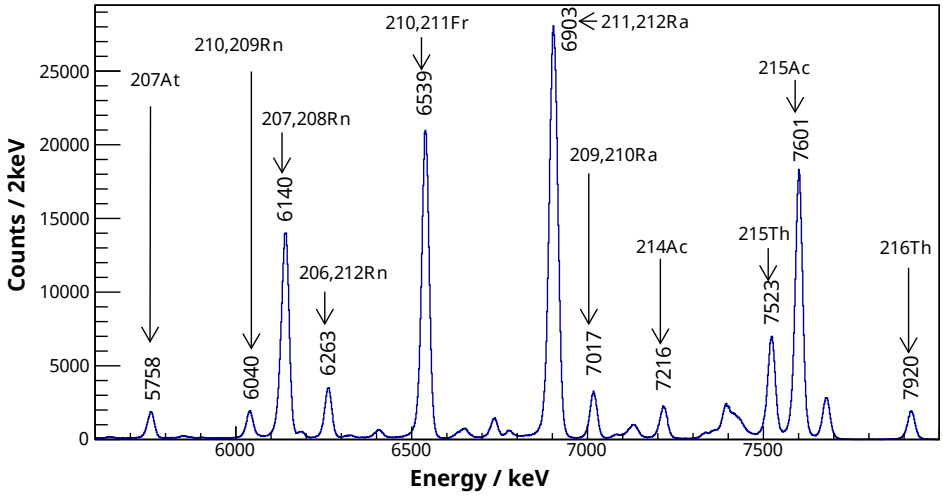

Figure 4.1: Low-energy spectrum containing α lines from the decays of ERs produced in reaction ^{50}Ti + ^{170}Er $\rightarrow$ ^{220}Th*.

(E_α = 7920 keV of ^{216}Th) for each of three strips and also compared to the peak containing events from all strips. This comparison is shown on Fig. 4.2. We observed that the strips are calibrated precisely within $\approx$ 1 keV and FWHM of peak from all strips is very similar to peaks from single strips.

The calibration of high-energy electronic branch was done in a similar way than low-energy calibration mentioned above. A comparison of the same energy spectrum registered by low- and hig-energy electronic branch is shown in Fig. 4.3. It is clear that the energy resolution in the case of high-energy branch is significantly worse due to the lower number of channels defining the peak (covered range of energies is wider, mentioned in Sec. 3.2.3). This branch was not suited for detection of α particles, but rather higher-energy signals such as ERs, projectiles or fission fragments. The reason for calibration by α decay energies is that the calibrations should be mainly suited for the detection of fission-fragments energy (energies of ERs and projectiles were not the focus of our measurement) and there simply are not any possibilities to calibrate via high-energy fission-fragment signals from implanted activity. In addition, high-energy signals are affected by pulse-height defect, which has a non-linear behavior and also depends on the implantation depth. The issue of high-energy calibration for used Si detectors is rather complex and a separate section (Sec. 4.1.4) is dedicated to this topic.

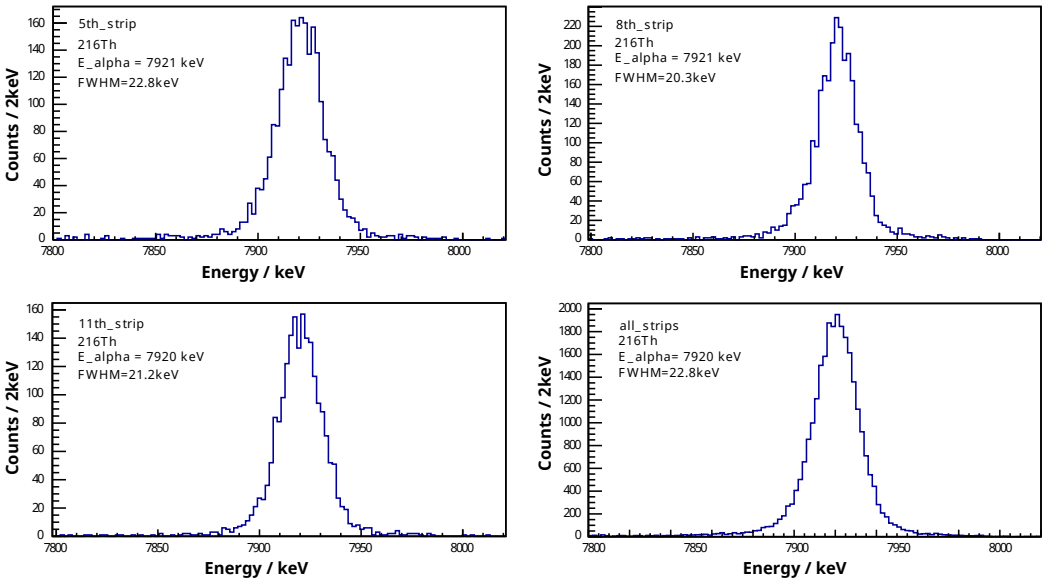

Figure 4.2: Comparison of peak positions and FWHM of α line from ^{216}Th registered in three randomly chosen strips and summed spectrum of all strips.

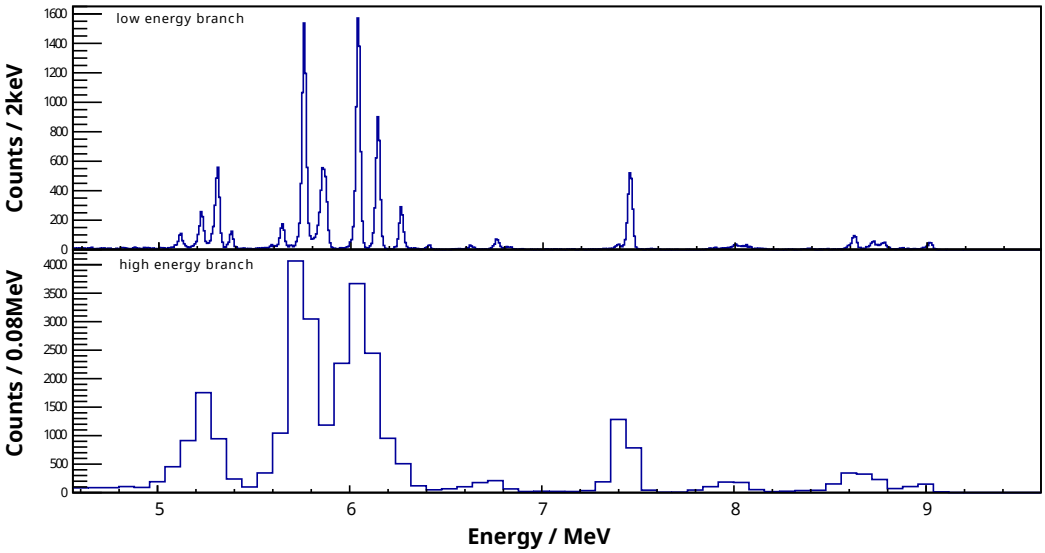

Figure 4.3: Comparison of the calibrated low-energy spectra registered in low-energy and high-energy electronic branches.

4.1.2 Correction of the fast-decay energies

For fast decays in our STOP detector (up to 500 µs) the signal from decay [e.g. α decay or internal conversion electrons (CE)] is summed with the tail of ER signal. This pile-up effect causes a deviation of measured decay energy and depends on the time difference between the decay and the ER implantation. For studies of electron energies in our work, discussed further in Sec. 5.2.1, it was necessary to determine an energy correction. We estimated this effect using the α decay of ^{216}Ac collected during the calibration measurement with reaction ^{50}Ti + ^{170}Er, which delivers a clearly separated peak at 9118 keV in the α spectrum and has a half-life of 440 ± 16 µs. The plot of α-particle energy as a function of the time difference between the implantation and decay is shown on the top of Fig. 4.4. A clear dependence can be seen, influencing the energies of decays that occurred faster than 500 µs after the implantation of ER. After this time the energies saturate to the real value and the effect vanishes. We used the difference ΔE in measured and expected energies (green and red lines resp. in Fig. 4.4) at given time as an energy correction as:

$$\Delta E = (9118 - \overline{TKE}_{fit})\,\mathrm{keV} \tag{4.1}$$

The same events from ER–α correlations of ^{216}Ac with applied energy correction is shown in Fig. 4.4b). As this effect depends on the high-energy signal from the implantation of ER, it can be used as a correction for correlations of other type, such as ER–CE with an implantation of ER and conversion electron in case that the energy of ER is similar to the one of ^{216}Ac from our correction method. We used this correction method in our further analysis of electron energies in Sec. 5.2.1 and Sec. 5.2.2.

4.1.3 Reaction ^{48}Ca + ^{206}Pb → ^{254}No* → ^{252}No + 2n

The reaction of ^{48}Ti + ^{206}Pb was performed for the purposes of production ^{252}No, which is one of few isotopes from transfermium region for which a SF activity of implanted nuclei with known $\overline{TKE}$ can be studied. The target of ^{206}Pb was 450 µg/cm^2 thick, projectiles were accelerated to 221 MeV, which corresponds to 218 MeV in the middle of the target and excitation energy of compound nucleus of 24 MeV. After the separation, before implanting into the STOP detector, the energy of ERs was then lowered to several different energies using degrader Mylar foils, so that different implantation depths

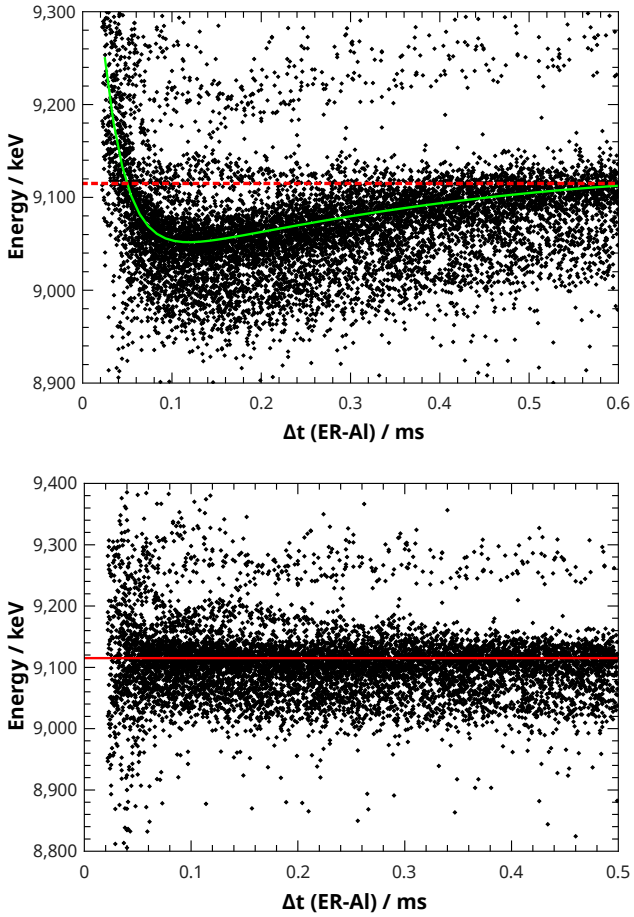

Figure 4.4: Top: Measured energy of the ^{216}Ac α decay as function of the time after implantation of the ER. For fast decays, the signal from α decay is summed with the tail of ER signal. The correction is given as a difference between the fit of measured energies (green solid line) and expected energy (red dashed line) at given time. Bottom: The same data as in top panel, but with applied correction.

could be achieved for the studies of pulse-height defect discussed in following section.

4.1.4 Correction to energy deficit in measured TKE

The crucial task for the evaluation of $\overline{TKE}$ using silicon detectors is the correction of the deficit in the measured energies for fission fragments. There are two main effects influencing the TKE measurements, already discussed in previous studies performed at SHIP [46, 43]. First, the pulse-height defect (see e.g. [47]) due to non-ionizing interactions with atoms in the detector and recombination of electron-hole pairs. The pulse-height defect is negligible for light ions such as α particles but becomes very important for heavy ions such as fission fragments (more than 10%). The energy calibration of the silicon STOP and BOX detectors was based on α-decay energies (which do not suffer by pulse-height defect) of implanted nuclei and therefore one has to correct the obtained values of fission-fragment TKE for the pulse-height defect.

The second effect is the strong dependence of the energy deficit on the implantation depth into the STOP detector. The importance of both effects is illustrated in Fig. 4.5, where α-particle energies of ^{252}No and its daughter products ^{248}Fm and ^{244}Cf are compared for various implantation depths from practically 0 µm to 5.7 µm. There is no observable shift of α decay peaks in function of implantation depth of ERs and the measured peak positions correspond to the known values of α-particle energies for these isotopes. In the case of registered TKE of fission fragment from the SF of ^{252}No (Fig. 4.6), a clear dependence on implantation depth can be seen. In addition, the TKE distribution position does not correspond to the known value of 194.3 MeV even for high implantation depths The implantation depth of ERs is usually few µm. The typical range of fission fragments in the silicon material is $(10 - 20)$ µm, giving the opportunity for one fragment to escape. In the case of STOP-BOX anticoincidences with one fragment escaping, the fission energy cannot be fully reconstructed. The presence of these events in the spectrum results in a low-energy tail. In the cases when fragments escape (for both STOP-BOX coincidences and anticoincidences), they are passing through the dead layers of STOP and possibly BOX detector under various angles, which also contributes to the energy deficit.

In order to evaluate the energy deficit, we used ^{252}No for which the value of $\overline{TKE} = 194.3$ MeV is well known from previous studies [5]. We measured

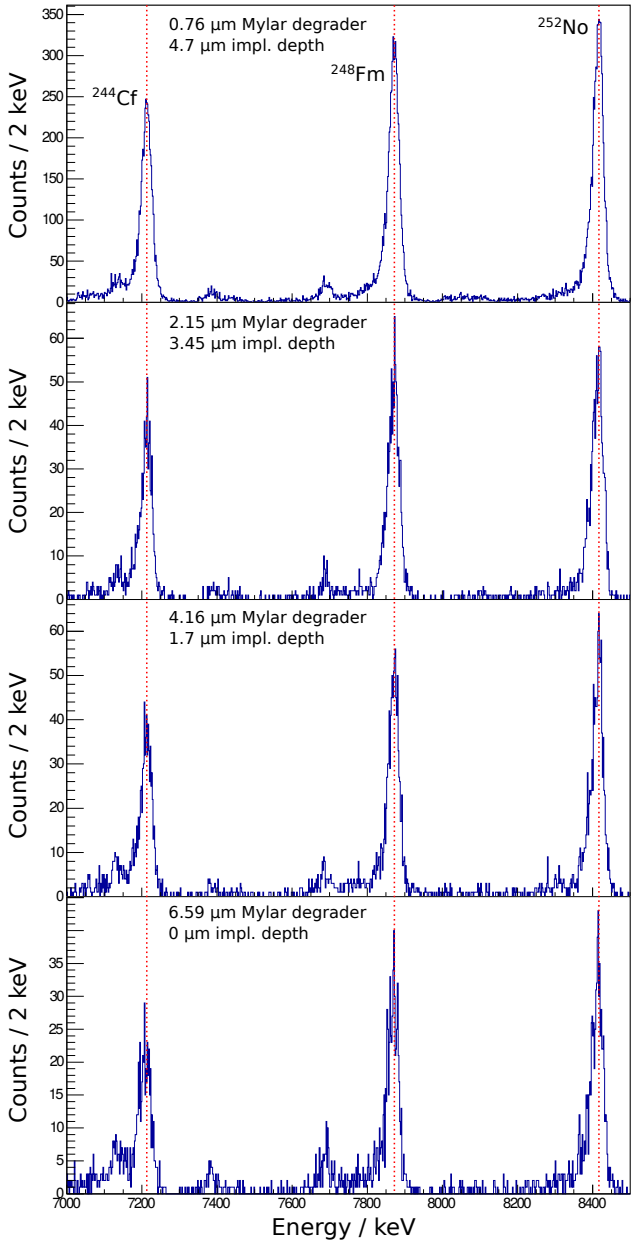

Figure 4.5: Comparison of energies of α lines from ^{252}No and its daughter products ^{248}Fm and ^{244}Cf in dependence with an implantation depth. The position of peaks is not effected by the pulse-height defect.

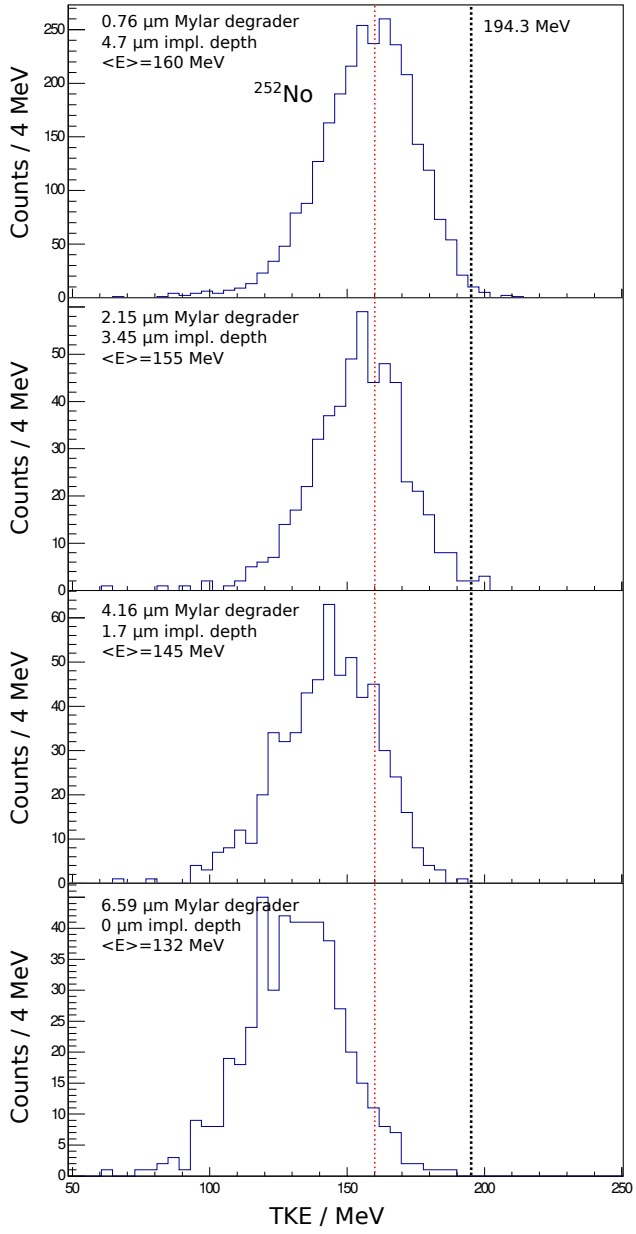

Figure 4.6: Comparison of total kinetic energies from the SF of ^{252}No in dependence with an implantation depth. The position of peaks is significantly effected by the pulse-height defect.

Degrader foil thickness [µm]	TOF C foils [pcs]	SRIM energy [MeV]	SRIM impl. depth [µm]	LISE++ energy [MeV]	LISE++ impl. depth [µm]
0	4	32.9	5.69	31.8	5.67
0	6	30.8	5.37	29.5	5.31
0.72	6	26.7	4.68	25.5	4.69
2.15	6	18.6	3.31	18.0	3.45
4.16	6	10.3	2.01	8.5	1.7
6.59	6	1.1	0.2	0	0

Table 4.1: Kinetic energies and implantation depths of ^{252}No, calculated by SRIM [48] and LISE++ [49]. In the table columns, from left to right, thickness of degrader foils, number of time-of-flight foils, entering energies and implantation depths calculated by SRIM and LISE++ are shown.

the $\overline{TKE}$ of ^{252}No at six different implantation depths. The analysis for STOP-BOX coincidences was published previously [46], where the implantation depths were calculated by SRIM [48] and a linear fit was used for $\overline{TKE}$,/ implantation depth dependence. However, SRIM is able to calculate the energy losses and ranges only for isotopes up to uranium ($Z = 92$) and for heavier isotopes an extrapolation is necessary. Therefore we decided to use LISE++ [49] in this work, due to its possibility to calculate the implantation depth directly for heavier nuclei. The cross-check was done by SRIM. In addition to previous works, we also evaluated the correction for STOP-BOX anticoincidences. The study was published in [50].

Considering the middle of the target as a place for compound nucleus synthesis, we calculated energy losses of ^{48}Ca projectiles in the first half of target material (40 µg/cm^2 of C and 225 µg/cm of ^{206}PbS) and energy losses of created evaporation residues of ^{252}No passing through the second half of the target (225 µg/cm^2 of ^{206}PbS material and 10 µg/cm^2 of carbon), charge equilibration foil (30 µg/cm^2 of carbon) and 2 or 3 pairs of time-of-flight detector foils (each foil consists of 30 µg/cm^2 of carbon). Mylar degrader foils were placed just before the detection setup to achieve various implantation depths. The results of kinetic energies before entering the detector and implantation depths of ^{252}No are shown in Table 4.1. It should be noted that when evaporation residues are entering the silicon STOP detector, they pass

through a $10\,\mu g/cm^2$ thick dead layer, where they lose about $(0.21-0.28)$ MeV (calculated by LISE++ for $(1-30)$ MeV evaporation residues of ^{252}No).

The analysis was done separately for the STOP-BOX anticoincident and coincident events. The results for STOP-BOX anticoincidences, shown in Fig. 4.7a), exhibit a strong non-linear $\overline{TKE}$ dependence on the implantation depth. For higher implantation depths the energy deficit decreases.

At implantations deeper than the range of a fission fragment the energy deficit reaches its minimum and is constant, however such a deep implantation is not possible in our experiment - the energy of ERs is defined from the reaction kinematics, where the only variable input is the beam energy, which is however set to the maximum of reaction cross-section. The measured $\overline{TKE}$ thus should saturate to a constant maximal value and so we fitted the obtained experimental points by a saturation-growth function.

In the case of STOP-BOX coincidences, signals from both detectors were summed up to evaluate the TKE of fission event. The results are shown in Fig. 4.7b). The energy deficit also decreases with higher implantation depths and we again applied the fit by a saturation-growth function. The advantage of this approach is that we measure the energy of both fully detected fragments, however only at the cost of lower statistics of about 20% of all fission events.

For both, STOP-BOX coincidences and anticoincidences, the energy deficit at given implantation depth can be determined as an energy difference of the known $\overline{TKE}$ of 194.3 MeV and the value from experimental fit (Fig. 4.7) as

$$\Delta E = (194.3 - \overline{TKE}_{fit})\,\mathrm{MeV} \tag{4.2}$$

The pulse-height defect in Si is dependent on the particle characteristics (Z, A) and particle energy. In our analysis we assumed that the correction to the pulse-height defect determined for ^{252}No can also works for our studied isotopes ^{255}Rf, ^{256}Rf and ^{258}Rf. We based this statement of the fact that Z and A of ^{252}No and the three Rf isotopes are similar and also expected <TKE> of Rf isotopes are similar to <TKE> of ^{252}No. Typical implantation depths of Rf isotopes were calculated by LISE++ to be $(6.3-6.5)\,\mu m$ while in the case of studied ^{252}No it was possible to reach maximal implantation depth of $\approx 5.7\mu m$. Thus in order to estimate the energy deficit at higher implantation depths the linear extrapolation from the data was done.

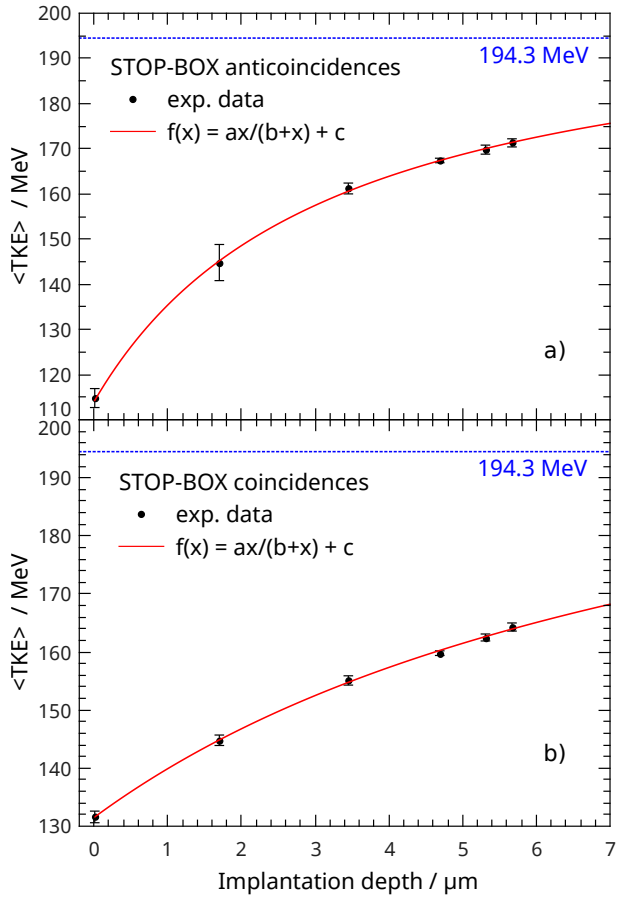

Figure 4.7: $\overline{TKE}$ from the SF of ^{252}No as a function of implantation depth of evaporation residues in the detector for: a) STOP-BOX anticoincident SF events, b) STOP-BOX coincident SF events. Blue dashed line: $\overline{TKE} = 194.3$ MeV of ^{252}No from [5]. Red solid line: saturation-growth fit of experimental data.

Remark on LISE++ and SRIM calculations of energy losses for heavy ions

The implantation depths for ^{252}No calculated by SRIM and LISE++ in Table 4.1 are in a good agreement, even though the results from SRIM were obtained by the extrapolation of values for ^{238}U with the same kinetic energy to mass ratio of ^{252}No evaporation residues. On the other hand, we found some evident disagreements in directly (without extrapolation) calculated implantation depths for lighter nuclei. As an example, we did calculations of ranges for 40 MeV ^{238}U and ^{208}Pb in silicon. The results for ^{238}U are 6.83 µm and 6.77 µm for SRIM and LISE++. For the lighter nucleus ^{208}Pb, the difference in the calculated implantation depths becomes more significant, the values are 7.15 µm and 5.95 µm, respectively.

4.2 Production and identification of $^{255,\ 256,\ 258}$Rf isotopes

Experiments aimed at the production of rutherfordium and dubnium ($Z = 105$) isotopes and investigations of their decay properties were carried out at GSI Darmstadt (Germany) using the velocity filter SHIP [51]. The beam of ^{50}Ti ions was accelerated by the UNILAC to energies from 225 to 243 MeV. The isotopes$^{255,\ 256\ ,258}$Rf were produced in the fusion-evaporation reactions ^{50}Ti + $^{207,\ 208}$Pb and ^{50}Ti + ^{209}Bi. Targets of ^{207}PbS, ^{208}PbS and $^{209}Bi_2O_3$ with thicknesses of 450 µg/cm^2, 450 µg/cm^2 and 463 µg/cm^2, respectively, were used. The evaporation residues ^{255}Rf and ^{256}Rf were produced in the $2n$ evaporation channel from the compound nuclei while the ^{258}Rf was produced indirectly through the electron capture (EC) decay of ^{258}Db [52].

4.2.1 Some remarks on the identification of SF events

It has to be mentioned that the identification of SF events is done on the high background of high-energy events originating mostly in scattered projectiles. We demonstrate the selection criteria we use for the SF identification on an example of ^{258}Rf produced during the irradiation ^{50}Ti + ^{209}Bi. The high-energy spectrum of all events registered in STOP detector is shown on Fig. 4.8a)-left. A SF activity of ^{258}Rf was produced by EC decay of ^{258}Db is expected, however only a peak of non-scattered projectiles that passed through the separator is visible. The background in lower energies is due

to scattered projectiles. A condition of anti-coincidence with TOF system (Fig. 4.8b)-left) is able to significantly suppress this background with respect to the TOF efficiency. This condition rejects most of the events originating from the separator and a peak of fragments TKE is visible (still) on a background. Every SF is accompanied by a emission of several γ rays which is a reliable marker for SF event. Applying additional condition of coincidence of high-energy signal with a signal from CLOVER detector is shown on Fig. 4.8c)-left. The spectrum is clearer but there is a background left. Another possibility resulting from the pulsing character of accelerator is to accept only events that were register during the beam-off period (in beam pause). Such a condition leaves almost clear TKE spectrum of SF event (Fig. 4.8d)-left), however a small low-energy tail is still present. As a further possible condition for SF event identification we chose time and position correlation search (discussed in Sec. 3.2.5) between conversion electrons from EC decay of ^{258}Db and subsequent SF of ^{258}Rf. The result of SF events extraction from the background for the correlation method is on Fig. 4.8e)-left. Thus in the case of SF events registered in the STOP detector (with no BOX detector coincidence) the method of accepting events only during the beam pause and the correlation method are the only two useful, however, the first one only in case of not so high background.

The same conditions for SF events with an additional condition for a coincidence with BOX detector is shown on Fig. 4.8a–e)-right. It is clear that the condition of STOP-BOX coincidences a strongly itself (Fig. 4.8a). With the condition of TOF-anticoincidences the high-energy spectrum is cleared from background and contains SF events. However in some cases, it is better to add a condition of coincidences with CLOVER detector which is strongly selective but not so crucial for the statistics of SF events. The conditions of beam pause and correlation methods are not effectively suppressing the background anymore but rather dramatically lowering the statistics. Thus in the case of STOP-BOX coincidences we are avoiding them if possible. It is important to emphasize here, that for the half-life determination, the correlation method is the only one possible.

Another issue in the process of SF identification is the separation of more SF activities present in the data. As the $\overline{TKE}$ of possibly produced fissioning isotopes is typically $\approx 200\,\mathrm{MeV}$ and the $FWHM$ of the TKE distribution is $\approx 30\,\mathrm{MeV}$, it is possible to separate the activities only based on their different half-lives. Such a separation will be discussed in Sec. 4.2.4.

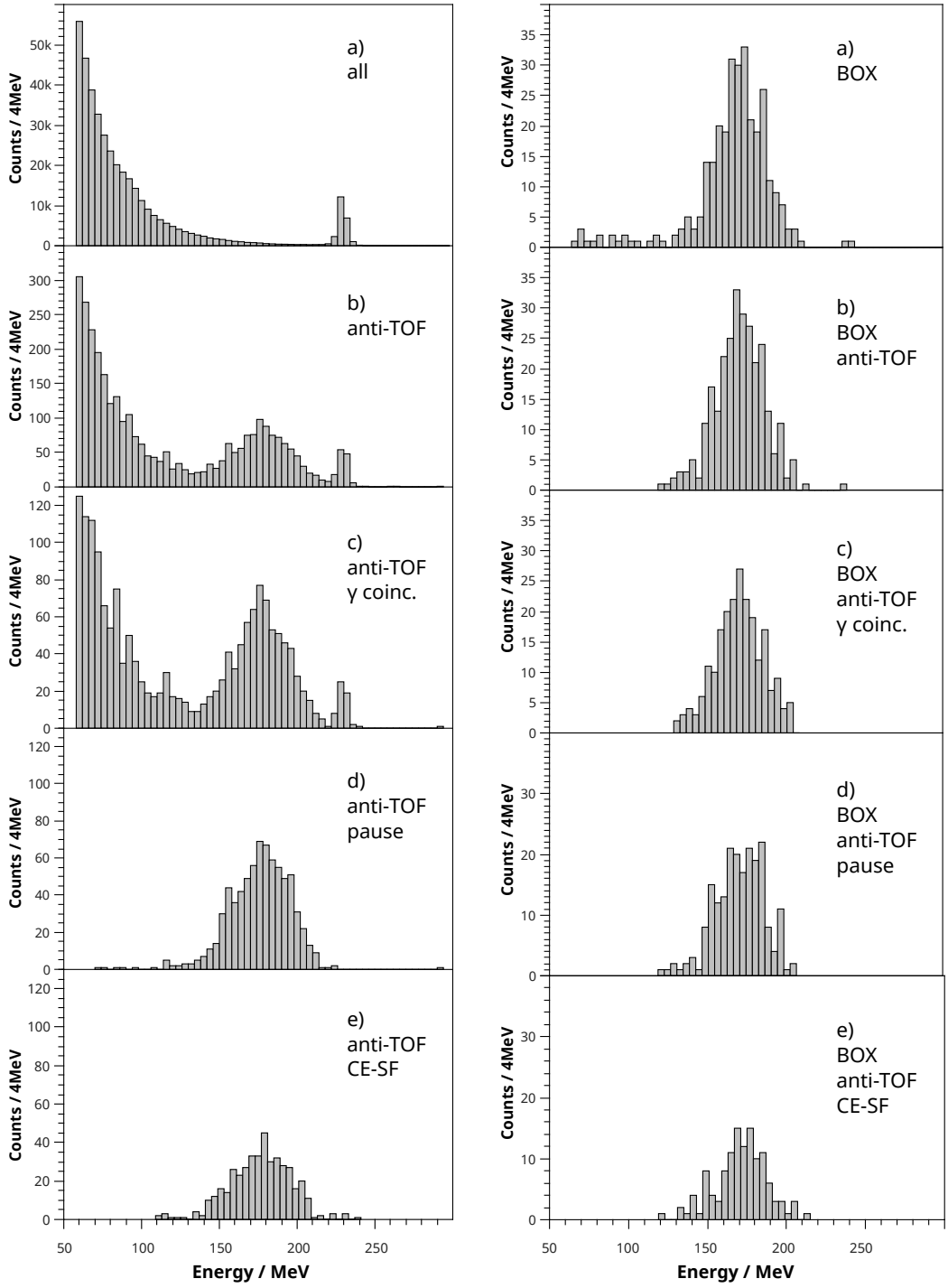

Figure 4.8: Selection criteria for the identification of SF events from the high-energy signals. Example of such selection is shown for ^{258}Rf. Right: for STOP-BOX anticoincidences, left: for STOP-BOX coincidences

Fusion-evaporation reaction	E_{beam} [MeV]	E_{targ} [MeV]	E^*_{CN} [MeV]	Time [Hours]	σ [nb]
^{207}Pb(^{50}Ti, 2n)^{255}Rf	243	239.8	23.4	33.4	11.4 (18)
^{208}Pb(^{50}Ti, 2n)^{256}Rf	233	229.8	15.8	17.2	2.4 (3)
	241.5	238.3	22.6	8.1	15.5 (17)
^{209}Bi(^{50}Ti, 1n)^{258}Db $\xrightarrow{EC}$ ^{258}Rf	236	232.6	16.0	195.6	2.9 (9)

Table 4.2: Summary of the individual irradiations during R292 at SHIP. From left to right, reaction is noted, E_{beam} is the beam energy before enetring the target, E_{targ} is the beam energy in the middle of target, $E*_{CN}$ is excitation energy of compound nucleus, then absolute time of measurements and calculated cross-sections are stated.

4.2.2 Irradiations

We performed three irradiations with ^{50}Ti beam and ^{207}Pb, ^{208}Pb and ^{209}Bi. The details of irradiations are summarized in Table 4.2.

We registered several hundreds of SF events in each of the irradiations. In order to identify the SF events of ^{255}Rf and ^{256}Rf isotopes, we used time and position-correlation method based on delayed coincidences between the ER implantation and subsequent high-energy signal (corresponding to SF) in the same position of the detector. In the case of ^{258}Rf we searched for correlations between conversion electrons after β decay of ^{258}Db produced in the reaction $^{50}\mathrm{Ti} + {}^{209}\mathrm{Bi}$ and subsequent SF decay of the daughter nucleus ^{258}Rf. The searching time windows between either ER-SF or CE-SF were set to ≈ 5 time the half-life for each isotope. For the SF events, the energy condition for high-energy signals was set to 100–300 MeV. Searching methods and conditions as well as the statistics of detected SF events for each isotope are described in Sec. 4.2.3, 4.2.4, and 4.2.5 and summarized in Table 4.3. The time conditions are also demonstrated on Fig.4.9.

Low-energy spectra

The production of isotopes was also monitored by α decay. Figure 4.10 shows low-energy spectra for each of the irradiations. The dominant α-decay peaks in each spectrum originate in target-like isotopes, we observe *alpha* lines of

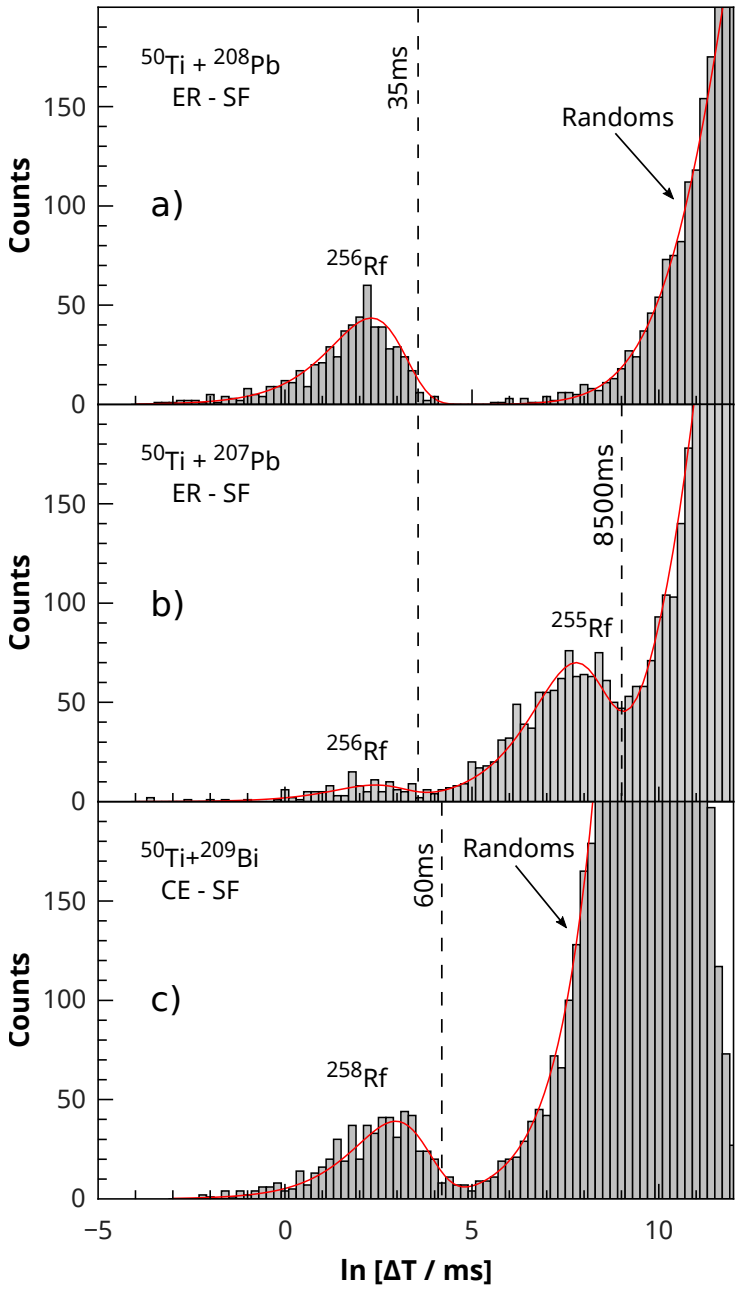

Figure 4.9: Time-difference distributions obtained from the: a) ER-SF correlation search in the data from reaction ^{50}Ti + ^{208}Pb, b) ER-SF correlation search in the data from reaction ^{50}Ti + ^{207}Pb, c) in CE-SF correlation search in the data from reaction ^{50}Ti + ^{209}Bi. The dashed vertical lines represents the limits that were set for time-difference windows used to separate the isotopes: a) 0–35 ms for ^{256}Rf, b) 35–8500 ms for ^{255}Rf, c) 0–60 ms for ^{258}Rf. Red solid line represent the fit of the data with function from the maximum likelihood method discussed in [53].

Isotope	Event	Condition	$N_{(S-B)coinc}$	$N_{(S-B)anticoinc}$
^{255}Rf	ER-SF	$\Delta T = (35 - 8500)$ ms	160	715
^{256}Rf	ER-SF	$\Delta T = (0 - 35)$ ms	138	453
^{258}Rf	SF	γ coinc.,	220	-[1]
^{258}Rf	CE-SF	$\Delta T = (0 - 60)$ ms	118	412

Table 4.3: Statistics of SF events for each isotope from STOP-BOX coincident (column IV) and anticoincident events (coulmn V). The searching time windows between either ER-SF or CE-SF are stated in column III. For the SF events, the energy condition for high-energy signals was set to 100–300 MeV.

several polonium (Po), astatine (At) and radon (Rn) isotopes, depending on the target and beam energy. These isotopes are typically produced via transfer reactions along with the products of fusion-evaporation reactions. The α-particle energies of transfer-reaction products in this case in in the range 5000–7500 keV. However, for our purposes, the interesting part of these spectra is in the range of higher α-decay energies where we expect the α-decay peaks from the rutherfordium (Rf) and dubnium (Db) isotopes and their decay products - isotopes of lawrencium (Lr), nobelium (No) or fermium (Fm).

4.2.3 ^{256}Rf produced in reaction ^{50}Ti + ^{208}Pb

The reaction ^{50}Ti + ^{208}Pb with the projectile energy set to 241.5 MeV (compound nucleus excitation energy of 22.6 MeV) was suited for the ^{256}Rf production through the $2n$ evaporation channel from the compound nucleus ^{258}Rf. For a part of the experiment the projectile energy was lowered to 233 MeV (compound nucleus excitation energy 15.8 MeV) to produce ^{257}Rf by $1n$ evaporation channel. The difference in produced isotopes with the change of beam energy can be demonstrated on low-energy spectra from of α decays in Fig. 4.10a) and Fig. 4.10b). Except the dramatic change in produced transfer products, where radon and astatine isotopes are dominantly produced at higher beam energy, while polonium isotopes at lower-energies, there is also a clear change in ^{257}Rf production (shown in insets of Fig. 4.10a) and Fig. 4.10b)). The production of ^{256}Rf cannot be monitored via the α-decay spectra due to the low branching ratio for α decay. The problematics of ^{256}R α decay is discussed in appendix

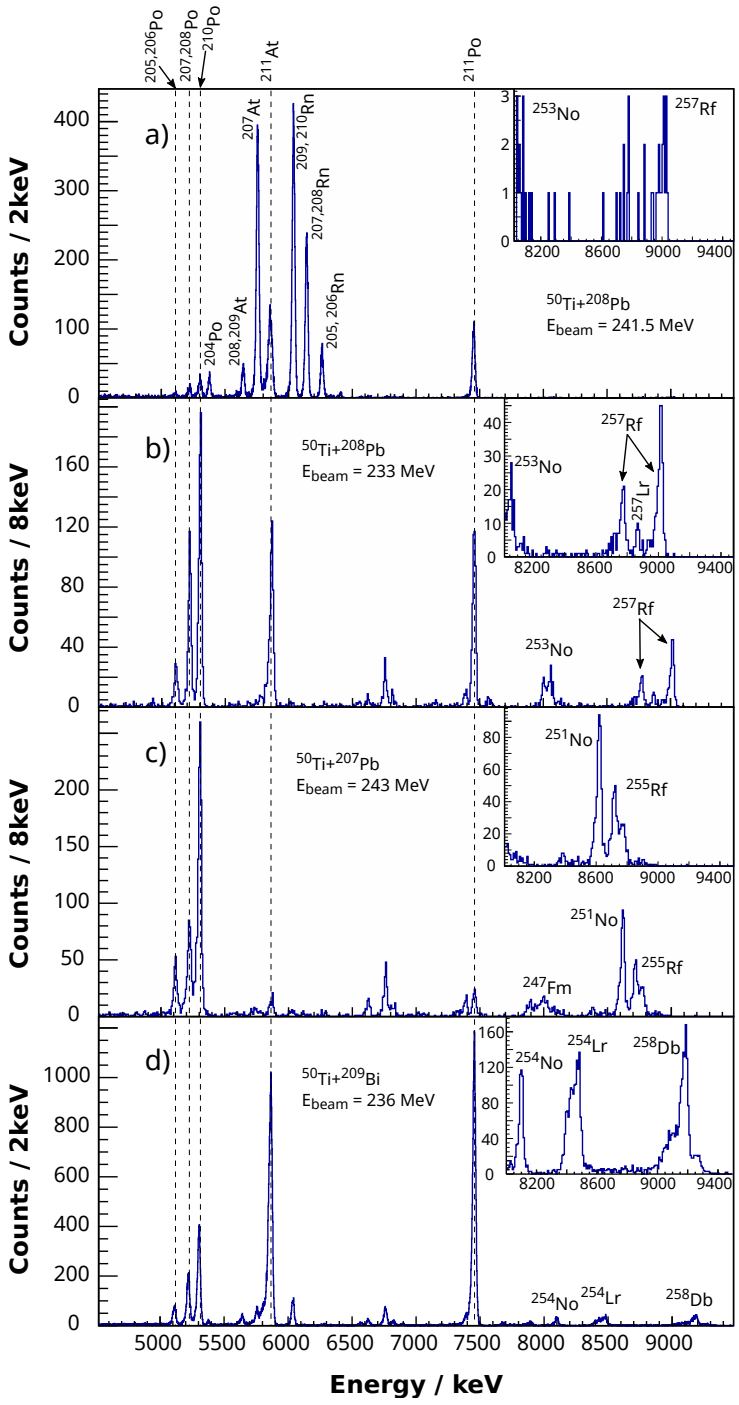

Figure 4.10: Low energy spectra obtained during the beam pause in irradiations: a) ^{50}Ti + ^{208}Pb with the beam energy of 241.5 MeV, b) ^{50}Ti + ^{208}Pb with the beam energy of 233 MeV, c) ^{50}Ti + ^{207}Pb with the beam energy of 243 MeV, d) ^{50}Ti + ^{209}Bi with the beam energy of 236 MeV.

In order to detect the SF events, we searched for ER-SF correlations. Time-difference distribution of detected ER-SF events from this reaction is shown in Fig. 4.9a). A time distribution corresponding to the half-life of ^{256}Rf ($T_{1/2} = 6.67$ ms [12]) was formed, well-separated from the distribution of random correlations without any different visible SF activity.

Together, we registered 591 SF events that were preceded by the implantation of ERs with time differences less than 35 ms. In 138 cases they were in coincidence with BOX detector and the energy signal was reconstructed as a sum of signals from STOP and BOX detectors.

We excluded the contribution of ^{255}Rf at mentioned excitation energies of compound nuclei - the number of ^{255}Rf fission events should be comparable to the α decays due to their similar branching values ($b_{SF} = 0.52 \pm 0.06$, $b_\alpha = 0.48 \pm 0.06$ [54]) and we did not observe any $\alpha(^{255}\text{Rf})$-$\alpha(^{251}\text{No})$ correlations ($b_\alpha(^{251}No) \approx 91\%$).

We also found about 700 ER-$\alpha(^{257}\text{Rf})$ correlations, mainly at the beam energy 230 MeV. With respect to the branching ratio of 0.013 [55] for SF of ^{257}Rf and a half-life of 4.8 ± 0.2 s [56] the number of expected SF events for ^{257}Rf is close to zero and thus negligible within $\Delta t = 35$ ms after the implantation of ERs.

We assigned all SF events detected during this reaction to ^{256}Rf. From the STOP-BOX coincident events, we evaluated a half-life as 6.75 ± 0.49 ms [see inset in Fig. 5.2b)], which is in agreement with the half-life reported in [12].

4.2.4 ^{255}Rf produced in reaction ^{50}Ti + ^{207}Pb

The next case was the study of ^{255}Rf produced in the reaction ^{50}Ti + ^{207}Pb via $2n$ evaporation channel from the compound nucleus ^{257}Rf. For this purpose, the beam energy was set to 243 MeV which corresponds to the compound nucleus excitation energy of 23.4 MeV.

Similarly to reaction ^{50}Ti + ^{208}Pb, discussed in previous section, we also searched for ER-SF correlations. Time-difference distribution of detected ER-SF events is shown in Fig. 4.9b). A groups of events corresponding to SF activities of ^{256}Rf and ^{255}Rf were observed. For the identification of SF from ^{255}Rf we accepted only events with time differences between the ER and SF signals of 35–8500 ms. With regard to the time distribution for ^{256}Rf obtained in reaction ^{50}Ti + ^{208}Pb [see Fig. 4.9a)], the minimum time difference between ER and SF signals was set to 35 ms in order to avoid

a contamination from ^{256}Rf (due to the $1n$ evaporation channel of ^{50}Ti + ^{207}Pb reaction and possible ^{208}Pb impurities in the ^{207}Pb target resulting in $2n$ evaporation channel of ^{50}Ti + ^{208}Pb reaction). The upper limit for the time window was set to 8500 ms, which is $\approx$ 5 times the half-life of ^{255}Rf (1.68 ± 0.09 reported in [57]).

In total, we identified 875 SF events corresponding to ^{255}Rf, 160 of them were in coincidence with BOX detector. In about 20% of cases, we found two possible ER candidates (ER_1 and ER_2) for one SF event within 35–8500 ms due to the fact, that the end of searching time window was already in the region of random correlations [see Fig. 4.9b)]. Although, this situation results in the background for time-difference distributions (both ER_1 and ER_2 are included), it does not effect the TKE distributions of SF events (SF event is included only once). If ER_1 was in the range 0–35 ms before the SF event and ER_2 in 35–8500 ms, the assignment to ^{255}Rf or ^{256}Rf was questionable and we excluded such SF events from further TKE studies.

Among the events found within 35–8500 ms, we estimated the contribution of only 3 SF events that may originate in ^{256}Rf from the half-life and the number of SF events in the range 0–35 ms. As there is not any possibility for other SF activity, we assigned all the events found within 35–8500 ms to ^{255}Rf and used these in further TKE studies. From the STOP-BOX coincident events, we evaluated the half-life of 1.60 ± 0.07 s [see inset in Fig. 5.2a)], which agrees with the half-life reported in [57].

4.2.5 ^{258}Rf produced via EC decay of ^{258}Db

The reaction ^{50}Ti + ^{209}Bi with the projectile energy set to 236 MeV (E^*_{CN} = 16.0 MeV) was suited for the ^{258}Db production through the $1n$ evaporation channel. A considerable amount of ^{258}Rf was produced by EC decay of ^{258}Db ($b_{EC} = 0.23 \pm 0.08$ and $T_{1/2} = 4.3 \pm 0.5$ s reported in [10]). The investigations of the EC process in ^{258}Db and also α-decay studies of ^{258}Rf as well as the problematics of ^{258}Rf SF identification in this case were reported in [52, 58]. We searched for correlations between CE from the deexcitation of states in ^{258}Rf populated after the EC decay of ^{258}Db and subsequent SF. Time-difference distribution of detected CE-SF events is shown in Fig. 4.9c).

We identified 530 SF events within a time window of 0–60 ms ($\approx$ 5 times the half-life of ^{258}Rf) between CE and SF. In 118 cases, signals were in coincidence with BOX detector. We assigned all events to ^{258}Rf. We used CE-SF(STOP-BOX) time differences to determine the half-life of 8.79 ± 1.12 ms

[see inset in Fig. 5.2c)], which is in agreement with the values reported in [52].

However, we estimated that the detection efficiency for electrons was less than 50%. Thus for further studies of STOP-BOX coincident events, we decided to take all high-energy events in coincidence with a signal from Clover detector (no correlation with CE) in order to increase the statistics in TKE distribution. The high-energy background mainly comes from scattered projectiles that passed through the separator. The probability of STOP-BOX coincidence in the case of projectiles is very low, only due to the random coincidences and also projectiles are not accompanied by γ rays as it is in the case of SF events. Thus the criteria of STOP-BOX-CLOVER coincidence is strongly selective for SF detection [43]. We found 220 of these events, which almost doubled the statistics in comparison with CE-SF correlations. Since there is not any possible contribution from other SF activity we assigned all events to ^{258}Rf.

In the case of STOP-BOX anticoincident SF events, we still required correlations with CEs, since the criteria of STOP-CLOVER (STOP detector signal coincident with signal from Clover detector) is not as selective as STOP-BOX-CLOVER, leaving considerable amount of high-energy background events.

Chapter 5

Discussion of results

5.1 TKE evaluation for SF of ^{255}Rf, ^{256}Rf and ^{258}Rf

5.1.1 Corrected mean TKE

As was mentioned in Sec. 4.2 the spectra from STOP-BOX anticoincidences contain two types of evets: a part where both fragments remained in the STOP detector and a small part where one of the fragments escaped the detection setup completely. The later ones have incomplete energy and affect the shape of TKE distribution (see discussion in [43]). These distributions are therefore not suitable for the analysis of their shape as would be desirable for the search of bimodal fission, however they could still be scaled to allow us an evaluation of $\overline{TKE}$. The values of $\overline{TKE}$ obtained from all SF events (described in Fig. 3.6) for each isotope are summarized in Table. 5.1 and compared to results from previous studies. The $\overline{TKE}$ of ^{255}Rf isotope is 199.5 ± 2.7 MeV, which is in a good agreement with the value of 199 ± 3 MeV from [6], where ^{255}Rf was produced at SHIP indirectly by α decay of ^{259}Sg and the method from [46] was used to correct $\overline{TKE}$ for the energy deficit. The $\overline{TKE}$ values of 198.7 ± 2.8 MeV for ^{256}Rf and 198.2 ± 3.0 MeV for ^{258}Rf are also in a good agreement with previously measured 198.9 ± 4.4 MeV and 197.6 ± 1.1 MeV [4], respectively. The TKE distributions containing all types of SF events have $FWHM \approx 37$ MeV for all the three isotopes.

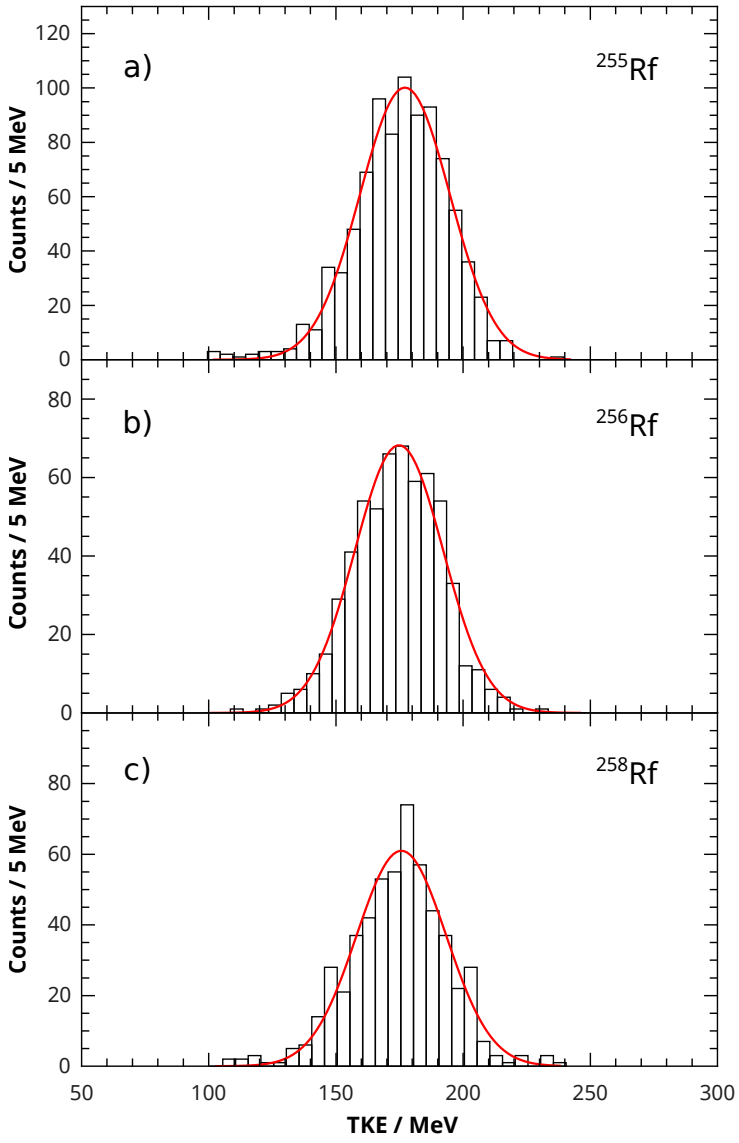

Figure 5.1: Total kinetic energy distribution for ^{255}Rf, ^{256}Rf and ^{258}Rf from all detected SF events for each isotope. Due to the pulse-height defect, the positions of gaussians are shifted to lower values.

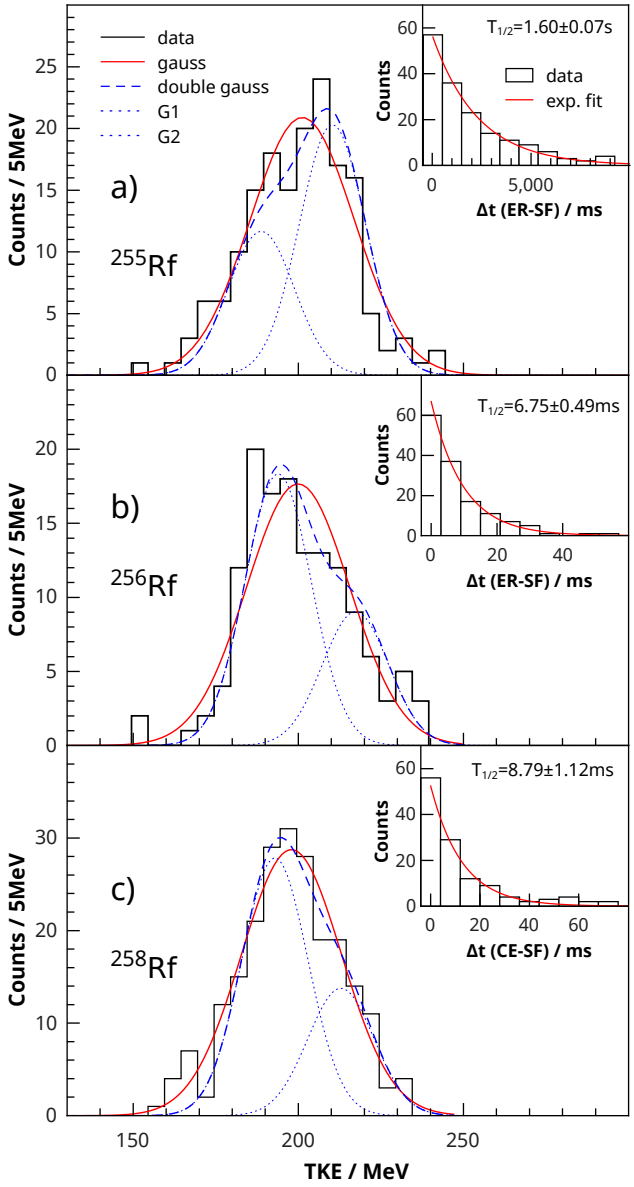

Figure 5.2: TKE distributions of SF fragments from STOP-BOX coincidences: a) for SF of ^{255}Rf obtained from ER-SF correlations (inset shows ER-SF time differences), b) for SF of ^{256}Rf obtained from ER-SF correlations (inset shows ER-SF time differences), c) for SF of ^{258}Rf obtained from STOP-BOX coincidences (inset shows CE-SF time differences in cases when CE was registered).

Isotope	$\overline{TKE}_{all}$ [MeV]	$\overline{TKE}_{ref}$ [MeV]	Ref.
^{255}Rf	199.5 ± 2.7	199 ± 3	[6]
^{256}Rf	198.7 ± 2.8	198.9 ± 4.4	[4]
^{258}Rf	198.2 ± 3.0	197.6 ± 1.1	[4]

Table 5.1: Total kinetic energies evaluated in this work, compared to previous results. In the table columns, from left to right, $\overline{TKE}$ of all events obtained from both STOP-BOX coincidences and anticoincidences, reference value of $\overline{TKE}$ and corresponding references are stated.

5.1.2 Discussion to bimodal fission

In order to study the shape of TKE distribution for bimodal fission search, it is necessary to use only STOP-BOX coincident events with completely registered energy as a sum of energies from STOP and BOX detectors. These TKE distributions of ^{255}Rf, ^{256}Rf and ^{258}Rf are shown in Fig. 5.2.

A slight asymmetry in the TKE distributions of ^{255}Rf and ^{256}Rf is noticeable. By fitting with single gaussian we obtained 201.2 ± 0.9 MeV with $FWHM = 31.3 \pm 1.7$ MeV and 197.5 ± 1.0 MeV with $FWHM = 31.2 \pm 2.0$ MeV for these two isotopes, respectively. By deconvolution with two gaussian components we estimated the $\overline{TKE}$ of low-energy and high-energy components to be 186.3 ± 1.5 MeV and 207.8 ± 0.8 MeV in the case of ^{255}Rf and 191.4 ± 0.7 MeV and 214.8 ± 1.5 MeV in the case of ^{256}Rf.

The distribution for the isotope ^{258}Rf is more symmetric than the ones for ^{255}Rf and ^{256}Rf. The single-gaussian fit gives $\overline{TKE}$ of 197.9 ± 0.7 MeV with $FWHM = 30.3 \pm 1.4$ MeV, fit by two gaussians gives 194.4 ± 1.5 MeV and 213.5 ± 4.8 MeV.

The goodness of single- or double-gaussian fits can be characterised by the values of residual sum of squares (χ^2) divided by the degrees of freedom (doF). The values of χ^2/doF are suitable for the comparison only for histograms with the same statistics (considering the same binning). The statistics in our case is very similar for each isotope, however in the case of specific isotope, the correctness of comparison is guaranteed. Thus the goodness of single- or double-gaussian fits for TKE distributions via χ^2/doF should be compared only within the same isotope. The χ^2/doF values of single- and double-gaussian fits for each isotope are stated in Table 5.2. For ^{255}Rf, χ^2/doF was

	Double gaussian fit				Single gaussian fit		
Isotope	$\overline{TKE}_L$ [MeV]	$\overline{TKE}_H$ [MeV]	ΔE [MeV]	χ^2/doF	$\overline{TKE}$ [MeV]	$FWHM$ [MeV]	χ^2/doF
^{255}Rf	186.3 ± 1.5	207.8 ± 0.8	21.8 ± 1.7	3.6	201.2 ± 0.9	31.3 ± 1.7	5.6
^{256}Rf	191.4 ± 0.7	214.8 ± 1.5	23.4 ± 1.9	3.3	197.5 ± 1.0	31.2 ± 2.0	6.7
^{258}Rf	194.4 ± 1.5	213.5 ± 4.8	19.1 ± 5.0	7.4	197.9 ± 0.7	30.3 ± 1.4	6.3

Table 5.2: In columns from left to right, for each isotope, characteristic values from fitting of TKE distributions (for SF events from STOP-BOX coincidences) are stated. For double-gaussian fit: $\overline{TKE}_L$ of low-energy component, $\overline{TKE}_H$ of high-energy component, ΔE energy difference between $\overline{TKE}_L$ and $\overline{TKE}_H$ and residual sum of squares (χ^2) divided by the degrees of freedom (doF). For single-gaussian fit: $\overline{TKE}$, FWHM and residual sum of squares (χ^2) divided by the degrees of freedom (doF).

lower in the case of double-gaussian than the single-gaussian fit, for ^{256}Rf situation was the same. In the case of ^{258}Rf, the χ^2/doF value for double-gaussian fit was higher.

Asymmetric TKE distributions and lower χ^2/doF values for double-gaussian fits lead us to the conclusion of possible bimodal fission for ^{255}Rf and ^{256}Rf. For ^{255}Rf the high-energy component is dominant while for ^{256}Rf the low-energy component is dominant. We note, however, that the positions of the two components are closer (energy differences ΔE are stated in Table 5.2) to each other in contrast to the bimodal fission in ^{258}Fm, ^{259,260}Md and ^{258,260}No [4, 5], where the energy difference was 30–35 MeV. In ^{258}Rf we do not clearly see asymmetry in the TKE distribution and also double-gaussian fit gives slightly higher χ^2/doF value than the single-gaussian fit.

Comparison of experimental TKE distributions with calculations

In sec. 2.1.6 we introduced results of calculations [3] where mass distributions and TKE distributions for even Rf isotopes ^{254}Rf–^{268}Rf were presented. In our study, we obtained experimental results for TKE distributions of ^{255}Rf, ^{256}Rf and ^{258}Rf, which allows us to compare the two of them with even mass number with the calculations.

In the case of ^{256}Rf a qualitative agreement between the shape of the experimental and calculated TKE distributions is evident. The lower-energy component is slightly dominant over the higher energy component, resulting in an slightly asymmteric TKE distribution. The calculated energy difference between the $\overline{TKE}_L$ and $\overline{TKE}_H$ of the two fission modes is $\approx$20 MeV which roughly agrees with the experimentally measured value $\Delta E = 23.4 \pm 1.9$ for ^{256}Rf. However, the calculations resulted in higher $\overline{TKE}$ for both fission modes. The calculated TKE distribution are shifted by $\approx$15 MeV towards the higher energies in comparison to experimental TKE distributions.

In the case of ^{258}Rf, the two fission modes have the same probabilities according to the calculations and thus in the experimental data, the TKE distributions should have two components with similar statistics, which results in a rather symmetric shape of the distribution. In the experimental results, we obtained a symmetric TKE distribution for ^{258}Rf. The attempts for a decomposition into two gaussian components resulted in higher χ^2/doF than single-gaussian fit, which is a supporting argument for the symmetric distribution and thus in qualitative agreement with the calculations. As in the case of ^{256}Rf, also for ^{258}Rf the calculations resulted in higher TKE values

and thus the distributions are shifted to higher energies.

To summarize this comparison, it has to be emphasized that the experimental TKE distributions for both isotopes ^{256}Rf and ^{258}Rf are in qualitative agreement with the calculations. The TKE distribution of ^{255}Rf exhibits different behavior - the lower energy component is dominant in this case, however it could not be compared as there are not calculations for odd Rf isotopes. Nevertheless, it is a known fact that SF properties of isotopes with unpaired nucleon(s) do not necessarily fit into the systematics for even-even isotopes [23] and thus we cannot also exclude the impact of this effect on TKE. The details from the study of TKE in ^{255}Rf, ^{256}Rf and ^{258}Rf were submitted for the publication [59].

5.2 *K* isomerism in ^{255}Rf

5.2.1 Search for isomeric states in ^{255}Rf

In order to look for isomeric states in ^{255}Rf we searched for correlations containing an electron signal from the deexcitation of an isomeric state by internal conversion, preceded by an ER signal and followed by an SF or α decay from the ground state (ER-CE-(CE)-SF/α). This method is typically used for the search of isomeric states and several isomers were discovered this way.

Conversion electrons were searched for as a low-energy signal (up to 1 MeV). Subsequent α decays from the ground state (g.s.) of ^{255}Rf were searched for within 0–8500 ms after the electron signal and in energy range of 8500–9000 keV. For the SF, a time condition of 35–8500 ms was set in order to avoid the contamination of ^{256}Rf (with the same arguments that were mentioned in Sec.4.2.4).

The detection system used in our study has some limitations for detection of low-energy electrons. For significant part of the CEs the information on the position within the strip was missing. Therefore, we required a position agreement of the ER and SF/α signal to be within 1 mm and the same strip number for all three generations of ER-CE-SF/α chain. The histogram of time difference between signals from ER and CE from ER-CE-SF/α chains found under these conditions is shown in Fig. 5.3. The distribution shows that the real correlations are separated from the random ones. Thus we set the condition for time difference between signals from ER and CE as $\Delta t(ER-CE) < 500\,\mu$s. We detected 144 ER-CE-SF/α correlations fulfilling

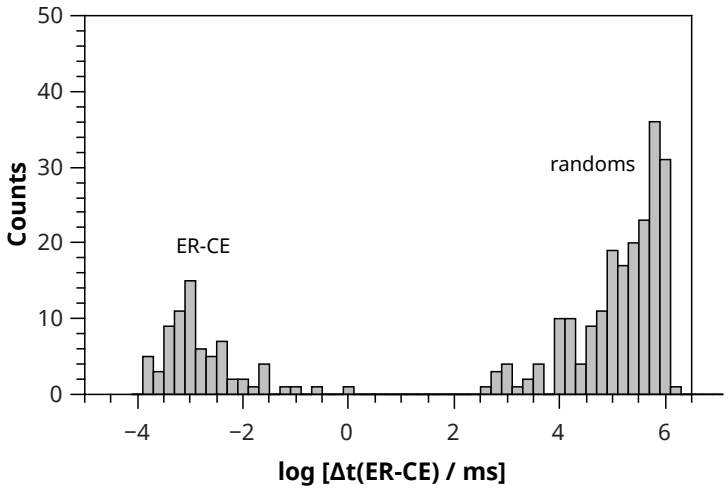

Figure 5.3: Histogram of time differences between signals from ER and CE from the ER-CE-SF/α correlation search.

Correlation	Δt(CE-SF/α)	E range	Counts
ER(^{255}Rf)-CE-(CE)-SF	35–8500 ms	100–300 MeV	74
ER(^{255}Rf)-CE-(CE)-α	0–8500 ms	8500–9000 keV	70

Table 5.3: Summary of ER-CE-SF/α correlation search. The time and energy conditions are stated. The searching condition for time between ER and CE was $\Delta t(ER-CE) < 500\,\mu s$. In 74 cases, chains ended by SF, in 70 cases by α decay of ^{255}Rf or ^{251}No.

the conditions mentioned above, the details are summarized in Table 5.3.

In 74 cases chains ended by SF and in 70 cases by the α decay corresponding to ^{255}Rf or ^{251}No. The detection of ^{251}No α particles was preceded by 1–2 MeV signals originating from the escape of ^{255}Rf α particles from the detection system, ER-CE-α(^{255}Rf) or ER-CE-α(^{255}Rf)$_{esc.}$-α(^{251}No) correlations. We evaluated branching ratios of ^{255}Rf according to detector efficiencies to be $b_{SF} = 0.51 \pm 0.07, b_\alpha = 0.49 \pm 0.07$. A contribution of a branching ratio for EC decay of ^{255}Rf (evaluated as $<$0.06 in [6]) was not considered.

In three cases of detected ER-CE-SF/α correlations, the CE was followed by another CE within 500 µs. The details on these three ER-CE-CE-SF/α(^{255}Rf) correlations including CE energies and decay times for each chain are summarized in Table 5.4.

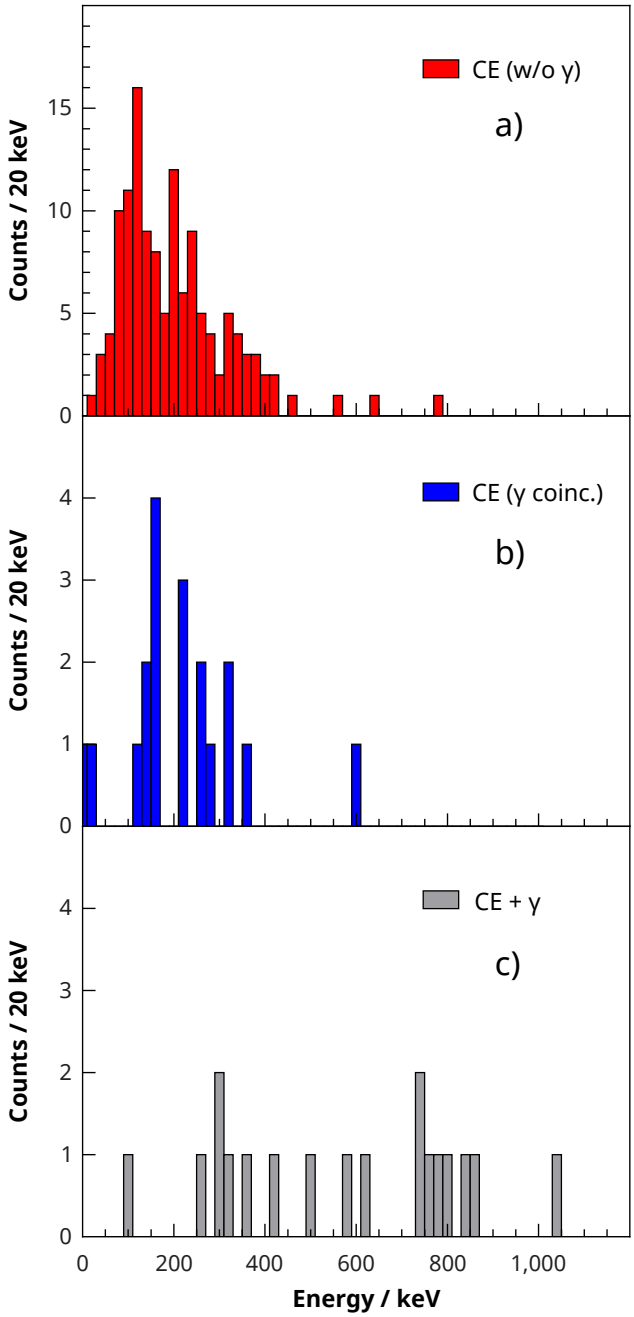

Figure 5.4: Energies of conversion electrons from the ER-CE-(CE)-SF/α correlations. a) electrons not coincident with γ rays, b) electrons in coincidence with γ rays, c) summed energies of electrons and coincident γ rays.

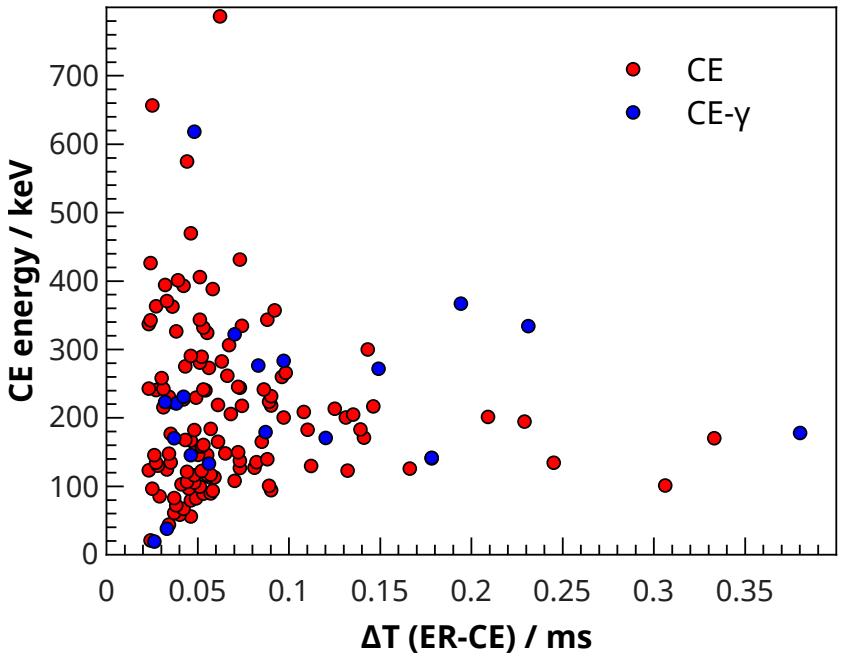

Figure 5.5: Conversion electron energies as a function of time difference between the implantation of ER and detection of CE. Red dots: electrons not in coincidence with γ rays, blue dots: electrons in coincidence with γ rays.

From the total of 147 CEs detected in ER-CE-SF/α or ER-CE-CE-SF/α correlations, in 19 cases, electrons were in prompt coincidence with γ rays and in 128 cases without. The energy spectra of these CEs without or with coincident γ rays are shown in Fig. 5.4a) and Fig. 5.4b) respectively. The CE energies were corrected by the method discussed in Sec. 4.1.2. Figure 5.5 shows the 2D plot of CE energies as a function of ER-CE time differences. The gap of $\approx$ 25 µs at the beginning is due to the dead time of the data acquisition system. We might separate the electrons into at least two groups according to their time distributions. The half-life of the lower-energy electrons (0–350 keV) is 35 ± 6 µs and the higher-energy group ($>$ 350 keV) is 15 ± 5 µs.

We separately evaluated the half-life of the lower-energy CEs (0–350 keV) in coincidence with γ rays as 38 ± 4 µs (explained in the discussion, Sec. 5.2.2). The energy spectra of coincident γ rays are shown in Fig. 5.6. There is not any sign of γ lines in single-crystal mode or add-back mode of Clover detector.

ER-CE-CE-SF/α chain	E_{CE1} [keV]	Δt_{CE1} [µs]	E_{CE2} [keV]	Δt_{CE2} [µs]	g.s. decay
1	81.0	57	147.5	33	SF
2	126.0	88	143.8	25	α
3	146.4	50	19.8[1]	26	α

Table 5.4: Conversion electron characteristics from the ER-CE-CE-SF/α correlations.

The spectrum of summed energies of electrons and coincident γ rays is shown in Fig. 5.4c), where energies go up to 1050 keV.

5.2.2 Discussion to *K* isomers in ^{255}Rf

A single-particle $5/2^+[622]$ isomer with $T_{1/2} = 50 \pm 15$ µs populated by α decay of ^{259}Sg was previously identified in ^{255}Rf with an excitation energy of ≈ 135 keV [6] based on the statistics of 42 ER(^{259}Sg)-α-CE correlations. None of the CEs in a previous study was observed in coincidence with γ rays. The energy distribution of the electrons formed a narrow peak at ≈ 105 keV with FWHM practically defined only by detector resolution.

In our study, with direct production of ^{255}Rf via $2n$ evaporation channel, the energy distribution of CEs from ER-CE-α/SF correlations was significantly broader and reaching up to 800 keV [see Fig. 5.4a)].

From all events in the energy range of 0–350 keV, 17 cases were detected in coincidence with γ rays, we evaluated their half-life as 38 ± 4 µs. Considering broader electron-energy distribution of these events in comparison with the study of $5/2^+[622]$ isomer in [6], the mean energy of ≈ 250 keV and many γ-coincident events, we conclude that we identified a new isomer, different from the reported single-particle $5/2^+[622]$ isomer.

In the energy range of 0–350 keV, we also found that most of the CEs were not in coincidence with γ rays. The half-life of these events was 35 ± 6 µs. The fact that many electrons were not in coincidence with γ rays can be explained by the γ-ray detection efficiency, however, there might be a contribution of CEs from the $5/2^+[622]$ isomer with $T_{1/2} = 50 \pm 15$ µs half-life for which no γ rays were observed in coincidence with CEs [6]. As these events result in similar half-lives and energies, they cannot be separated from the electrons originating in the deexcitation of the new isomer we identified. Thus for

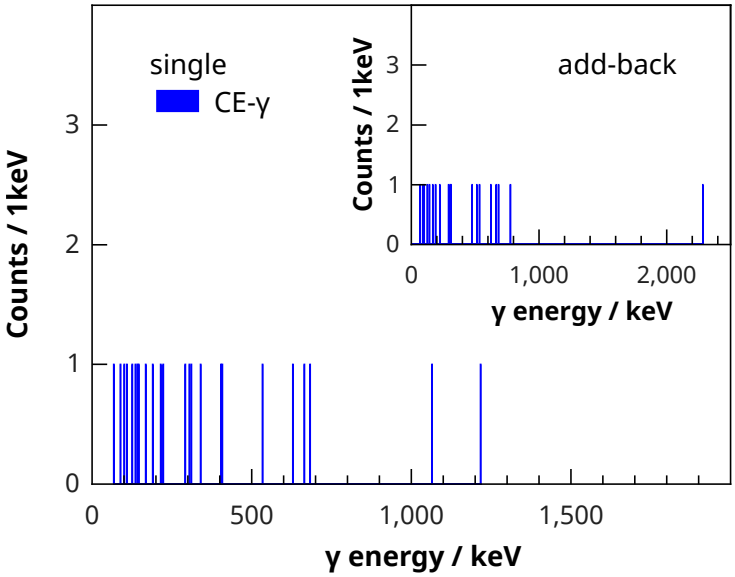

Figure 5.6: Energy spectrum of γ rays in coincidence with electrons from the ER-CE-(CE)-SF/α correlations. Inset: add-back spectrum.

the estimations of the half-life and excitation energy of the new isomer we are discussing only electrons from the energy range 0–350 keV which were in coincidence with γ rays.

From the high number of electrons in comparison with the number of γ rays and non-observation of clear γ-ray peak, we assume that the transition deexciting the isomer has a high total conversion coefficient. However, for the low-multipolarity transitions high conversion coefficients are expected only for low transition energies up to 100–200 keV. Therefore, we consider our electron signals to be formed as a summed signal from a cascade of 3–5 transitions. The ground state of ^{255}Rf was assigned to be $9/2^-[734]$ state in [57] and thus the new isomer should be a high-K isomer with K number at least by 4–6 higher than the ground state. The excitation energy can be estimated from the summed energies of conversion electrons and coincident γ rays [Fig. 5.4c)], which go up to 1050 keV. Depending on the binding energies of electrons in the atomic K ($\approx$ 147 keV) or L ($\approx$ 29 keV) shells, the excitation energy is roughly estimated to 1150–1450 keV.

Another group of electrons with significantly different life-time was formed at energies above 350 keV (Fig. 5.5). The half-life of these events is $T_{1/2} = 15 \pm 5$ µs. Using the same arguments as above one can expect these signals

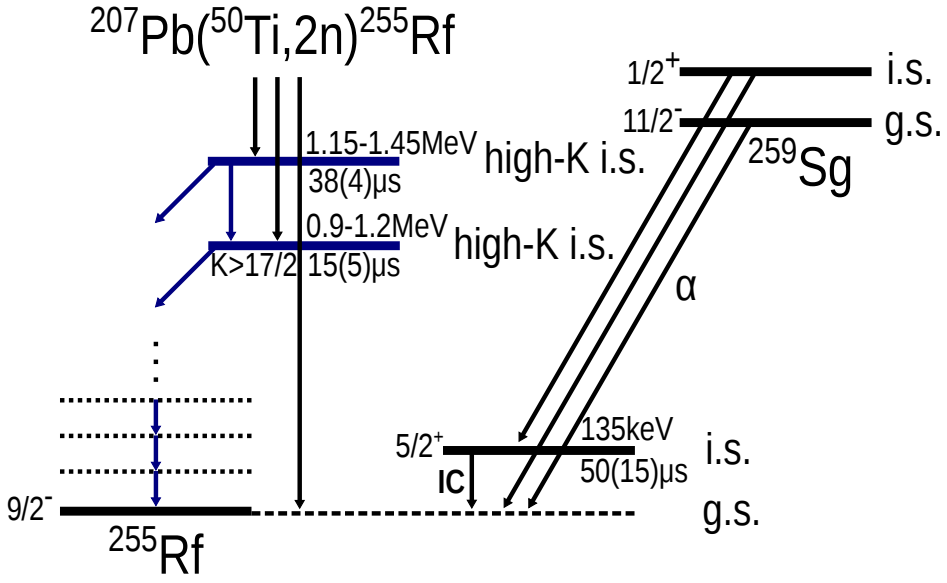

Figure 5.7: Proposed decay scheme of K-isomers in ^{255}Rf populated in the reaction ^{207}Pb(^{50}Ti,2n)^{255}Rf (left) and in the α decay of ^{259}Sg (right).

to be the sum of an electron cascade from the deexcitation of another isomeric state with high K number. A supporting argument for an existence of two isomers is the observation of three ER(^{255}Rf)-CE-CE-SF/α correlations shown in Table 5.4. As the energies of electrons with $T_{1/2} = 15 \pm 5$ µs reach up to 800 keV one can estimate the excitation energy to be 900–1200 keV.

In all three cases of ER(^{255}Rf)-CE-CE-SF/α correlations from Table 5.4, the decay time of the first electron was longer than the decay time of the second one. From this fact we assume that besides a direct population of the 15 µs isomer during the production of ER, the decay of the longer-lived 38 µs isomer might also feed the 15 µs isomer. The energy difference of these two levels may be deduced from the energies of the first electrons from the three ER(^{255}Rf)-CE-CE-SF/α correlations. By adding the binding energy of an electron on K or L atomic shell we estimated the gap between the two isomeric levels to be 150–300 keV. Based on the results presented before we propose the tentative decay scheme shown in Fig. 5.7.

The crucial question for such an interpretation is the availability of levels to form a configuration with high K value. The scheme of available single-particle levels for protons and neutrons in ^{255}Rf prepared according to calculations from [60] with nuclear deformations taken from [61] is presented

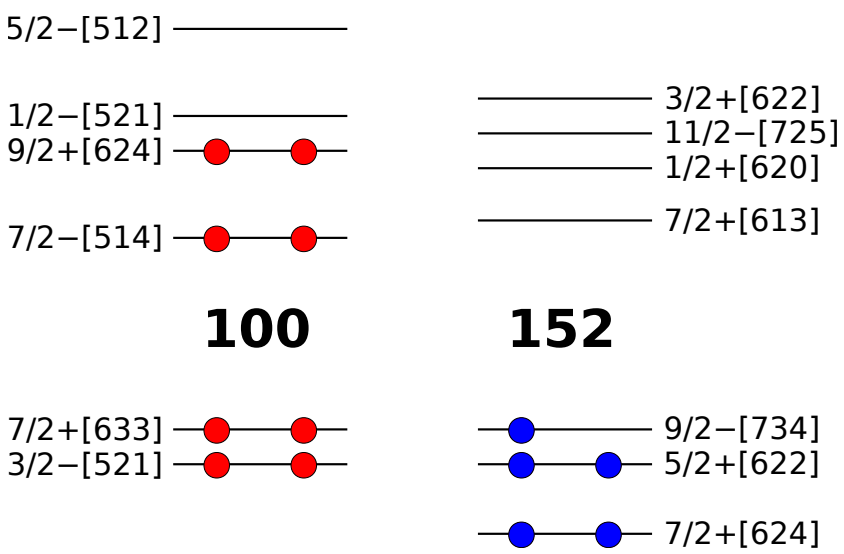

Figure 5.8: Single-particle levels for protons (left) and neutrons (right) in ^{255}Rf, calculated in [60] with nuclear deformations taken from [61]. Neutron level $5/2^+[622]$ was placed according to experimental results from [6]. The ground state configuration is shown.

3-qp configuration	K^π	ΔK
$1/2^-[521]\pi \otimes 9/2^+[624]\pi \otimes 9/2^-[734]\nu$	$19/2^+$	5
$1/2^-[521]\pi \otimes 7/2^-[514]\pi \otimes 9/2^-[734]\nu$	$17/2^-$	4
$5/2^-[512]\pi \otimes 9/2^+[624]\pi \otimes 9/2^-[734]\nu$	$23/2^+$	7
$7/2^-[514]\pi \otimes 5/2^-[512]\pi \otimes 9/2^-[734]\nu$	$19/2^-$	5
$1/2^-[521]\pi \otimes 9/2^+[624]\pi \otimes 5/2^+[622]\nu$	$15/2^-$	4
$5/2^-[512]\pi \otimes 9/2^+[624]\pi \otimes 5/2^+[622]\nu$	$19/2^-$	5
$7/2^-[514]\pi \otimes 5/2^-[512]\pi \otimes 5/2^+[622]\nu$	$17/2^+$	4
$1/2^-[521]\pi \otimes 9/2^+[624]\pi \otimes 7/2^+[624]\nu$	$17/2^-$	4
$5/2^-[512]\pi \otimes 9/2^+[624]\pi \otimes 7/2^+[624]\nu$	$21/2^-$	6
$7/2^+[613]\nu \otimes 9/2^-[734]\nu \otimes 5/2^+[622]\nu$	$21/2^-$	6
$7/2^+[613]\nu \otimes 9/2^-[734]\nu \otimes 7/2^+[624]\nu$	$23/2^-$	7

Table 5.5: Examples of possible configurations of 3-qp high-K isomeric states in ^{255}Rf, according to single-particle levels calculated in [60] with nuclear deformations taken from [61] (see Fig. 5.8).

in Fig. 5.8. In this case a high-K configuration can be simply achieved for example by breaking a pair of protons at $9/2^+[624]$ or $7/2^-[514]$ and shifting one proton to the $1/2^-[521]$. Such three quasi-particle configurations $\{1/2^-[521]\pi \otimes 9/2^+[624]\pi \otimes 9/2^-[734]\nu\}$ and $\{1/2^-[521]\pi \otimes 7/2^-[514]\pi \otimes 9/2^-[734]\nu\}$ lead to $K = 19/2^+$ with $\Delta K = 5$ and $K = 17/2^-$ with $\Delta K = 4$. These and other examples of possible configurations with high-K are summarized in Table 5.5. The 3-qp configurations composed of three unpaired neutrons demand a neutron to be shifted over the level gap for deformed isotones at $N = 152$. From the estimations of excitation energy of new isomers, quite low-lying high-K state can be expected. Nevertheless, without having detailed calculations of energy gaps, one cannot exclude the possibility of three neutron qp state. The details from the study of K isomers in ^{255}Rf were submitted for the publication [59].

Conclusion

This thesis was focused on two topics. First, we studied the total kinetic energies of isotopes ^{255}Rf, ^{256}Rf, and ^{258}Rf and secondly, we investigated ^{255}Rf for the presence of K-isomeric states.

The experiment was performed at the experimental setup SHIP, which is located in GSI Darmstadt (Germany). The nuclei of rutherfordium isotopes were produced in the fusion-evaporation reactions with ^{50}Ti beam and targets of ^{207}Pb, ^{208}Pb and ^{209}Bi with the cross-sections of few nb. During the irradiations, which lasted couple dozens of hours, we produced several hundreds nuclei for each isotope.

The energy calibrations of focal plane STOP detector as well as surrounding BOX detectors were done using the known α-particle energies from the decay of several isotopes produced in fusion-evaporation reaction ^{50}Ti + ^{170}Er. The main issue in measuring fission-fragment energies is the energy deficit caused by the pulse-height defect and detection geometry. In order to correctly evaluate the TKE of fission fragments from the spontaneous fission of Rf isotopes, we studied ^{252}No with known $\overline{TKE}$ implanted at different implantation depths in order to obtain response function of the detector system. For this purposes we reanalysed older data (also from the SHIP experiment), where ^{252}No was produced in fusion-evaporation reaction with ^{48}Ca beam and ^{206}Pb target. We published this study in [50].

The correction of the energy deficit in TKE studied on the ^{252}No allowed us to evaluate the $\overline{TKE}$ of the rutherfordium isotopes ^{255}Rf, ^{256}Rf, and ^{258}Rf to be 199.5 ± 2.7 MeV, 198.7 ± 2.8 MeV and 198.2 ± 3.0 MeV, respectively. The results on $\overline{TKE}$ are in a good agreement with previous studies.

To investigate the TKE distributions for bimodal fission, we considered only STOP-BOX coincident events which guarantee the fully reconstructed energy of fission fragments. We observed asymmetric distributions for ^{255}Rf, ^{256}Rf and a more symmetric shape for ^{258}Rf. A possible explanation is the existence of bimodal fission for ^{255}Rf, ^{256}Rf, although weaker as in previous

cases [4, 5]. Experimental results were also in a qualitative agreement with theoretical calculations [3].

During the study of ^{255}Rf, we were able to identify new high-K, presumably 3-qp, isomers with half-lives of $38 \pm 4\,\mu s$ and $= 15 \pm 5\,\mu s$. We estimated the excitation energies of these isomers to 1150–1450 keV and 900–1200 keV, respectively, with 150–300 keV of energy difference between them and a lower limit for spin of $17/2\hbar$. Based on these results we also proposed a tentative decay scheme. The details of this study were submitted for the publication [59].

Perspectives

The results showed us, that the spontaneous-fission study for rutherfordium isotopes is possible. There are hints for bimodal fission, however a higher statistics would be necessary to confirm this phenomenon in discussed nuclei. Rutherfordium isotopes are currently the heaviest for which the total kinetic energy of fission fragments was measured with reasonable statistics. As the bimodal fission was already confirmed in fermium ($Z = 100$), mendelevium ($Z = 101$) and nobelium ($Z = 102$) isotopes, and in this work we reported also hints for bimodal fission in neutron deficient rutherfordium isotopes, it would be interesting to study fission modes also for more neutron rich rutherfordium isotopes and in seaborgium isotopes. Such measurement would help to improve theoretical models and our understanding of spontaneous fission process, which is crucial for the survival (and thus also the production possibilities) of super-heavy isotopes.

There are not many laboratories around the world which are able to produce such heavy isotopes with reasonable statistics. The possibility to carry out the beamtimes at SHIP in GSI Darmstadt is limited due to the construction of the FAIR facility. The possibilities to continue the study of total kinetic energies for rutherfordium and heavier isotopes are presently in FLNR Dubna. The detection setup is similar to the one at SHIP described in this work, but DSSSD dectors are used as STOP and BOX detectors. Attempts to calibrate this detection system and study the energy deficit in measured total kinetic energies as a function of the angle under which fission fragments escape the STOP detector and hit the BOX detectors are made. Such a calibrations would result in more precise TKE measurements. In few years, the S_3 facility at GANIL is planned to be commissioned. With this experimental setup, it will be possible to perform measurements discussed

in this work and several proposals of experiments (also from the group at the Department of Nuclear Physics and Biophysics of Comenius University in Bratislava) were already accepted.

A more detailed study of discovered K-isomers in ^{255}Rf requires a higher statistics. We based our study on 147 of detected internal-conversion electrons from the deexcitation of these states. Higher statistics would allow us to precisely evaluate the half-lives and excitation energies and also to possibly observe γ transitions, which would help us to improve the decay scheme. The experiments focused on the spectroscopy of ^{255}Rf were performed in Dubna in 2018 with significantly higher statistics. We are therefore looking forward for the results of these measurements. Further studies of K isomerism in also other isotopes from this region, that is expected due to the significant deformation and presence of states with high Ω, will be possible in FLNR Dubna and also S_3 at GANIL.

Appendix A

Search for alpha decay of ^{256}Rf

A.1 α decay of ^{256}Rf and spontaneous fission of ^{251}No

A.1.1 Identification of α decay for ^{256}Rf

Reaction ^{50}Ti + ^{208}Pb

A considerable quantity of ^{255}Rf and ^{256}Rf was produced via $2n$ and $1n$ evaporation channels in reaction ^{50}Ti + ^{207}Pb from the compound nucleus ^{257}Rf (see Fig. 4.9b)).

In the data from this reaction we found two possible decay chains indicating rare α decay of ^{256}Rf. The first chain summarized in fig. A.1 *b*) contains α decay of ER and ends with SF of α-decay daughter nucleus. Both decay characteristics, time difference of 2.88 ms between ER - α signals and energy of 8778 keV (reconstructed from STOP and BOX), fit to the known half-life and α-particle energy of ^{256}Rf (6.67 ms [12] and 8790 keV [62]). The α decay was followed by SF, 1.12 s after the signal from α decay ($T_{1/2}(^{252}\text{No}) = 2.44\,\text{s}$ [63]). We excluded the assignment of this chain to the decay of ^{255}Rf due to the long half-life of ^{255}Rf and low SF branching ratio of ^{251}No. In total we expect only 0.0032 events of ER(^{255}Rf) - α(^{255}Rf) - SF(^{251}No) with ΔT(ER-α) < 6.67 ms. We thus assigned this decay chain to ^{256}Rf.

Another chain (fig. A.1 *a*)) contains two consequent α decays after the signal from ER implantation (first α decay corresponds to ER and second one to daughter nucleus). Considering time differences between ER, α decay and daughter nucleus in the same position of STOP detector, we assigned

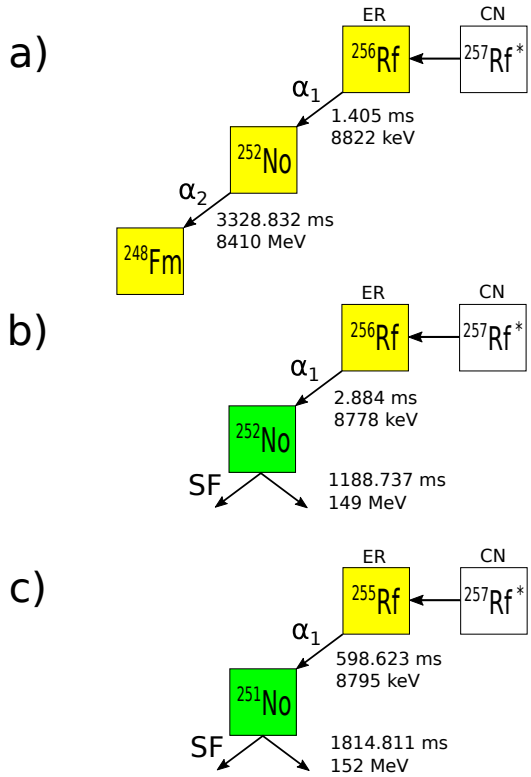

Figure A.1: Decay chains identified in the reactions $^{50}\mathrm{Ti} + {}^{207}\mathrm{Pb}$ and $^{50}\mathrm{Ti} + {}^{208}\mathrm{Pb}$. Given time represents time differences between corresponding decays. Measured α-decay energies or TKE of SF fragments (not corrected to pulse-height defect) are stated.

this chain to ^{256}Rf.

Reaction ^{50}Ti + ^{208}Pb

There was no ^{255}Rf produced in the reaction ^{50}Ti + ^{208}Pb (see Fig. 4.9a). However, a considerable amount of ^{256}Rf and ^{257}Rf was produced by $2n$ and $1n$ evaporation channels from the compound nucleus ^{258}Rf. In Sec. 4.2.3 we excluded the presence of SF events from ^{257}Rf. We assign all of the ER-SF events with $\Delta t < 35$ ms to ^{256}Rf. However in the data from this irradiation we did not find any signs of possible α decay of ^{256}Rf.

Branching ratios of ^{256}Rf

From two α decays of ^{256}Rf and total 706 ER - SF events from both reactions, we evaluated the α-decay branching ratio for this isotope. Adding this value to the older results from direct production of ^{256}Rf [62] we obtained improved value of 0.36^{+17}_{-13} %. This value is significantly different than the one of $1.88^{+1.65}_{-0.85}$ % [44], [64] from the indirect production through α decay of ^{260}Sg. Further studies are necessary to explain this disagreement.

Fusion-evaporation reaction	E_{lab} [MeV]	E^*_{CN} [MeV]	σ [nb]	σ^{ref}_{max} [nb]	E^{*ref}_{CN} [MeV]
^{207}Pb(^{50}Ti, 2n)^{255}Rf	239.8	23.4	11.4 (18)	-	-
^{208}Pb(^{50}Ti, 2n)^{256}Rf	229.8	15.8	2.4 (3)	-	-
	238.3	22.6	15.5 (17)	12 (1)	21.5
^{209}Bi(^{50}Ti, 1n)^{258}Db $\xrightarrow{EC}$ ^{258}Rf	232.6	16.0	2.9 (9)	4.3 (4)	15.8

Table A.1: Summary of the individual irradiations during R292 at SHIP. E_{lab} is the beam energy calculated in the middle of target thickness, $E*_{CN}$ is the excitation energy of compound nucleus, σ is evaluated cross-section, σ^{ref}_{max} is the maximal cross-section from the study in [54] and E^{*ref}_{CN} is the excitation energy of compound nucleus corresponding to maximal cross-sectionin [54].

Branching ratio of ^{251}No

Other interesting result coming from this reaction is SF of ^{251}No. Up to now only one such event was observed [57]. We found one new case in the decay chain ER(^{255}Rf) - α(^{255}Rf) - SF(^{251}No) shown in fig.A.1 c). Considering the number of α decays of ^{255}Rf, we obtained branching ratio for SF of ^{251}No to be $0.12^{+0.28}_{-0.10}$ % which is in a good agreement with the previous value of $0.14^{+0.31}_{-0.12}$ % from [57].

A.2 Summary of production cross-sections

A valuable information that can be substracted from the data are the production cross-sections of isotopes. Excitation functions for reactions $^{50}\mathrm{Ti} + {}^{208}\mathrm{Pb}$ and $^{50}\mathrm{Ti} + {}^{209}\mathrm{Bi}$ were reported in [54]. In Table A.1 we summarize the evaluated cross-sections and compare them with values from [54]. In our study, the beam energies were set to obtain excitation energies of compound nuclei corresponding to the maximum cross-sections from previous studies. The values we obtained are in a good agreement with reported detailed measurements in [54]. For reaction $^{50}\mathrm{Ti} + {}^{207}\mathrm{Pb}$, excitation function is not known yet.

Bibliography

[1] S. G. Nilsson, Ch. Fu Tsang, A. Sobiczewski, et al., *Nucl. Phys. A* **131**, 1 (1969).

[2] F. P. Heßberger, *Eur. Phys. J. A* **53**, 75 (2017).

[3] N. Carjan, F. A. Ivanyuk, Yu. Oganessian, et al., *Nucl. Phys. A* **942**, 97 (2015).

[4] J. F. Wild, E. K. Hulet, R. W. Lougheed, et al., *J. Alloy. Compd.* **213**, 86 (1994).

[5] E. K. Hulet, *Phys. At. Nucl.* **57**, 1099 (1994).

[6] S. Antalic, F. P. Heßberger, D. Ackermann, et al., *Eur. Phys. J. A* **51**, 41 (2015).

[7] B. Sulignano, S. Heinz, F. P. Heßberger, et al., *Eur. Phys. J. A* **33**, 327 (2007).

[8] A. Ghiorso, K. Eskola, P. Eskola, et al., *Phys. Rev. C* **7**, 2032 (1973).

[9] R. D. Herzberg, P. T. Greenlees, P. A. Butler, et al., *Nature* **442**, 896 (2006).

[10] F. P. Heßberger, S. Antalic, B. Sulignano, et al., *Eur. Phys. J. A* **43**, 55 (2009).

[11] H. M. David, J. Chen, D. Seweryniak, et al., *Phys. Rev. Lett.* **115**, 132502 (2015).

[12] H. B. Jeppesen, I. Dragojević, R. M. Clark, et al., *Phys. Rev. C* **79**, 031303 (2009).

[13] A. P. Robinson, T. L. Khoo, D. Seweryniak, et al., *Phys. Rev. C* **83**, 064311 (2011).

[14] A. Lopez-Martens, K. Hauschild, A. V. Yeremin, et al., *Eur. Phys. J. A* **32**, 245 (2007).

[15] S. Antalic, F. P. Heßberger, D. Ackermann, et al., *Eur. Phys. J. A* **47**, 62 (2011).

[16] S. Antalic, F. P. Heßberger, S. Hofmann, et al., *Eur. Phys. J. A* **38**, 219 (2008).

[17] K. Hauschild, A. Lopez-Martens, A. V. Yeremin, et al., *Phys. Rev. C* **78**, 021302 (2008).

[18] J. Rissanen, R. M. Clark, K. E. Gregorich, et al., *Phys. Rev. C* **88**, 044313 (2013).

[19] O. Hahn, F. Strassmann, *Sci. Nat.* **27**, 529 (1939).

[20] L. Meitner, O. R. Frisch, *Nature* **143**, 239 (1939).

[21] G. N. Flerov, K. A. Petrjak, *Phys. Rev.* **58**, 89 (1940).

[22] A. Zdeb, M. Warda, K. Pomorski, *Acta Phys. Pol. B* **46**, 423 (2015).

[23] D. C. Hoffman, *Nucl. Phys. A* **502**, 21 (1989).

[24] Yu. Ts. Oganessian, *J. Phys. G* **34**, R165 (2007).

[25] W. D. Myers, W. J. Swiatecki, *Nucl. Phys.* **81**, 1 (1966).

[26] W. D. Myers, W. J. Swiatecki, *Phys. Rev. C* **60**, 014606 (1999).

[27] P. Möller, J. R. Nix, W. D. Myers, et al., *Atom. Data Nucl. Data Tabl.* **59**, 185 (1995).

[28] P. Möller, A.J. Sierk, T. Ichikawa, et al., *Phys. Rev. C* **79**, 064304 (2009).

[29] H.C. Britt, In *Actinides in Perspective*, Pergamon 1982, p. 245.

[30] A. N. Andreyev, J. Elseviers, M. Huyse, et al., *Phys. Rev. Lett.* **105**, 252502 (2010).

[31] M. R. Lane, K. E. Gregorich, D. M. Lee, et al., *Phys. Rev. C* **53**, 2893 (1996).

[32] V. E. Viola, *Nuclear Data Sheets. Section A* **1**, 391 (1965).

[33] W. D. Loveland, D. J. Morrisey, G. T. Seaborg, *Modern nuclear chemistry*, John Wiley and Sons 2006.

[34] P. Walker, G. Dracoulis, *Nature* **399**, 35 (1999).

[35] K.E.G. Löbner, *Phys. Lett. B* **26**, 369 (1968).

[36] S. Hofmann, F.P. Heßberger, D. Ackermann, et al., *Eur. Phys. J. A* **10**, 5 (2001).

[37] S. N. Ghoshal, *Phys. Rev.* **80**, 939 (1950).

[38] J. R. Grover, *Phys. Rev.* **157**, 832 (1967).

[39] GSI, *Helmholtz Centre for Heavy Ion Research*, https://www.gsi.de.

[40] S. Hofmann, G. Münzenberg, *Rev. Mod. Phys.* **72**, 733 (2000).

[41] S. Hofmann, S. Heinz, R. Mann, et al., *Eur. Phys. J. A* **52**, 116 (2016).

[42] Š. Šáro, R. Janik, S. Hofmann, et al., *Nucl. Instrum. Meth. A* **381**, 520 (1996).

[43] S. Hofmann, D. Ackermann, S. Antalic, et al., *Eur. Phys. J. A* **32**, 251 (2007).

[44] B. Streicher, PhD thesis, Comenius University in Bratislava, Bratislava 2006.

[45] S. Hofmann, W. Faust, G. Münzenberg, et al., *Z. Phys. A* **291**, 53 (1979).

[46] K. Nishio, S. Hofmann, F. P. Heßberger, et al., *AIP Conf. Proc.* **891**, 71 (2007).

[47] B.D. Wilkins, M.J. Fluss, S.B. Kaufman, et al., *Nucl. Instrum. Meth.* **92**, 381 (1971).

[48] J. F. Ziegler, M. D. Ziegler, J. P. Biersack, *Nucl. Instrum. Meth. B* **268**, 1818 (2010).

[49] O. B. Tarasov, D. Bazin, *Nucl. Instrum. Meth. B* **266**, 4657 (2008).

[50] P. Mosat, S. Antalic, F.P. Heßberger, et al., *Acta Phys. Pol. B* **49**, 605 (2018).

[51] G. Münzenberg, W. Faust, S. Hofmann, et al., *Nucl. Instrum. Meth.* **161**, 65 (1979).

[52] F. P. Heßberger, S. Antalic, D. Ackermann, et al., *Eur. Phys. J. A* **52**, 328 (2016).

[53] K. H. Schmidt, et al., *Z. Phys. A* **316**, 19 (1984).

[54] F.P. Heßberger, S. Hofmann, D. Ackermann, et al., *Eur. Phys. J. A* **12**, 57 (2001).

[55] B. Streicher, F. P. Heßberger, S. Antalic, et al., *Eur. Phys. J. A* **45**, 275 (2010).

[56] J. S. Berryman, R. M. Clark, K. E. Gregorich, et al., *Phys. Rev. C* **81**, 064325 (2010).

[57] F. P. Heßberger, S. Hofmann, D. Ackermann, et al., *Eur. Phys. J. A* **30**, 561 (2006).

[58] M. Vostinar, F. P. Heßberger, D. Ackermann, et al., *Eur. Phys. J. A* **55**, 17 (2019).

[59] P. Mosat, S. Antalic, F.P. Heßberger, et al. submitted to Phys. Rev. C, 2019.

[60] R. R. Chasman, I. Ahmad, A. M. Friedman, et al., *Rev. Mod. Phys.* **49**, 833 (1977).

[61] P. Möller, A.J. Sierk, T. Ichikawa, et al., *Atom. Data Nucl. Data Tabl.* **109-110**, 1 (2016).

[62] F. P. Heßberger, S. Hofmann, V. Ninov, et al., *Z. Phys. A* **359**, 415 (1997).

[63] Yu. Ts. Oganessian, V. K. Utyonkov, Yu. V. Lobanov, et al., *Phys. Rev. C* **64**, 054606 (2001).

[64] B. Sulignano, PhD thesis, Johannes Gutenberg University, Mainz 2007.